SMIP21

SMIP21 SEMINAR ON
UTILIZATION OF STRONG-MOTION DATA

October 21, 2021

PROCEEDINGS

Sponsored by

California Strong Motion Instrumentation Program
California Geological Survey
California Department of Conservation

Co-Sponsors

California Seismic Safety Commission
California Governor's Office of Emergency Services
Office of Statewide Health Planning and Development
California Department of Transportation

California
Department of
Conservation
California Geological Survey

The California Strong Motion Instrumentation Program (CSMIP), a program within the California Geological Survey (CGS) of the California Department of Conservation, records the strong shaking of the ground and structures during earthquakes for analysis and utilization by the engineering and seismology communities, through a statewide network of strong motion instruments (www.conservation.ca.gov/CGS/smip). CSMIP is advised by the Strong Motion Instrumentation Advisory Committee (SMIAC), a committee of the California Seismic Safety Commission. Major program funding is provided by an assessment on construction costs for building permits issued by cities and counties in California, with additional funding from the California Governor's Office of Emergency Services (Cal OES), the Office of Statewide Health Planning and Development (OSHPD) and the California Department of Transportation (Caltrans)

In July 2001, the California Governor's Office of Emergency Services (Cal OES) began funding for the California Integrated Seismic Network (CISN), a newly formed consortium of institutions engaged in statewide earthquake monitoring that grew out of TriNet, funded by FEMA, and including CGS, USGS, Caltech and UC Berkeley. The goals are to record and rapidly communicate ground shaking information in California, and to analyze the data for the improvement of seismic codes and standards (www.cisn.org). CISN produces ShakeMaps of ground shaking, based on shaking recorded by stations in the network, within minutes following an earthquake. The ShakeMap identifies areas of greatest ground shaking for use by OES and other emergency response agencies in the event of a damaging earthquake.

The Center for Engineering Strong Motion Data (CESMD) is operated by the CSMIP in cooperation with the National Strong-Motion Project (NSMP), a part of the Advanced National Seismic System (ANSS) of the U.S. Geological Survey (USGS). The CESMD builds on and incorporates the CISN Engineering Data Center and will continue to serve the California region while expanding to serve other ANSS regions. The Data Center provides strong-motion data rapidly after a significant earthquake in the United States. Users also have direct access to data from previous earthquakes and detailed information about the instrumented structures and sites. The CESMD also provides access to the U.S. and international strong ground motion records through its Virtual Data Center (VDC). The Data Center is co-hosted by CGS and USGS at www.strongmotioncenter.org

DISCLAIMER

SMIP21

SMIP21 SEMINAR ON
UTILIZATION OF STRONG-MOTION DATA

October 21, 2021

PROCEEDINGS

Edited by

Daniel Swensen

Sponsored by

California Strong Motion Instrumentation Program
California Geological Survey
California Department of Conservation

Co-Sponsors

California Seismic Safety Commission
California Governor's Emergency Services
Office of Statewide Health Planning and Development
California Department of Transportation

PREFACE

The California Strong Motion Instrumentation Program (CSMIP) in the California Geological Survey of the California Department of Conservation established a Data Interpretation Project in 1989. Each year CSMIP funds several data interpretation contracts for the analysis and utilization of strong-motion data. The primary objectives of the Data Interpretation Project are to further the understanding of strong ground shaking and the response of structures, and to increase the utilization of strong-motion data in improving post-earthquake response, seismic code provisions and design practices.

As part of the Data Interpretation Project, CSMIP holds annual seminars to transfer recent research findings on strong-motion data to practicing seismic design professionals, earth scientists and post-earthquake response personnel. The purpose of the annual seminar is to provide information that will be useful immediately in seismic design practice and post-earthquake response, and in the longer term, useful in the improvement of seismic design codes and practices. Proceedings and individual papers for each of the previous annual seminars are available at http://www.conservation.ca.gov/cgs/smip/seminar in PDF format. Due to State budget constraints, CSMIP did not hold an annual seminar in 2010 or 2011. The SMIP21 Seminar is the thirtieth in this series of annual seminars.

The SMIP21 Seminar is divided into two sessions in the morning and two sessions in the afternoon. There are three presentations on the results from CSMIP-funded projects and five invited presentations. The sessions in the morning include four presentations. The first session will focus on ground motion issues. Professor Ziotopoulou of UC Davis will present on developing input motions for site response and nonlinear deformation analyses. She will be followed by a presentation from Professor Abrahamson of UC Berkeley on site response based on Vs profile information. The second session will focus on structural response topics. Professor Kunnath of UC Davis will present on ASCE-41 acceptance criteria for steel moment frame buildings. Dr. Celebi of USGS and I will then present on recent response studies of four tall buildings in California.

The two sessions in the afternoon include four presentations on a variety of topics. In the third session, Professor Olsen of San Diego State University will present on seismic hazard analysis of embankment dams. He will be followed by a presentation from Professor Mosalam of UC Berkeley on structural health monitoring. The last session will include a presentation on earthquake early warning by Dr. Given of USGS, and a presentation on the Community Seismic Network by Professor Kohler of Caltech. Individual papers and the proceedings are available for download by the SMIP21 participants at the provided link and will be available at the CSMIP website in the future.

Daniel Swensen
CSMIP Data Interpretation Project Manager

Appreciation to Members of the Strong Motion Instrumentation Advisory Committee

Main Committee

Farzad Naeim, Chair, Farzad Naeim, Inc.
Norman Abrahamson, UC Berkeley
Bruce Clark, Leighton & Associates
Martin Eskijian, California State Lands Commission (retired)
David Gutierrez, GEI Consultants
Marshall Lew, Wood
Bret Lizundia, Rutherford + Chekene
Carlos Ventura, University of British Columbia
Chris Tokas, Office of Statewide Health Planning and Development
Jia Wang-Connelly (ex-officio), Seismic Safety Commission

Ground Response Subcommittee

Marshall Lew, Chair, Wood
Zia Zafir, Kleinfelder
Martin Hudson, Turner

Buildings Subcommittee

Bret Lizundia, Chair, Rutherford + Chekene
Lucie Fougner, Degenkolb Engineers
Ifa Kashefi, City of Los Angeles (retired)
Michelle Yu, City of San Francisco
Eduardo Miranda, Stanford University
Roy Lobo, Office of Statewide Health Planning and Development
Chia-Ming Uang, UC San Diego

Lifelines Subcommittee

Martin Eskijian, Chair, California State Lands Commission (retired)
David Gutierrez, GEI Consultants
Faiz Makdisi, Gannett Fleming

Data Utilization Subcommittee

Representatives from each Subcommittee

TABLE OF CONTENTS

SMIP21 SEMINAR ON UTILIZATION OF STRONG-MOTION DATA

October 21, 2021

FINAL PROGRAM

9:00 am **WELCOMING REMARKS**
Farzad Naeim, Chair, Strong Motion Instrumentation Advisory Committee (SMIAC)
Steve Bohlen, Acting State Geologist, California Geological Survey (CGS)

9:20 am **INTRODUCTION**
Hamid Haddadi, Program Manager, California Strong Motion Instrumentation Program
Dan Swensen, Senior Civil Engineer, California Strong Motion Instrumentation Program

Session I

Moderator: *Zia Zafir*, Kleinfelder and SMIAC

9:30 am **Broadening the Utilization of CSMIP Data: Double Convolution Methodology towards Developing Input Motions for Site Response & Nonlinear Deformation Analyses**
Renmin Pretell, S. K. Sinha and *Katerina Ziotopoulou*, UC Davis
Jennie Watson-Lamprey, Slate Geotechnical Consultants
Dimitrios Zekkos, UC Berkeley

10:00 am **Move from Soil/Rock: Site Response Based on the Difference in the VS Profile for the GMPE and the Site-specific VS Profile**
Norman Abrahamson, UC Berkeley

10:30 am **Break**

Session II

Moderator: *Bret Lizundia*, Rutherford + Chekene and SMIAC

11:00 am **Utilizing Instrumented Data to Assess ASCE-41 Acceptance Criteria for Steel Moment Frame Buildings**
Laura Hernandez-Bassal and *Sashi Kunnath*, UC Davis

11:30 am **Collaborative Recorded Data Based Response Studies of Four Tall Buildings in California**
Dan Swensen, California Strong Motion Instrumentation Program
Mehmet Celebi, U.S. Geological Survey

12:00 pm **Lunch Break**

Session III

Moderator: *Martin Eskijian*, California State Lands Commission and SMIAC

1:00 pm **Next Generation Seismic Hazard Analysis of Embankment Dams: Case of the Long Valley Dam, CA**
Kim Olsen, T.-Y. Yeh and Daniel Roten, San Diego State University

1:30 pm **Artificial Intelligence-Enabled Structural Health Monitoring**
Yuqing Gao and *Khalid Mosalam*, UC Berkeley

2:00 pm **Break**

Session IV

Moderator: *Marshall Lew*, Wood and SMIAC

2:30 pm **ShakeAlert Earthquake Warning: The Challenge for Transforming Ground Motion into Protective Actions**
Douglas Given, U.S. Geological Survey

3:00 pm **The Community Seismic Network for Dense, Continuous Monitoring of Ground and Structural Strong Motion**
Monica Kohler, Caltech

3:30 pm **Adjourn**

BROADENING THE UTILIZATION OF CSMIP DATA: DOUBLE CONVOLUTION METHODOLOGY TOWARDS DEVELOPING INPUT MOTIONS FOR SITE RESPONSE AND NONLINEAR DEFORMATION ANALYSES

Renmin Pretell[(1)], Sumeet K. Sinha[(1)], Katerina Ziotopoulou[(1)], Jennie A. Watson-Lamprey[(2)], and Dimitrios Zekkos[(3)]

[(1)] Department of Civil and Environmental Engineering, University of California, Davis
[(2)] Slate Geotechnical Consultants
[(3)] Department of Civil and Environmental Engineering, University of California, Berkeley

Abstract

The double convolution methodology for the development of input motions for site response analyses and nonlinear deformation analyses is presented, and challenges associated with its development and implementation are discussed. This methodology uses deep V_S profiles and random vibration theory to modify ground motions recorded on soil sites such that they are compatible with conditions at a selected depth within a deposit. This selected depth is commonly the base of a numerical domain for a 1D or 2D response analysis, i.e. halfspace. Ongoing efforts in the development of this methodology focus on constraining the ground motions' high-frequency content, where unrealistic amplification may be estimated. Two approaches for addressing this issue are presented using examples in California.

Introduction

Ground surface seismic stations are dominant in most seismic networks around the world. Recordings from these stations are commonly used as input motions in site response analyses (SRAs) and 2- or 3-dimensional (2D or 3D hereafter) nonlinear deformation analyses (NDAs) employed for (1) the design of structures such as dams, bridges, and buildings; and (2) the study of case histories either towards validating numerical procedures or towards forensically investigating possible causes of failures (e.g., Pretell et al. 2021). For instance, Figure 1 presents a schematic of a typical scenario where input ground motions are needed for the evaluation of the seismic performance of a dam using NDAs. In this case, the target site and depth are the location of the dam and the depth of the halfspace, respectively.

Common approaches for developing input ground motions for the design of structures consist of two steps: (1) the selection of recordings based on a seismic scenario and site conditions consistent with the halfspace; and (2) the modification of the recordings to approximately match a spectral shape, a ground motion intensity measure, or meet some other criterion such that the resulting ground motions are consistent with the halfspace (e.g., Abrahamson 1992a, Hancock et al. 2006, Watson-Lamprey and Abrahamson 2006, Baker et al. 2011, Arteta and Abrahamson 2019, Mazzoni et al. 2020). The first step strongly depends on the candidate recordings available, which are often selected from recording stations (i.e., reference site in Figure 1) that have an inverse of the average slowness on the top 30 m (V_{S30}) higher than 760 m/s, i.e. rock sites

(ASCE2016). These stations are commonly referred to as “outcropping rock.” Outcropping rock stationsare not widely available in shallow crustal tectonic regions as they add up to only 3% of the ground motion recordings from the Center for Engineering Strong Motion Data (CESMD) as of June 2020.In the case of forensic studies, the ability to replicate the case history strongly depends on availableseismic stations as candidate ground motions should be representative of the specific seismic scenario, at a specific location and depth. The limited number of ground motions recorded at outcropping rock sites leads practitioners and researchers to use ground surface motions recordedat soil sites, hereafter referred to as “ground surface recordings,” with some modifications.

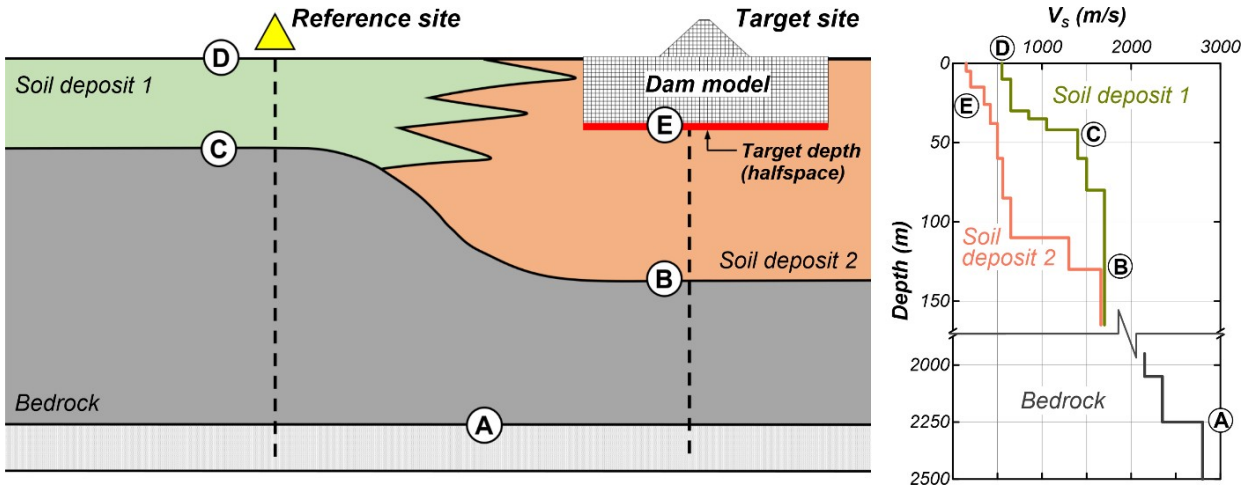

Figure 1. Schematic of a typical scenario where input ground motions for site response analyses (SRAs) or nonlinear deformation analyses (NDAs) at a target site can be developed based on a ground motion recorded at a reference site (seismic station).

Several procedures are used for the development of input ground motions in the absence of recordings from rock stations. A common approach is deconvolution analysis, which is a type of 1D SRA that allows for the computation of ground motions that would have been recorded at some depth given ground motion recordings at the ground surface at the same site. Deconvolution can occasionally lead to numerical errors and spurious ground motions (Kramer 1996). Other approaches for the modification of ground surface recordings include the procedures proposed by Cabas and Rodriguez-Marek (2017) and Ntritsos et al. (2021), which respectively use VS-□0 correction factors, and a four-step approach including deconvolution to account for differences between the target and reference (i.e., recording station) sites.

This paper describes an ongoing investigation towards the development and implementation of the double convolution methodology, initially presented by Pretell et al. (2019). Pretell et al. (2019) presented a two-stage procedure for the development of input motions for SRAs and NDAs: (1) modification of ground motion recordings from ground surface stations to be representative of conditions at some target depth; and (2) incorporation of ground motion incoherency (e.g., Abrahamson 1992b) for the analysis of elongated geosystems. In this work, attention is placed on the first stage, hereafter referred to as “double convolution methodology.” First, previously proposed approaches are described and differences and commonalities with the

double convolution methodology are highlighted. Second, sites in California considered for the ongoing investigation are presented, and 5 km-deep VS profiles are developed based on shallow measurements (e.g., suspension logging tests) and velocity models from the Unified Community Velocity Model, UCVM (Small et al. 2017). Lastly, challenges associated with the development of the double convolution methodology and potential solutions are presented within the context of examples in California.

The ultimate goal of this investigation is to broaden the utilization of data from the Centerfor Engineering Strong Motion Data (CESMD) and ground surface stations in general. Specific results are expected to provide: (1) a robust yet practical methodology for the development of at- depth input ground motions based on ground surface recordings; (2) a user-friendly web-based tool accompanied by a user guide and example applications; (3) readily available modified groundmotion recordings at depths of potential interest within California sites, obtained during the development of this investigation; (4) newly measured VS profiles that will enrich the current database and allow for future research efforts; and (5) feedback to the Strong Motion Instrumentation Program (SMIP) regarding the utility of the available data.

Approaches for developing input ground motions

Deconvolution

Deconvolution analysis (Schnabel et al. 1972, Kramer 1996) is commonly used in engineering practice and research for the development of ground motions at depth based on a ground motion recorded at the ground surface (e.g., Mejia and Dawson 2006, Chiaradonna et al. 2018). It is a practical technique; however it is also highly sensitive to the analysis input parameters such as the VS profile (Cadet et al. 2011) and may run into numerical instabilities that impact the accuracy of the resulting ground motions (e.g., Roesset et al. 1995, Di Giulio et al. 2014).

Common practices for preventing numerical issues when using deconvolution analysis include (1) scaling down the ground motion amplitudes such that only the ground motion fraction that can be explained by vertical propagation of waves is used (e.g., Silva et al. 1988); (2) post-filtering of ground motions to remove any unreasonably high-frequency content (e.g., Silva et al. 1988, Markham et al. 2015), and (3) using strain ratios and number of iterations different than the values traditionally used in equivalent linear SRAs (Bartlett et al. 2005). These approaches are either not implemented in most commercial programs, or are developed based on observations specific to a single site, and are thus of little use to the practicing engineer. In addition, oftentimes the site and depth of interest are not the seismic station and the sensor depth, but rather a neighboring location. Thus, a subsequent convolution analysis accompanied by scaling or other procedures may be required to adapt the deconvolved ground motion to the target location.

VS-□0 correction by Cabas and Rodriguez-Marek (2017)

Cabas and Rodriguez-Marek (2017) proposed a VS-□0 correction factor to modify ground surface recordings and make them consistent with conditions at some target depth, where □0 is the distance-independent component of the high-frequency decay parameter (Anderson and Hough 1984). Thisapproach captures both impedance and attenuation effects through the respective use

of the correction factors CF_{imp} and CF_{atn}. The CF_{imp} factor is the inverse of the transfer function (TF) computed using the square-root-impedance method (Joyner et al. 1981), whereas the CF_{atn} factor is based on measurements of the attenuation in the shallow crust, □. The CF_{imp} is equal or lower than 1 and accounts for the amplification from the target depth to the ground surface, while C_{atn} isequal or higher than 1 and accounts for the dissipation of energy from the target depth to the ground surface. In a study conducted by the same researchers (Cabas and Rodriguez-Marek 2017) using data from the KiK-net database, the VS-□0 correction factors demonstrated a better performance than linear elastic deconvolution analysis in the characterization of the spectral energy in the high-frequency range, except for stations with soft shallow deposits. This approach is only applicable within the linear elastic range of soils' behavior, and for sites that do not have soft materials near-surface or strong resonances. Ground motions developed using VS-□0 correction factors might present unrealistically high amplification of the high-frequency components.

Ntritsos et al. (2021) methodology

These researchers proposed a four-step methodology for the development of input ground motions for the forensic evaluation of case histories: (1) selection of a reference layer consistent with the target layer, (2) selection of seismic events, (3) deconvolution analysis, and (4) scaling of the deconvolved ground motions. The first three steps are consistent with the common practices previously described, whereas the fourth step offers two scaling approaches to account for the differences in the source-to-distance effects at the target and reference sites. This methodology offers an improved approach towards accounting for the differences between target and reference sites. However, numerical issues associated with deconvolution analysis (3rd step) can limit its implementation in practice.

Double convolution methodology for the development of input ground motions

The double convolution methodology allows for the development of ground motion recordings at a target site and depth based on recordings from a ground surface station. The proposed approach aims at developing input motions at a target site and depth, "E" in Figure 1, based on a ground motion recording from a ground surface recording at a "reference site", "D" in Figure 1. This methodology requires that a common geologically-based stratum of similar stiffnesses is present at both the target and reference sites, locations "C" and "B" in Figure 1, respectively. At locations deeper than "B" and "C", the geological conditions are assumed to be similar, such that the ground motions can be considered to result from the upward propagation of the same ground motion at location "A". Based on this assumption, the ground motion at "E" can be estimated as the product of two transfer functions (TF): TF_1 deconvolves the ground motion from location "D" to "C", and TF_2 propagates the ground motion from "B" (equivalent to "C") to"E." This relation can be expressed as presented below, where "GM" is a ground motion in the frequency domain:

$$GM_E = \frac{GM_C}{GM_D} \cdot \frac{GM_E}{GM_B} \rightarrow GM_D$$

Target Reference

Equivalently, in terms of TFs:

$$\underbrace{GM_E}_{\text{Target}} = TF_1 \cdot TF_2 \cdot \underbrace{GM_D}_{\text{Reference}}$$

Where TF1 is computed as the ratio of results from two convolution analyses, from "A" to "C" andfrom "A" to "D." TF2 allows for the subsequent convolution to a target depth, e.g. a selected halfspace, and is computed similarly to TF1. The input ground motion at location "A" can be developed as a Fourier Amplitude spectrum using seismological theory (e.g., Brune 1970, 1971, Boore 2003a), finite fault seismological simulations (e.g., Beresnev and Atkinson 1998), or another preferred method. This ground motion is then propagated upwards using random vibrationtheory (RVT). Once TF1 and TF2 are computed, the ground motion at location "E" can be estimatedusing the inverse Fast Fourier Transform (iFFT) of the product of these TFs and the reference ground motion recording. Note that TF1 is equivalent to the TF used for deconvolution analysis, and TF2 is equivalent to conducting a subsequent convolution analysis using the deconvolved timehistory as input motion. In applications that only require deconvolving a ground motion recordingat the reference site, TF2 = 1. However, in most applications the deconvolved ground motions needto be further modified (e.g., linear scaling) to account for source, path, and site effects (e.g., Chiaradonna et al. 2018). Figure 2 presents a flow chart of the double convolution methodology.

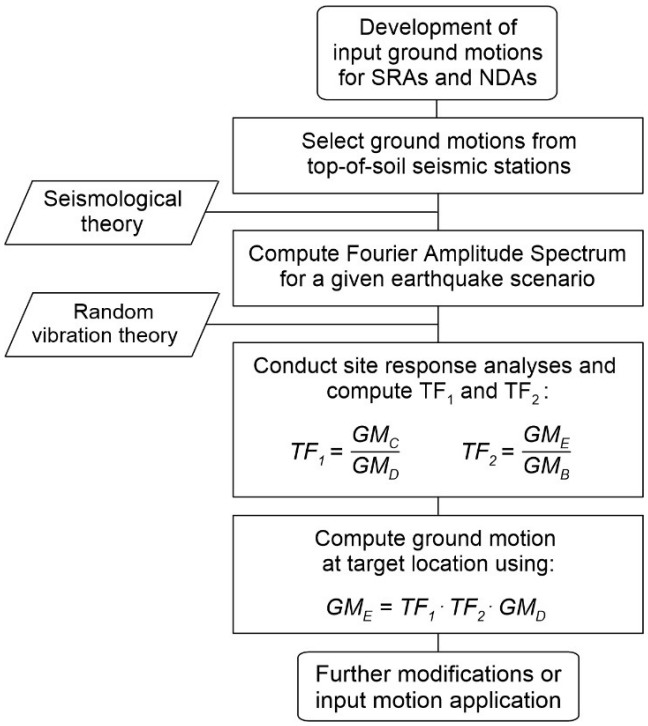

Figure 2. Proposed methodology for the development of input ground motions for site response and nonlinear deformation analyses. Adapted from Pretell et al. (2019).

The double convolution methodology is different from previously proposed approaches. This methodology provides (1) a robust and practical technique for the modification of ground surface recordings to make them compatible with conditions at some target site and depth; (2) the ability to account for moderate soil nonlinearities such as those handled by equivalent linear SRAs, i.e., maximum shear strains lower than 0.1% (Kaklamanos et al. 2013); and (3) the potential for

efficient propagation of uncertainties. The double convolution approach uses deep V_S profiles to account for site effects within high-V_S materials, which are typically considered negligible and might lead to underestimation of the seismic response (Steidl et al. 1996). The proposed methodology uses 1D linear elastic or equivalent linear SRAs along with RVT, and thus carries the same limitations as these tools, e.g., omission of ground motion lengthening effects and changes in ground motion phase due to wave propagation.

Development of double convolution for sites in California

The double convolution methodology is used to develop ground motions at selected depths based on ground surface recordings from the CESMD, located in California. Sixteen geotechnical array sites from the CESMD are selected across California, three of them are paired with a neighboring ground surface site (Figure 3, Tables 1 and 2). The downhole recordings of geotechnical array sites allow for the partial evaluation of the performance of the proposed methodology, i.e. the estimation of TF_1. Meanwhile, the paired sensors allow for a full evaluationof the proposed methodology. The selection of neighboring sites reduces the differences in source,path, and site effects between sites, thus reasonably improving the quality of the evaluation.

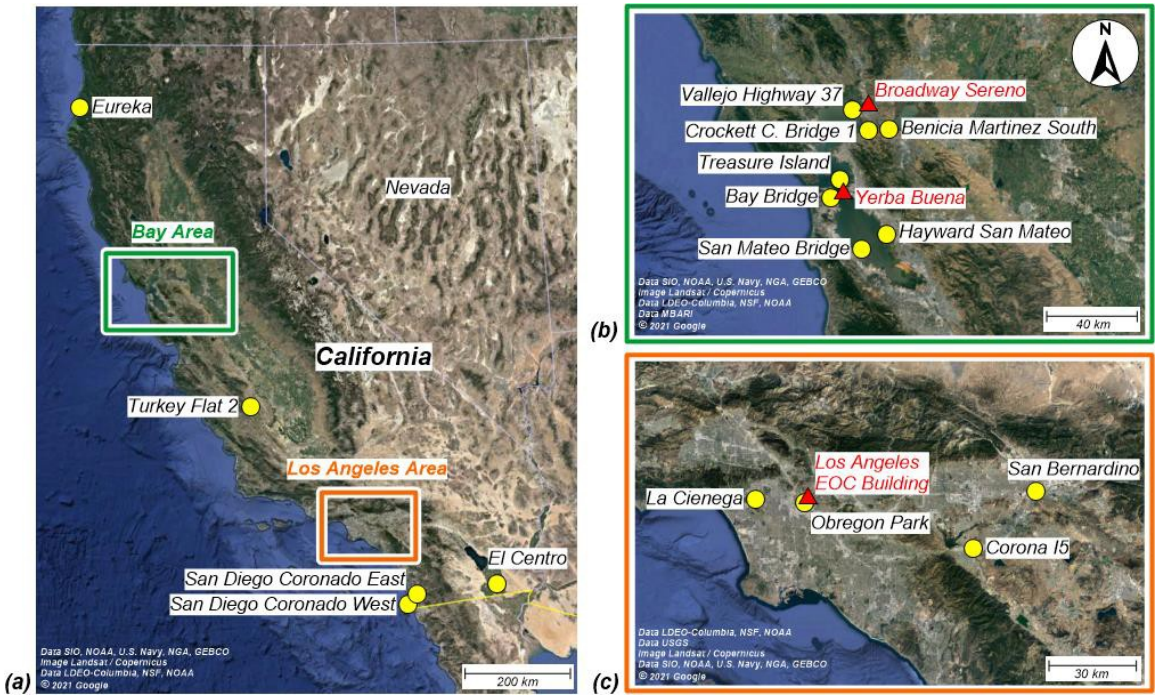

Figure 3. Seismic stations selected for the application of the double convolution methodology: (a) locations in California, (b) locations in the Bay Area, and (c) locations in Los Angeles Area.

Ground motion recordings

The ground motion recordings from CESMD, collected and processed by Afshari et al. (2019), are used in this study. To examine the effect of soil nonlinearity and based on a I_γ-based criterion, ground motions are separated into weak and strong ground motions and with linear

elastic and equivalent linear SRAs used, respectively. Ground motions that yield shear strain index (I_γ) values lower than 0.01% are considered weak and appropriate for linear elastic SRAs (Kaklamanos et al. 2013), where I_γ was proposed by Idriss (2011) and is defined as:

$$I_\gamma = \frac{PGV}{V_{S30}} \times 100\%$$

Where I□ is in percentage, and PGV is the peak ground velocity at surface in the same units as VS30.Ground motions yielding I□ values between 0.01 and 0.1% are considered strong and equivalent linear SRAs more appropriate for their propagation.

Table 1. Geotechnical array sites to be considered in this investigation.

MEDID	Station	Sensor depth[1] (m)	V_S shallow(field test)	V_S deep (UCVM[2])	V_S shallow-based V_{S30} (m/s)
68323	Benicia Martinez	35	Suspension logging	cs173h	588
68206	Crockett Carquinez Bridge 1	45.7	Suspension logging	cs173h	350
1794	El Centro	195	Suspension logging	cvms5	200
58798	Hayward San Mateo	91	Suspension logging	cencal	184
24703	La Cienega	100	Suspension logging	cvmsi	254
24400	Obregon Park	69.5	Suspension logging	cvmsi	450
23792	San Bernardino	35	Suspension logging	cvmsi	268
58961	San Francisco Bay Bridge	40	Suspension logging	cencal	383
58642	Treasure Island	122	Suspension logging	In progress	159
36520	Turkey Flat 2	23	SASW	cs173h	Not applicable
68310	Vallejo Highway 37	44.7	Suspension logging	cs173h	527

[1] Sensor depth considered for this study.
[2] Acronyms/abbreviations presented in Table 3.

Table 2. Ground surface stations for the application of double convolution methodology.

CSMEDID	Station	V_S shallow (field test)	V_S deep (UCVM[4])	V_S shallow-based V_{S30} (m/s)	Neighboring downhole station	
					Site name	Distance (km)
58163	Yerba Buena	Downhole[2]	cencal	Not available[3]	Treasure Island	2.25
24723	LA EOC Building[1]	Downhole[2]	In progress	Not available[3]	Obregon Park	1.50
68294	Broadway and Sereno	Not available	In progress	Not available	Vallejo Hwy. 37	2.29

[1] Los Angeles County of Emergency Office Center Building.
[2] V_S profiles measured 220 and 580 m from the Yerba Buena and LA EOC Building stations, respectively.
[3] Measured V_S profile shallower than 30 m.
[4] Acronyms/abbreviations presented in Table 3.

Site characterization

The site characterization of the selected CESMD sites is conducted for linear elastic and equivalent linear applications. The characterization consists of the following: (1) development of deep V_S profiles based on shallow measurements and velocity models, (2) small-strain damping profiles, (3) soil unit weight profiles, and (4) equivalent linear properties. The following section describes the criteria and assumptions considered for the selection of these input parameters.

Shear wave velocity (V_S) profiles

Shear wave velocity (V_S) profiles for the selected sites are developed as the combination of relatively shallow site-specific measurements and deep profiles based on V_S models from the UCVM (Small et al. 2017) as presented in Figure 4. Shallow V_S profiles are collected from various studies: Gibbs et al. (1992, 2000), Nigbor and Swift (2001), Boore (2003b), Gibbs et al. (2003), Thompson et al. (2010), and Petralogix (2017), with most of these integrated into the database by Afshari et al. (2019). In addition, 5 km-deep V_S profiles are sampled from velocity models included in the UCVM. The sample spacing ranges from 1 to 10 m, with finer sampling at the top of the profile. The shallow and deep V_S profiles are combined to obtain a detailed V_S profile near the ground surface while reaching a significant depth to estimate the site response.

Table 3. Velocity models from the SCEC UCVM evaluated for the selection of deep V_S profiles.

Model name	Abbreviation	Comment[1]	Reference
Modified Hadley-Kanamori1D	1D	Southern California region, V_P-base estimation of V_S.	Hauksson (2010)
Northridge region 1D	bbp1D	Northridge region, based on profiles from the Southern California Earthquake Center sites.	Graves and Pitarka (2010)
Central California velocity model, CCA06	cca	Based on full 3D tomographic inversions.	En-Jui Lee
USGS Bay Area velocitymodel v0.8.3	cencal	3D velocity model defined on regular mesh.	Brocher et al. (2006)
Southern California velocity model, CVM-H v15.1	cvmh	Southern California 3D velocity model defined on regular mesh. Developed by SCEC and the Harvard Structural Geology Group.	Süss and Shaw (2003), Shaw et al. (2015)
Southern California velocity model CVM-S4	cvms	Southern California 3D velocity model defined as rule-based system. Developed by the SCEC, Caltech, and USGS groups.	Kohler et al. (2003)
Southern California velocity model, CVM-S4.26	cvms5	Based on CVM-S4 as starting model but improved using 3D tomography and 26 iterative updates.	Lee et al.(2014)
Southern California velocity model, CVM-S4.26.M01	cvmsi	Based on the CVM-S4.26 but preserving some ofthe geotechnical information in the original CVM- S4 that was lost during tomography improvements.	Lee et al.(2014)

CyberShake v17.3 Central California Velocity	cs173	Tiled from CCA06, CenCal, and CVM-S4.26.M01.	SCEC (2018a)
CyberShake v17.3 Central California Velocity	cs173h	Similar to the above but includes the San Joaquinand Santa Maria Basins and data from Harvard's group.	SCEC (2018b)

[1] Based on Small et al. 2017, Shi and Asimaki 2018, SCECpedia, and github.com/SCECcode/UCVM.

The aforementioned sources of VS often provide multiple alternative profiles. Shallow VS profiles generally consist of measurements from P-S suspension logging tests, and non-invasive methods such as the spectral analysis of surface waves (SASW). From these, P S suspension logging is preferred as it is an invasive method and thus provides high resolution regardless of depth (Passeri 2019). The deep VS profiles are obtained using all of the models presented in Table3 when available for the location of the sites. Most models include a geotechnical layer, GTL (Elyet al. 2010) that consists of a soft layer in the top 350 m generated based on VS30, and the CVM- H15.1.0 VS at 350 m. The GTL helps with accounting for the soft sediments near the ground surface, but it assumes a smooth increase in VS and thus misses the presence of sharp impedance contrasts that affect site response (Shi and Assimaki 2018), and occasional inconsistencies in the geometry of the Los Angeles basin (Taborda et al. 2016). Therefore, shallow VS profiles are entirely used to replace the top portion of the UCVM profiles at all the selected locations.

Deep VS profiles are selected based on how well the shallower portion compares to the shallow VS profiles from site-specific measurements. No shifting of depth or VS scaling is appliedto the deep VS profiles in the selection process. Taborda et al. (2016) conducted a validation studyto evaluate the CVM-S4, CVM-S4.26, CVM-H, and CVM-H with GTL models in their ability tolead to accurate ground motion predictions for 30 events recorded in Los Angeles. The authors concluded that the CVM-S4, CVM-S4.26.M01 models (Table 3) consistently yielded the most accurate results. Based on this finding, deep VS profiles from the CVM-S4 and CVM-S4.26.M01 models are preferred when multiple profiles are equally adequate. The selection and constructionof VS profiles represent a source of epistemic uncertainty that will be further studied, and newly measured VS profiles incorporated in future stages of this investigation.

Other material properties

Other material properties consist of the small-strain damping, equivalent linear properties for soils, and unit weight. These properties are estimated based on correlations and typical values. Small-strain damping is computed based on quality factors (Q) estimated as a function of VS basedon a relation proposed by Campbell (2009) for sites in California:

$$D_{min} = \frac{1}{2 \cdot Q}; \quad \text{and} \quad Q = 7.17 + 0.0276 \cdot V_S$$

Where V_S is in m/s and D_{min} in decimal.

Equivalent linear properties are assigned to soil materials ($V_S \leq 760$ m/s), whereas linear elastic behavior is assumed for rock-like materials ($V_S > 760$ m/s). The Darendeli (2001) model is used to model the nonlinear behavior of all soils. This model is selected to account for the dependency of soil's behavior on the effective vertical stress. Different plasticity indexes (PIs) are assigned to soil materials based on the overall characteristic of the soil unit as described in the available boring logs or geological information included in database by Afshari et al. (2019) and other available studies listed in previous section. Granular soils (i.e., sands and gravels) are assigned a PI = 0, and fine soils are assigned a PI = 15 as a reasonable representative estimate. Finally, a unit weight of 18 kN/m^3 is assumed for all soils, whereas a unit weight of 22 kN/m^3 is assumed for all rock-like materials. The ability of the double convolution methodology for efficiently propagating uncertainties allows for the future incorporation of alternative selected parameters.

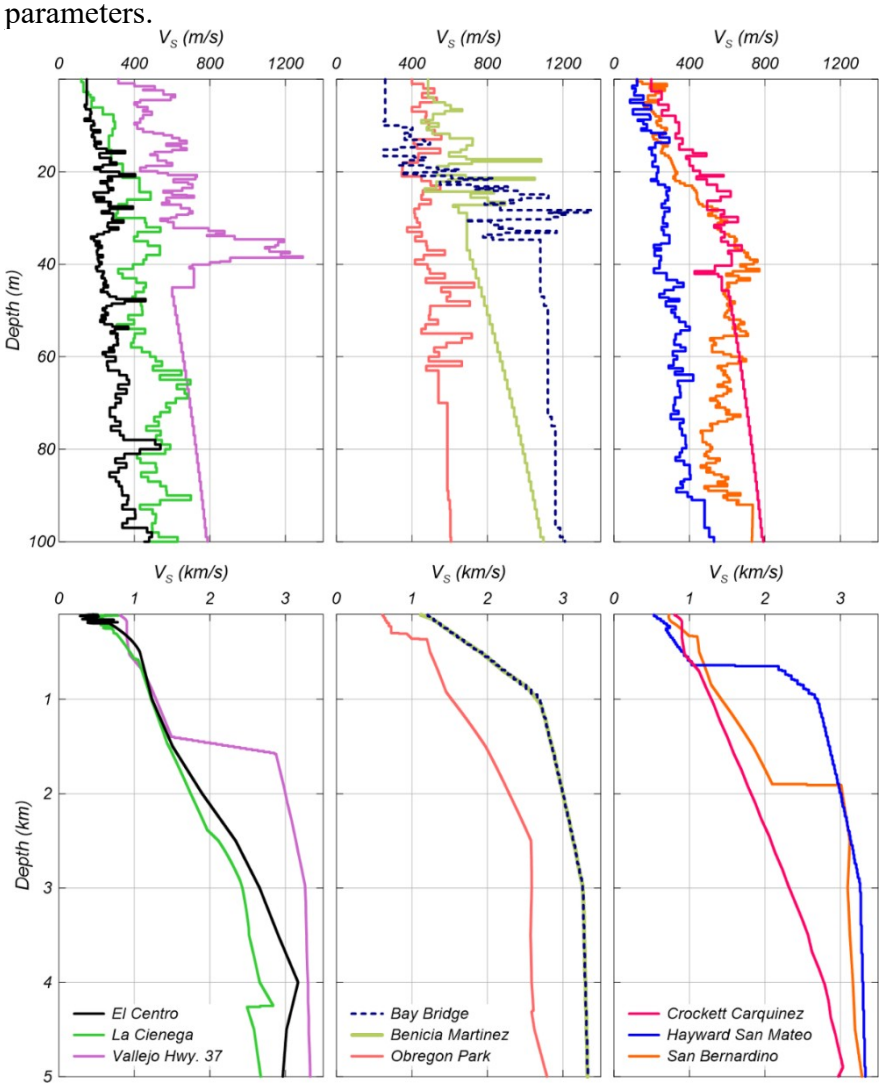

Figure 4. Combined shallow (V_S measurement-based) and deep (UCVM-based) V_S profiles for various seismic stations selected for the modification of ground motions using the double convolution methodology. *Note: Grouping of profiles for visual purposes only.*

Challenges associated with the development of the double convolution methodology

Key aspects challenging the development and validation of the double convolution methodology towards being robust and reasonably accurate, mainly consist of three issues: (1) an unrealistic amplification of the ground motion high-frequency range observed in computed ground motions; (2) inaccuracies inherent in 1D SRAs and uncertainty in the estimated response due to using different computer programs (Meite et al. 2020); and (3) the aleatory variability and epistemic uncertainty, mainly associated with VS. Herein, the focus is placed on the first issue, andalternative procedures for handling it are presented. The second and third issues have been previously studied in the context of convolution SRAs by various researchers, e.g., Toro (1995), Bonilla et al. (2002), Kaklamanos et al. (2013), Zalachoris and Rathje (2015), Griffiths et al. (2016), Kaklamanos and Bradly (2018), Meite et al. (2020), and Stewart and Afshari (2020), among others.

Unrealistic amplification of ground motions' high-frequency content

The double convolution approach relies on two TFs: TF_1 is used to modify the ground surface ground motion such that it is compatible with conditions at depth, and TF_2 propagates thatground motion upwards to the base of the numerical domain (Figure 1) or a target depth. Often, anunrealistically high amplification is observed in the TF_1's high-frequency range. This problem is also one of the common sources of errors in deconvolution analyses and the V_S-κ_0 correction factorapproach by Cabas and Rodriguez-Marek (2017). This section describes two potential solutions within the context of linear elastic SRAs and two examples in California.

Events recorded at The El Centro and Obregon Park geotechnical array sites are used in this section. In this exercise, the reference and target sites are the same, and thus $TF_2 = 1$. One-dimensional SRAs are conducted using pySRA (Kottke 2019) and the acceleration response spectra are computed using pyRotD (Kottke 2018). A single acausal-filtered ground motion recording from the database by Afshari et al. (2019) is used per site. Recordings from the deepest sensors are used such that the widest possible frequency band is used. In this evaluation, downhole recordings (i.e., within ground motions) are used and thus appropriate wavefield assumptions are made in the analyses to get results that are comparable with the empirical data.

Results from the double convolution approach are presented in Figures 5 and 6 up to a maximum usable frequency of approximately 50 Hz, common to all the recordings used. Figures 5a and 6a present the empirical TF_1, computed as the ratio of the ground motion recordedat depth and the ground surface recording and smoothed using the technique proposed by Konno and Ohmachi (1998). The theoretical equivalent TFs are also presented. The uncorrected TF is obtained by following the procedure presented in Figure 2, while the two alternative TFs are obtained from using two approaches for constraining unrealistic high amplifications:
(1) establishing a TF cap ($TF_{1,max}$) and (2) constraining the contribution of TF within a frequency range up to a maximum value, f_{max}, for the computation of ground motions at depth. Figures 5c to 5f, and 6c to 6f present the resulting Fourier amplitude spectra (FAS) and acceleration response spectra resulting from the use of all the previously described TFs. Cutoff values for these two approaches, $TF_{1,max} = 0.6$, 0.8, and 1.0 (Figures 5a and 6a), and $f_{max} = 10$, 15, and 20 Hz (Figures

5b and 6b), are selected guided by empirical observations, and a greater body of results not presented herein for brevity. In the case of El Centro, the empirical TF varies consistently under the value of 1, whereas the uncorrected TF_1 progressively increases from 0.8 Hz to values higher than 10 at 25 Hz (Figures 5a and 5b). On the other hand, a different behavior is observed for Obregon Park, in which the empirical TF increases from 1 at 15 Hz to values up to 10 at 40 Hz, whereas the uncorrected TF_1 remains under values of 2 (Figures 6a and 6b).

The performance of the investigated approaches, judged based on the similarity to the empirical TFs, FAS, and response spectra, vary significantly for the El Centro site, whereas they are very similar in all the cases for Obregon Park. The wide range of variability of results for El Centro are mainly caused by the TF_1 trend to increase in the high-frequency range, contrary to what the empirical TF_1 shows. Also, TF_1 estimated using Approach 1 constrains more the TF's higher values (Figure 5a) and thus has a better estimate of the FAS and response spectra is achieved (Figures 5c and 5e), compared to Approach 2. A low $TF_{1,max} = 0.6$ leads to a TF more similar to the empirical from 8 to 30 Hz (Figure 5a). Similar trends are observed in terms of FAS and spectral accelerations (Figures 5c and 5e). Results for the event at Obregon Park indicate a more similar performance between both approaches and amongst the different $TF_{1,max}$ and f_{max} values (Figures 6c to 6f). In this case, a $TF_{1,max} = 1$ leads to the most accurate FAS and spectral accelerations at low and high frequencies (Figures 6c and 6d), although with some underprediction, and overpredictions between 6 and 8 Hz. A $f_{max} = 10$ Hz yields better predictions. The difference between the responses of these sites challenges the robustness of the double convolution approach, given that a single value for $TF_{1,max}$ and f_{max} might not be appropriate in all cases. Future advances of the double convolution methodology will focus on the development of a robust approach, based on either the first approach or a combination of both approaches, for constraining unrealistically high amplifications while reasonably preventing or aggravating the degree of underpredictions. Recommendations will be made for forward predictions, including those conducted at non-downhole sites, which are of interest for most applications.

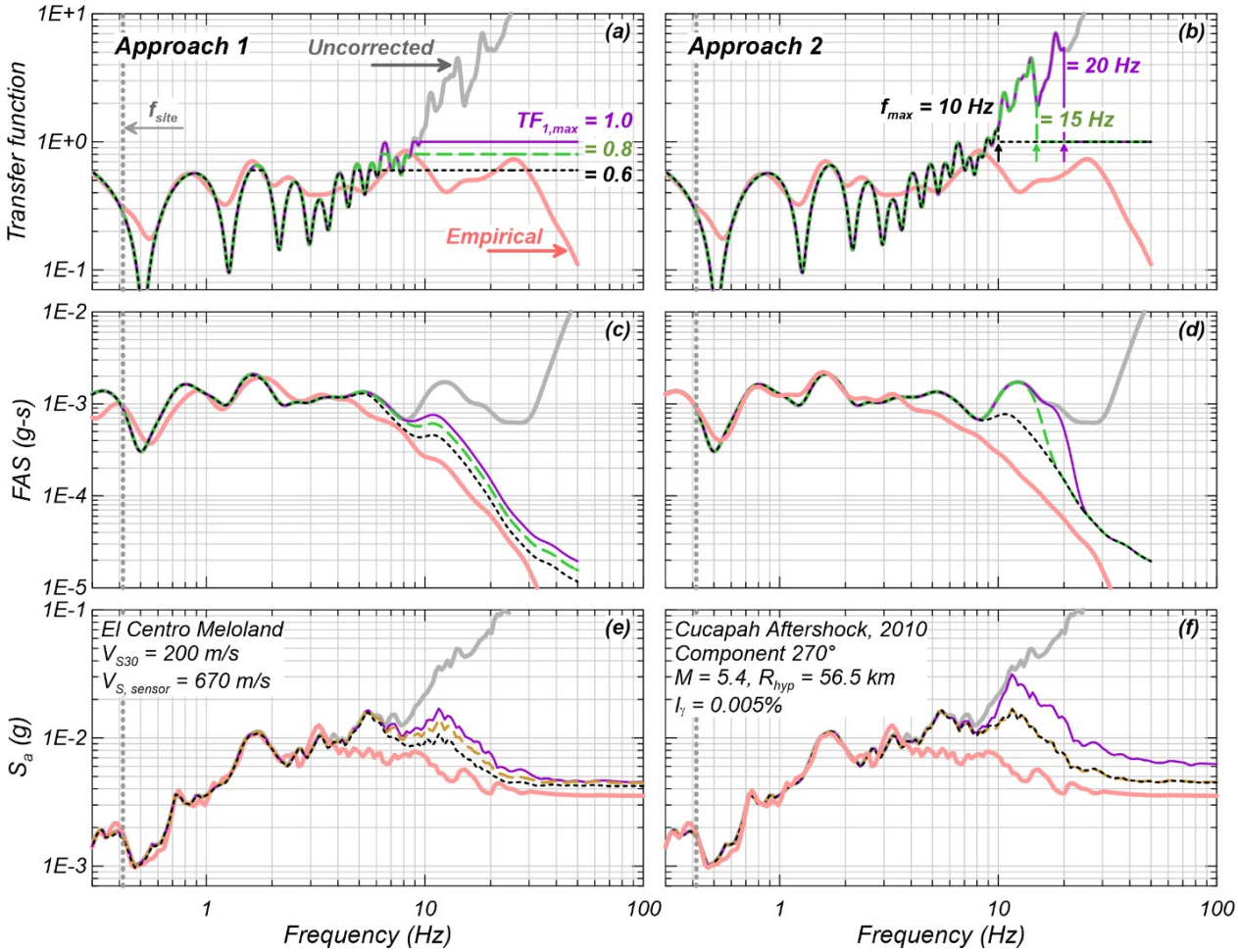

Figure 5. Two different approaches for constraining the high-frequency content in transfer function 1 (TF_1) and the effect on Fourier amplitudes and spectral accelerations (S_a). Figures (a), (c), and (e): Approach 1, TF cap ($TF_{1,max}$) across all frequencies. Figures (b), (d), and (f): Approach 2, TF considered up to a maximum frequency (f_{max}). El Centro site; downhole sensor depth = 195 m. *Note: Site's fundamental frequency, f_{site}, computed as the average V_S divided by 4 times the depth to the sensor.*

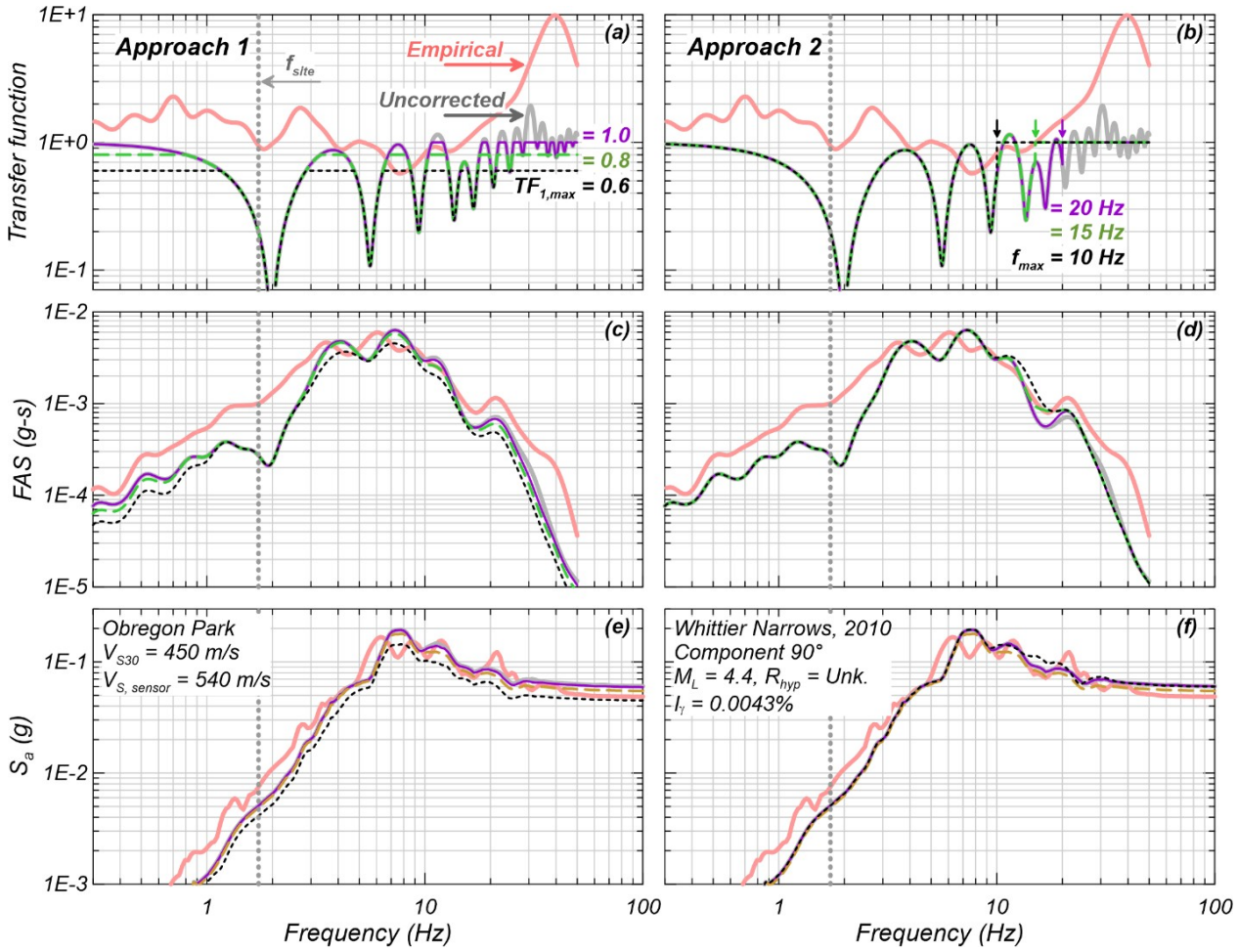

Figure 6. Two different approaches for constraining the high-frequency content in transfer function 1 (TF_1) and the effect on Fourier amplitudes and spectral accelerations (S_a). Figures (a), (c), and (e): Approach 1, TF cap ($TF_{1,max}$) across all frequencies. Figures (b), (d), and (f): Approach 2, TF considered up to a maximum frequency (f_{max}). Obregon Park site; downhole sensor depth = 69.5 m. *Note: Site's fundamental frequency, f_{site}, computed as the average V_S divided by 4 times the depth to the sensor.*

Web-based application tool

A web application tool is being developed to make the double convolution methodology accessible and usable by the broader community of practicing engineers and researchers. This tool will facilitate the generation of input motions for SRAs, NDAs, and similar applications. The web tool provides a user-friendly and intuitive graphical user interface (GUI) for taking the input parameters of the model: reference and target site profile characteristics, target depths for the development of input ground motions, and the recorded earthquake motion at the ground surface. These input data are then synthesized to generate time histories of accelerations that can be used as input ground motions for SRAs, NDAs, and other similar applications. Figure 7 illustrates the interface of the web application tool with the tabs "Soil profile," "Ground motion," "Analysis," for receiving input parameters, and the "Results" tab for showing the synthesized input ground

motions after performing the double convolution analysis. In addition, the ability to download a summary of the input parameters locally and the results will be implemented.

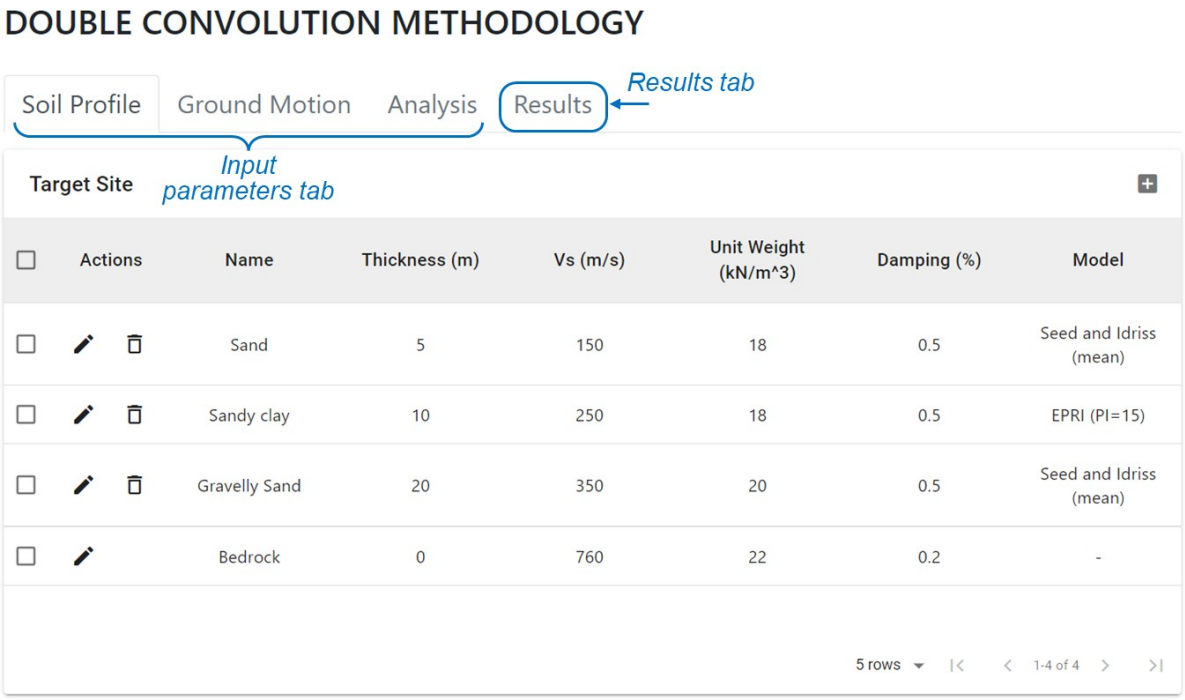

Figure 7. Web application interface for the target site's input data.

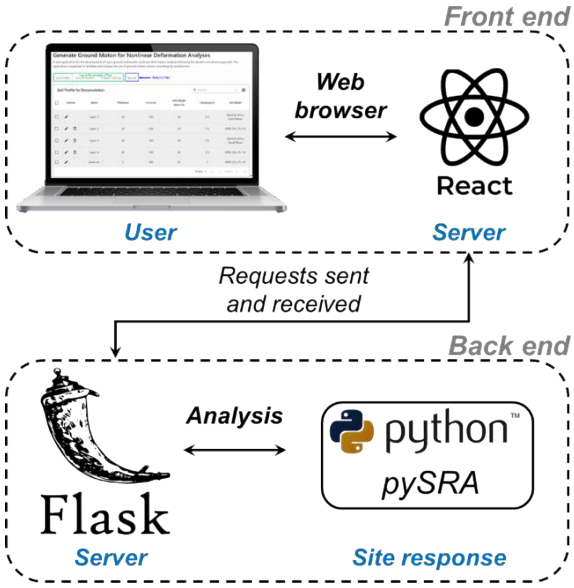

Figure 8. Web application tool architecture and request response-cycle.

The web tool is developed using React (Facebook Inc. 2021), Flask (Pallets Projects 2021), and pySRA (Kottke 2019). Figure 8 shows the web application architecture and request-response cycle. React is used to build the front end, i.e., the application's user interface (UI). Flask is used to build the back-end server to receive, send, and process the requests made by the user. Finally, any analysis involved in the double convolution methodology is performed in the back end using python and the pySRA implementation (Kottke 2019).

The fully developed web tool will be ultimately made available online and accessible to the public. In addition, a user manual with analysis guidelines and example applications will be provided to assist the users in using the tool. Its capabilities, and intuitive and user-friendly GUI are expected to be of valuable use to the geotechnical engineering practice and academia in providing a practical yet robust approach for developing ground motions.

Final remarks

This paper presented the double convolution methodology for the development of input ground motions primarily for the performance of site response analyses (SRAs) and nonlinear deformation analyses (NDAs) towards the design of structures or the forensic investigation of case histories. The double convolution methodology utilizes ground surface recordings, which dominate most seismic networks in the world. Advantages of the double convolution methodology as compared to commonly used and previously proposed approaches are: (1) its robustness in computing ground motions at a target depth based on ground surface recordings, (2) its implementation in a user-friendly interface to eventually facilitate the use of the proposed methodology in engineering practice and research, (3) the ability to account for moderate soil nonlinearities, and (4) the potential for efficient propagation of uncertainties.

Challenges encountered in the development of the double convolution methodology can be separated into three parts: (1) the unrealistic amplification of the ground motions' high-frequency content often obtained in computed ground motions, (2) the inaccuracies inherent to 1D SRAs and the uncertainty associated with site response computer programs; and (3) the aleatory variability and epistemic uncertainty associated with V_S and other parameters. The first part challenges the robustness of the approach, whereas the second and third parts challenge the precision of the results and the validation of the methodology. Empirical observations from California sites and an investigation of two approaches for handling the unrealistic amplifications of the ground motions' high-frequency content indicate that selecting a transfer function cap, $TF_{1,max}$, can be an effective measure. Further statistical evaluation of the empirical data is needed to determine an appropriate $TF_{1,max}$ for the high-frequency range. The proposed methodology is limited to cases of moderate to low nonlinearity (i.e., shear strains lower than 0.1%), it does not account for changes in phase or duration due to wave propagation, and the resulting ground motions might need further adjustments depending on site-to-source distance of the target and reference sites, or any other case-specific needs.

The double convolution methodology addresses a problem of practical importance. Expected outcomes of this investigation include: (1) a robust yet practical methodology for the development of input ground motions; (2) a user-friendly web-based tool accompanied by a user guide and example applications; (3) readily available modified ground motion recordings at depths

of potential interest within California sites, obtained during the development of this investigation; (4) measured V_S profiles that will enrich the current seismic station database and allow for future research efforts; and (5) the double convolution methodology will ultimately lead to the overall broadening of the utilization of data from the Center for Engineering Strong Motion Data (CESMD) and ground surface stations in general.

Acknowledgements

Discussions with Prof. Norman A. Abrahamson were critical in the development of the proposed approach. Dr. Christine Goulet provided clarifications on the SCEC velocity models. Drs. Mei-Hui Su and Philip Maechling provided helpful assistance in the use of the UCVM software. The authors are grateful for all of the above assistance and feedback.

References

Abrahamson, N.A. (1992a). "Non-stationary spectral matching." *Seism. Res. Lett.* 63:1, 30.

Abrahamson, N.A. (1992b). "Generation of spatially incoherent strong motion time histories." *10th World Conference on Earthquake Engineering*, II:845–850.

Afshari, K., Stewart, J.P., and Steidl, J.H. (2019). "California ground motion vertical array database." *Earthquake Spectra*, 35(4): 2003-2015.

American Society of Civil Engineers, ASCE (2016) Minimum design loads for buildings and other structures. ASCE/SEI 7 16, Reston, VA.

Anderson, J.G., and Hough, S.E. (1984). "A model for the shape of the Fourier amplitude spectrum of acceleration at high frequencies." *Bull. Seis. Society of America*, 74, 1969–1993.

Arteta, C.A., and Abrahamson N.A. (2019). "Conditional Scenario Spectra (CSS) for hazard-consistent analysis of engineering systems." *Earthquake Spectra*, 35(2): 737–757.

Baker, J.W., Lin, T., Shahi, S.K., and Jayaram, N. (2011). New Ground Motion Selection Procedures and Selected Motions for the PEER Transportation Research Program. PEER 2011/03.

Bartlett, S.F., Ostadan, F., and Abghari, C.F. (2005). "Development of design spectra for deep and soft soil sites."

Beresnev, I.A., and Atkinson, G.M. (1998). "FINSIM: A FORTRAN program for simulating stochastic acceleration time histories from finite faults." *Seismological Research Letters*, 69, 27–32.

Bonilla, L.F., Steidl, J.H., Gariel, J.C., and Archuleta, R.J. (2002). "Borehole response studies at the Garner Valley downhole array, Southern California." *Bulleting of the SeismologicalSociety of America* 92 (8): 3165–3179.

Boore, D.M. (2003a). SMSIM - Fortran Programs for Simulating Ground Motions from Earthquakes: Version 2.0 - A Revision of OFR 96-80-A. A modified ver. of OFR 00-509, USGS.

Boore, D.M. (2003b). A Compendium of P- And S-Wave Velocities from Surface-To- Borehole Logging: Summary and reanalysis of previously published data and analysis of unpublished data. USGS O.F. Report 03-191.

Brocher, T.M., Aagaard, B.T., Simpson, R.W., and Jachens, R.C. (2006). "The USGS 3Dseismic velocity model for northern California." Presented at the 2006 Fall Meeting, AGU, San Francisco, California, 11–15 December, Abstract S51B–1266.

Brune, J.N. (1970). "Tectonic stress and the spectra of seismic shear waves from earthquake." *Journal of Geophysics Research*, 75(26):4997–5009.

Brune, J.N. (1971). Correction. Journal of Geophysics Research, 76:5002.

Cabas, A., and Rodriguez-Marek, A. (2017). "V_S-κ_0 correction factors for input ground motions used in seismic site response analyses." *Earthquake Spectra*, 33(3): 917-941.

Cadet, H, Bard, P.-Y., and Rodriguez-Marek, A. (2011). "Site effect assessment using KiK-net data: Part 1. A simple correction procedure for surface/downhole spectral ratios." *Bulletin of Earthquake Engineering*, 10: 421-448.

Campbell, K.W. (2009). "Estimates of shear-wave Q and κ0 for unconsolidated and semi consolidated sediments in Eastern North America." *Bull. Seismol. Soc. Am.* 99(4): 2365–2392.

Chiaradonna, A., Tropeano, G., d'Onofrio, A., and Silvestri, F. (2018). "Interpreting the deformation phenomena of a levee damaged during the 2012 Emilia Earthquake." *Soil Dynamics and Earthquake Engineering*,124: 389-398.

Darendeli, M.B. (2001). "Development of a new family of normalized modulus reductionand material damping curves." Ph.D. dissertation, Dept. of Civil, Architectural, and Environmental Engineering, Univ. of Texas at Austin.

Di Giulio, G., Gaudiosi, I., Cara, F., Milana, G., and Tallini, M. (2014). "Shear-wave velocity profile and seismic input derived from ambient vibration array measurements: the case study of downtown L'Aquila." *Geophysical Journal International,* 198: 848-866.

Ely, G.P., Jordan, T.H., Small, P., and Maechling, P.J. (2010). "A V_{S30}-derived near surfaceseismic velocity model." AGU Fall Meet., San Francisco, California, 13–17 December, Abstract.

Facebook Inc. (2021). React - a JavaScript library for building user interfaces. v17.0.2.

Gibbs et al., BSSA (submitted), within: Boore, D.M. (2003). A compendium of P- And S-wave velocities from surface-to-borehole logging: Summary and Reanalysis of Previously Published Data and Analysis of Unpublished Data. USGS O.F. Report 03-191.

Gibbs, J.F., Fumal, T.E., Boore, D.M., and Joyner, W.B. (1992). Seismic velocities and geologic logs from borehole measurements at seven strong-motion stations that recorded the LomaPrieta

earthquake. USGS O.F. Report 92-287.

Gibbs, J.F., Tinsley, J.C., Boore, D.M., and Joyner, W.B. (2000). Borehole velocity measurements and geological conditions at thirteen sites in the Los Angeles, California region. USGS O.F. Report 00-470.

Graves, R.W., and Pitarka, A. (2010). "Broadband ground-motion simulation using a hybrid approach." *Bull. Seismological Society America*, 100, 5A, 2095-2123.

Griffiths, S.C., Cox, B.R., Rathje, E.M., and Teague, D.P. (2016). "Surface wave dispersion approach for evaluating statistical models that account for shear wave velocity uncertainty." *Journal of Geotechnical and Geoenvironmental Engineering*, 142(11): 04016061.

Hancock, J., Watson-Lamprey, J., Abrahamson, N.A., Bommer, J., Markatis, A., McCoyh,E., and Mendis, R. (2006). "An improved method of matching response spectra of recorded earthquake ground motion using wavelets." *Journal of Earthquake Engineering*, 10(S1): 67–89.

Hauksson, E. (2010). "Crustal structure and seismic distribution adjacent to the Pacific andNorth America plate boundary in southern California." *J. Geophys. Res.* 105, B6, 13,875-13,903.

Idriss I.M. (2011) "Use of V_{S30} to represent local site conditions." *4th IASPEI/IAEE international symposium. Effects of source geology on seismic motion.*

Joyner, W.B., Warrick, R.E., and Fumal, T.E., (1981). "The effect of quaternary alluviumon strong ground motion in the Coyote Lake, California, Earthquake of 1979." *Bulletin of the Seismological Society of America*, 71, 1333–1349.

Kaklamanos J., and Bradley, B.A. (2018). "Challenges in predicting seismic site responsewith 1D analyses: conclusions from 114 KiK-net vertical seismometer arrays." *Bulletin of the Seismological Society of America*, 108(5A): 2816–38.

Kaklamanos, J., Bradley, B.A., Thompson, E.M., and Baise, L.G. (2013) "Critical parameters affecting bias and variability in site-response analyses using KiK-net downhole array data." *Bulleting of the Seismological Society of America*, 103: 1733-1749.

Kohler, M.D., Magistrale, H., and Clayton, R.W. (2003). "Mantle heterogeneities and theSCEC reference three-dimensional seismic velocity model version 3." *BSSA*, 93, 757-774.

Konno, K., and Ohmachi, T. (1998) "Ground-motion characteristics estimated from spectral ratio between horizontal and vertical components of microtremor." *Bulletin of theSeismological Society of America*, 88: 228 241.

Kottke, A.R. (2018). pyRotD, module for computing rotated response spectrum. v0.5.4.Kottke, A.R. (2019). pySRA, module for conducting site response analysis. v0.4.5.

Kramer, S.L. (1996). Geotechnical Earthquake Engineering. Upper Saddle River: Prentice Hall.

Lee, E.J., Chen, P. Jordan, T.H., Maechling, P.J., Denolle, M., and Beroza, G.C. (2014). "Full-3-D tomography for crustal structure in Southern California based on the scattering-integral and the adjoint wavefield methods." *J. Geophysics Res.* 119, 6421–6451.

Markham, C.S., Bray, J.D., and Macedo, J. (2015). "Deconvolution of surface motions from the Canterbury earthquake sequence for use in nonlinear effective stress site response analyses." *6th Int. Conf. on Earthquake Geotechnical Engineering*, Christchurch, New Zealand.

Mazzoni, S., Gregor, N., Al Atik, L., Bozorgnia, Y., Welch, D.P., and Deierlein, G.G. (2020). Probabilistic seismic hazard analysis and selecting and scaling of ground-motion records.PEER 2020/14.

Meite, R., Wotherspoon, L., Kaklamanos, J., McGann, C.R., and Hayden, C. (2020). "Sensitivity of 1-D ground motion predictions to analysis codes and material models using KiK- net vertical arrays." *Journal of Soil Dynamics and Earthquake Engineering*, 133(2020): 106113.

Mejia, L.H., and Dawson, E.W. (2006). "Earthquake deconvolution for FLAC." *4th International FLAC Symposium*, Madrid, Spain.

Nigbor, R.L., and Swift, J.N. (2001). Resolution of Site Response Issues in the Northridge Earthquake (ROSRINE), Data Collection, Processing and Dissemination from Phases 1, 2 & 4 Field and Laboratory Investigations. USC Report CE472. 15 June 2001: 250 pp.

Ntritsos, N., Cubrinovski, M., and Bradley, B.A. (2021). "Challenges in the definition of input motions for forensic ground-response analysis in the near-source region." *Eq. Spectra*.

Pallets Projects (2021). Flask – web development, one drop at a time. v2.0.1.

Passeri, F. (2019). Development of an advanced geostatistical model for shear wave velocity profiles to manage uncertainties and variabilities in ground response analyses. PhD dissertation, Politecnico di Torino.

Petralogix (2017). V_{S30} Site Characterization Report, Los Angeles, Orange, Ventura, San Bernardino, and Riverside Counties. Report 2017-00006.

Pretell, R., Ziotopoulou, K., and Abrahamson, N. (2019). "Methodology for the development of input motions for nonlinear deformation analyses." *7th International Conference on Earthquake Geotechnical Engineering*, Rome, Italy.

Pretell, R., Ziotopoulou, K., and Davis, C.A. (2021). "Liquefaction and cyclic softening atBalboa Blvd. during the Northridge 1994 Earthquake." *Journal of Geotechnical and Geoenvironmental Engineering*, 147(2): 05020014.

Roesset, J.M., Huerta, C.I., Stokoe II, K.H. (1995). "Effect of magnitude and type of damping on soil amplification." *3rd International Conference on Recent Advances in GeotechnicalEarthquake Engineering and Soil Dynamics*, Paper No. 10.25. St. Louis, MO.

SCEC. Scecpedia, 2018a, https://strike.scec.org/scecpedia/CyberShake_Study_17.3. Accessed 11 Oct. 2021.

SCEC. Scecpedia, 2018b, https://strike.scec.org/scecpedia/CS17.3-H. Accessed 11 Oct. 2021.

Schnabel, P.B., Lysmer, J., and Seed, H.B. (1972). SHAKE: A Computer Program for Earthquake Response Analysis of Horizontally Layered Sites, Report UCB/EERC-72/12, Earthquake Engineering Research Center, University of California, Berkeley, CA.

Shaw, J.H., Plesch, A., Tape, C., Süess, M.P., Jordan, T. H., Ely, G., Hauksson, E., Tromp,J.,

Tanimoto, T., Graves, R., Olsen, K., Nicholson, C., Maechling, P.J., Rivero, C., Lovely, P., Brankman, C.M., Munster, J. (2015). "Unified structural representation of the Southern California crust and upper mantle." *Earth Planet. Sci. Lett.* 415, 1.

Shi, J., and Asimaki, D. (2018). "A generic velocity profile for basin sediments inCalifornia conditioned on V_{S30}." *Seismological Research Letters*, 89(4): 1397-1409.

Silva, W.J. (1988). Soil response to earthquake ground motion. EPRI Report NP-5747, CA.Small,

P., Gill, D., Maechling, P.J., Taborda, R., Callaghan, S., Jordan, T.H., Ely, G.P., Olsen, K.B. and Goulet, C.A. (2017). "The SCEC Unified Community Velocity Model Software Framework. *Seismological Research Letters* 88(6): 1539-1552.

Steidl, J.H., Tumarkin, A.G., and Archuleta, R.J. (1996). "What is a reference site?" *Bulletin Seismological Society of America*, 86: 1733-1748.

Stewart, J.P., and Afshari, K. (2020). "Epistemic uncertainty in site response as derivedfrom one-dimensional ground response analyses." *JGGE*, 147(1): 04020146.

Süss, M.P., and Shaw, J.H. (2003). "P wave seismic velocity structure derived from soniclogs and industry reflection data in the Los Angeles basin, California." *J. Geophys. Res.* 108, 2170.

Taborda, R., Azizzadeh-Roodpish, S., Khoshnevis, N., and Cheng, K. (2016). "Evaluationof the Southern California seismic velocity models through simulation of recorded events." *Geophysical Journal International*, 205: 1342-1364.

Thompson, E.M., Kayen, R.E., Carkin, B., and Tanaka, H. (2010). Surface-wave site characterization at 52 strong-motion recording stations affected by the Parkfield, California, M6.0 Earthquake of 28 September 2004. USGS O.F. Report 2010-1168, 117 pp.

Toro, G.R. (1995). Probabilistic models of the site velocity profiles for generic and site- specific ground-motion amplification studies. Report 779574, Brookhaven National Laboratory, Upton, NY, 17 November.

Watson-Lamprey, J.A. and Abrahamson, N.A. (2006). "Selection of ground motion time series and limits on scaling." *Soil Dynamics and Earthquake Engineering*, 26(5) 477-482.

Zalachoris, G., and Rathje, E.M. (2015) "Evaluation of one-dimensional site response techniques using borehole arrays." *J. Geotech. Geoenviron. Eng.*, 141(12): 04015053.

MOVE FROM SOIL/ROCK: SITE RESPONSE BASED ON THE DIFFERENCE IN THE VS PROFILE FOR THE GMPE AND THE SITE-SPECIFIC VS PROFILE

Norman Abrahamson

University of California, Berkeley

Abstract

The traditional approach used to incorporate site response into the ground-motion hazard analysis is to compute a design spectrum for a rock-site condition and then propagate the rock motion from the base of the soil model to the surface. The rock-site ground motion is computed for a given VS30 value which is often assumed to represent the outcropping motion at a depth at which the VS is equal to the VS30. For example, the ground motion computed for VS30=600 m/s is assumed to apply to the layer at depth with VS=600 m/s. There are two problems with this assumption. First, a site with a given VS30 value will have a gradient in the VS(z) profile so that the Vs at the surface is much lower than the VS30 value. As a result, the assumption that VS=VS30 leads to overestimation of the motion at depth. Second, the VS30 value is not a fundamental physical parameter for site response. The VS30 works in GMMs because the VS30 tends to be correlated with the deeper VS(z) profile that is the fundamental physical parameter for site response. The VS30 should be thought of as an index for the full VS(z) profile and not a key parameter by itself.

Adjusting the ground motion for an average site condition given by the GMMs to the site-specific condition requires first understanding what site condition is represented by the GMM, then computing the site factor to account for the differences. To be able to correct for the differences in the VS(z) profile implicit in the GMM and the site-specific VS(z) profile, requires knowing the VS(z) profile for the GMM. Current GMMs do not provide the VS(z) profiles that go with the GMM, but that is changing. An example of VS(z) and kappa for California that are estimated as part of the GMM development process is shown using the NGA-W2 data set. For each VS30 value, there is a full VS(z) profile and the kappa. These models provide a more complete description of the site condition that goes with the ground motions computed using the GMM. They also make it clear that VS30 is not the important physical parameter for site effects and their use should lead to clear handoffs between hazard analyses and site response studies.

The VS(z) profile correction method described in Williams and Abrahamson (BSSA 2021) is an alternative to the soil-over-rock approach routinely used in earthquake engineering practice. The approach is not new and has been used for Vs-kappa corrections to adjust a GMM from one region to another, but it has not been widely used for site response studies. This approach is similar to the standard soil-over-rock analysis, but it uses different input motions and involves performing two site response analyses -- one for the generic profile associated with the GMM(s) and one for the site-specific profile -- then applying the ratio of the two site response analysis results to correct the design spectrum for the reference site condition developed using the GMMs. An example application of the method is shown.

ASSESSING ASCE-41 ACCEPTANCE CRITERIA FOR LINEAR AND NONLINEAR PROCEDURES USING INSTRUMENTED BUILDING DATA

Laura L. Hernández-Bassal and Sashi K. Kunnath

Department of Civil and Environmental Engineering
University of California, Davis

Abstract

Current provisions in ASCE-41 for performance-based assessment are applied to an existing three-story steel moment frame building that was designed and constructed prior to the 1961 UBC code revisions. A computer model of a perimeter frame that comprises the primary lateral system of the building was developed and validated against available instrumented data from two earthquakes. Both linear and nonlinear procedures were used in the assessment. Findings from the study indicate that the linear static and dynamic procedures produced consistent demand-to-capacity ratios. The nonlinear static procedure resulted in the most severe demands at the lowest level with two beams failing the Collapse Prevention limit state whereas the nonlinear dynamic procedure produced the lowest demands on the building; however, the fact that some individual motions caused some beams to exceed Life Safety or Collapse Prevention limits indicates that ground motion selection can play a major role in the outcome of the assessment when using the nonlinear dynamic procedure.

Introduction

The development of ASCE-41 (ASCE 2017) and other ongoing efforts directed towards the enhancement of performance-based codes represent a significant advancement in the practice of earthquake engineering. However, calibration and validation of the modeling parameters and acceptance criteria to real building performance is clearly needed for practicing engineers to gain confidence in the proposed methodologies. The use of strong motion data obtained from instrumented buildings experiencing strong ground shaking is an essential part of this process.

ASCE-41 permits as many as four analytical procedures to estimate seismic demands: Linear Static Procedure (LSP), Linear Dynamic Procedure (LDP), Nonlinear Static Procedure (NSP), and Nonlinear Dynamic Procedure (NDP). This implies that the assessment of a regular low to mid-rise building using any of the methods should reach the same conclusion on the performance of the system. Recently, Harris and Speicher (2018) carried out a detailed ASCE 41-based assessment of six modern steel frames varying in height from four to sixteen stories designed to the provisions of ASCE-7 (ASCE 2016). Their study identified numerous inconsistencies in the different evaluation procedures: for example, LDP consistently resulted in lower demand-to-capacity ratios (DCRs) than LSP and likewise NSP consistently resulted in lower DCRs than NDP – though it is recognized that nonlinear responses are sensitive to model and analysis parameters.

The results reported in this paper are part of a larger study investigating three instrumented buildings and examining several ASCE-41 provisions. It can be viewed as an extension of the study by Harris and Speicher to an existing building where the numerical model has been calibrated to observed responses.

Building and Instrumentation Data

The first structure selected for assessment is a 3-story office building designed in 1958 and located in San Bernardino, California. The structure is composed of moment frames along the exterior serving as the lateral load resisting system in both directions. The gravity system is a wood truss-joist system supported on steel columns that spans in the north-south direction. Figure 1 shows the plan view of the building and the elevation of the perimeter frame used in the assessment.

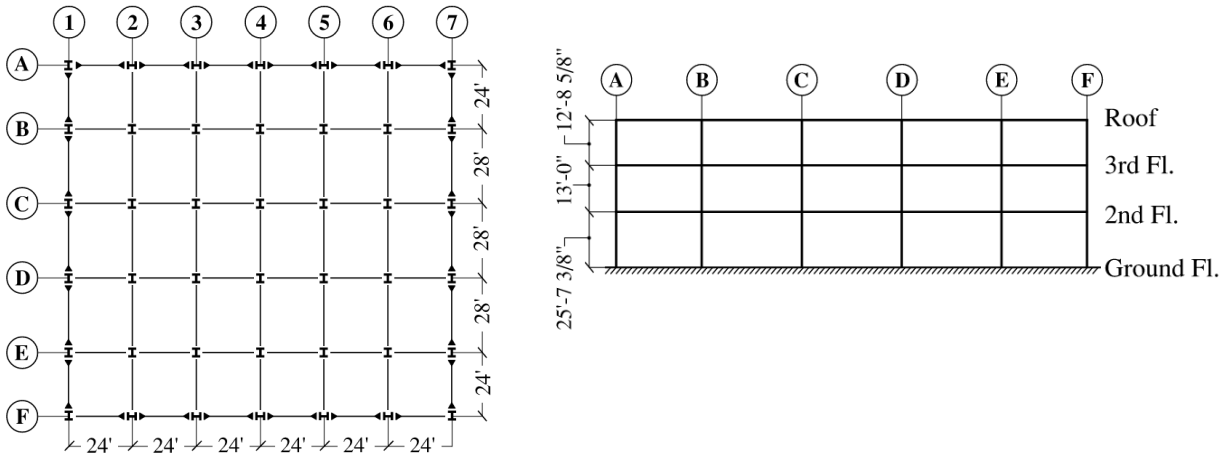

Figure 1. Plan view of building and elevation of perimeter frame on line 1

The building has been instrumented by the California Strong Motion Instrumentation Program (CSMIP Station 23516) with thirteen accelerometers: three at the ground level to record base accelerations in all three orthogonal directions, three each at the 2nd floor and roof, and four at the third level of the building – as shown in Figure 2.

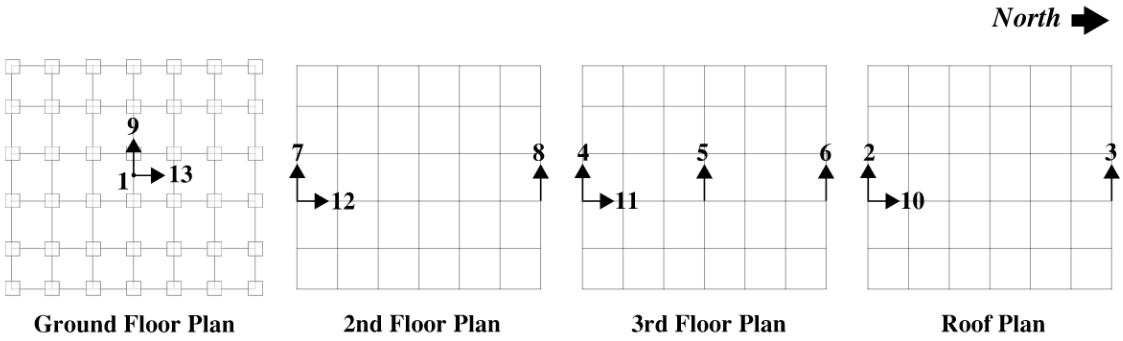

Figure 2. Locations of installed sensors

Instrumented data from several earthquakes are available for this building, as indicated in Table 1. Of the available data, two recorded motions with the highest ground peak accelerations

(PGA) were selected to calibrate the simulation model: Landers (1992) and San Bernardino (2009).

Table 1. Available instrumented data for selected building

Earthquake	Year	Peak Acceleration (g)	
		Ground	Structure
Landers	1992	0.110	0.280
San Bernardino	2009	0.102	0.155
Chino Hills	2008	0.052	0.076
Lake Elsinore	2007	0.036	0.050
Whittier	1987	0.030	0.090
Calexico	2010	0.022	0.108
Borrego Springs	2016	0.019	0.062
Borrego Springs	2010	0.018	0.077
Inglewood	2009	0.010	0.029
Beaumont	2010	0.009	0.016

When examining the time series for the Landers earthquake, unusual long-period content was observed throughout the record, particularly in the floor displacement histories (see roof history shown in Fig. 3). Therefore, a high-pass filter was applied with a corner frequency of 0.5 Hz using an 8th order zero phase delay Butterworth filter. Figure 3 shows the base acceleration as well as the relative roof displacement before and after filtering.

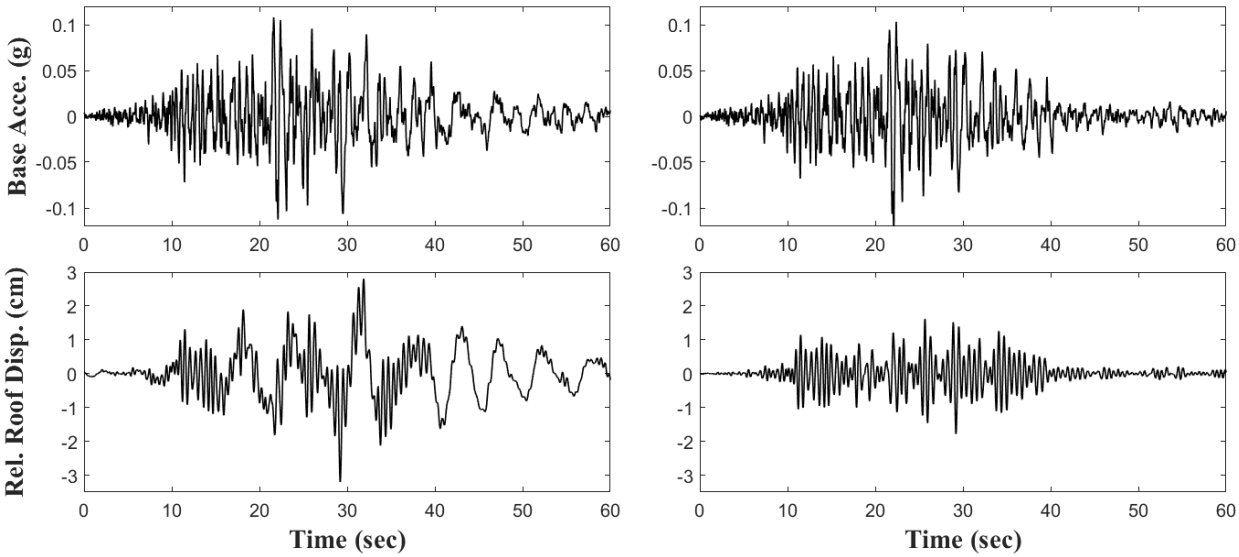

Figure 3. Unfiltered (left) and filtered (right) time histories

Modeling and Validation

Given the general symmetry of the building plan and the fact that torsional motions were not evident in the profile of the recorded floor displacement histories, the analyses were carried out on a two-dimensional model (Fig. 4) of the perimeter moment frame in the east-west direction.

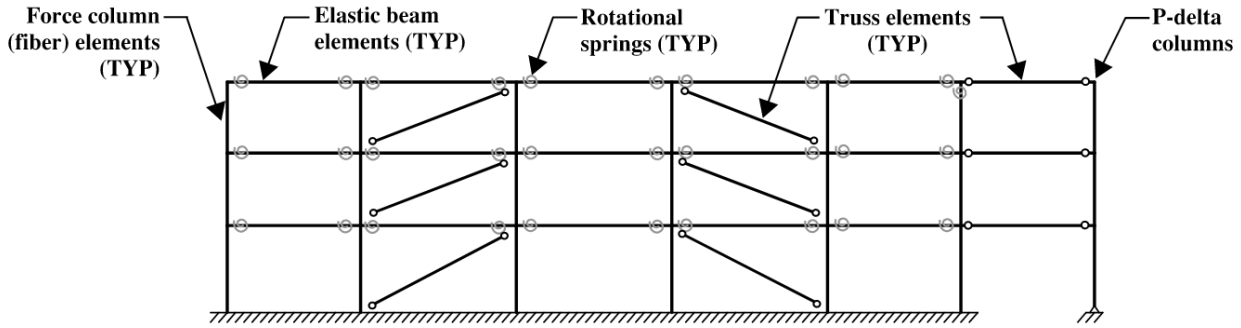

Figure 4. Two-dimensional model of perimeter frame used in assessment

Beams are modeled using elastic beam-column elements with inelastic springs (constructed with zero-length elements) at the ends as shown in Figure 4. All inelastic action (for nonlinear procedures) is lumped into these concentrated springs whose cyclic response is represented using the Modified Ibarra-Medina-Krawinkler deterioration model (Ibarra et al. 2005). In order to capture the axial load-moment interaction, columns were modeled as force-based elements with five Lobatto integration points and the Voce-Chaboche material model was used to represent the inelastic cyclic behavior of steel. Center-line dimensions are used for beams and columns to indirectly account for the flexibility of the panel zones. The building has embedded column bases connected to spread footings and grade beams and therefore the base was assumed to be fully restrained – an assumption that was shown to be reasonable for such a base connection (Falborski et al. 2020). An additional leaning column is attached to the moment frame using rigid links with pinned connections at each end to account for P-Delta effects and contributing gravity loads from the interior frames are applied at each level. A set of diagonal braces were also added at each level to represent the stiffness contribution of non-structural elements – the process by which the brace stiffness was determined is described in the following section.

Calibration of Non-Structural Stiffness

An eigenvalue analysis was carried out on the bare frame structure without the diagonal braces and the fundamental period of the structure was estimated as 0.70 sec. A Fast Fourier Transform (FFT) was carried out using the acceleration time histories at each level and Transfer Functions (relative to the base) were obtained for both the Landers and San Bernardino earthquakes. The resulting plots for the Landers recordings are shown in Fig. 5 where a predominant frequency is evident at approximately 1.8 Hz or a period of 0.56 sec.

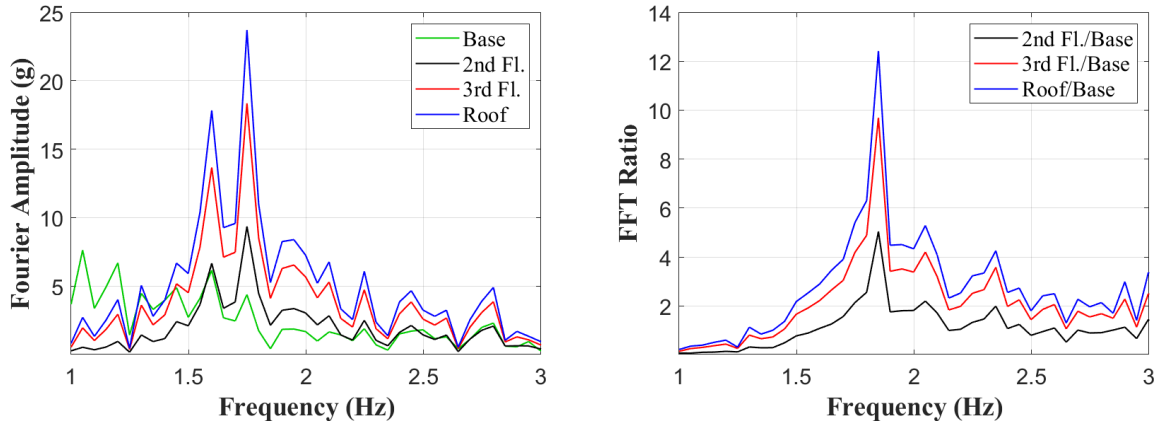

Figure 5. Fourier transform and transfer functions from acceleration histories recorded during Landers earthquake

The procedure outlined in Falborski et al. (2020) was utilized to establish the non-structural stiffness at each story level. At any time instant during the dynamic response of the structure, the shear in any story *K* can be estimated from:

$$V_k^{story}(t) = V_K^{NS}(t) + V_K^{STR}(t) + C_K \cdot \dot{\Delta}_K(t) = \sum_{i=K}^{N} m_i \ \ddot{u}_i(t) \quad (1)$$

In the above equation, $V_K^{story}(t)$ is the instantaneous shear in story *K* at time *t*, $V_K^{NS}(t)$ and $V_K^{STR}(t)$ are the story shears from the non-structural and structural components, respectively, $C_K \cdot \dot{\Delta}_K(t)$ is the story force due to damping, and $\sum_{i=K}^{N} m_i \ \ddot{u}_i(t)$ is the sum of the inertia forces above story *K*.

Using the recorded time histories, the time instants at which the interstory velocities are zero are determined for each story *K*. At these instants, the damping force is eliminated in Equation (1). The lateral displacements at each floor corresponding to these time instants are determined and applied statically to the model. The resulting shears will be structural story shears at each level. The total shear is determined by summing the inertia forces above that level, hence the non-structural contribution can be established. At each time instant when the interstory velocity is zero, the nonstructural story shear can be plotted vs. the corresponding interstory drift at story *K*. Linear regression can be used to fit the data points and the resulting slope represents the nonstructural story stiffness. Likewise, the total and structural stiffness at each floor can be estimated using a similar approach. The estimated story stiffnesses are shown for a typical floor in Fig. 6 for the San Bernardino recordings. Table 2 lists the numerical values of the estimated stiffness quantities.

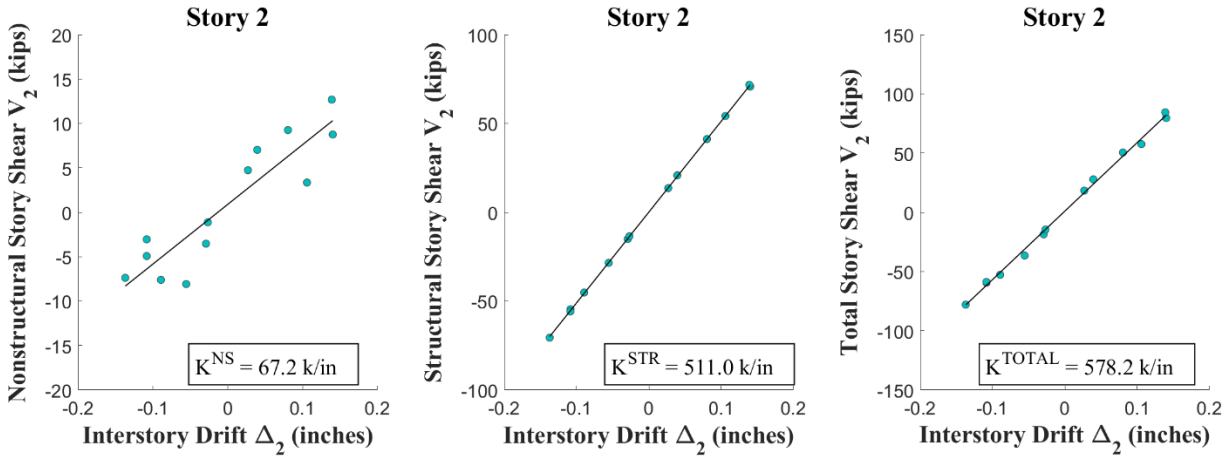

Figure 6. Estimating non-structural stiffness for a typical story (Data from San Bernardino earthquake)

In order to add the nonstructural stiffness, braces were introduced in two bays at each floor through the use of truss elements as shown previously in Fig. 4. The properties of the braces were adjusted until the total story stiffness matched the calculated values shown in Table 2. This was accomplished iteratively by updating the areas of the braces, applying static lateral loading to the model and determining the total story stiffness. The addition of the braces to the model as well as incorporating the additional stiffness of the joist floor system altered the fundamental period of the frame to 0.54 sec, consistent with the estimated building period in the east-west direction from the FFT analysis (Fig. 5).

Table 2. Estimated components of story stiffness

Story	***Stiffness (k/in)***			
	K^{NS}	K^{STR}	K^{TOTAL}	K^{NS}/K^{TOTAL}
1	51.9	551.1	603.0	0.09
2	67.2	511.0	578.2	0.12
3	102.9	340.3	443.2	0.23

Calibration of Damping

The concept behind Equation (1) can also be used to calibrate damping. In this case, the time instants at which the interstory drifts are zero are considered. Therefore, the total damping force in any story at these time instants will be equal to the sum of the inertia forces above that story. However, the damping coefficients will correspond to the lateral degree-of-freedom of the floor and additional calibration will be needed to establish Rayleigh coefficients associated with the mass and stiffness matrices of the system. Hence, in the present study, damping was estimated using the logarithmic decrement method by examining the displacement histories of the floors at the end of the recordings. Shown in Figure 7 are the floor displacement histories at the end of the recording during the San Bernardino earthquake which is assumed to represent the free vibration phase of the response. The decay in the response over the final two cycles is used to estimate damping. The estimated damping ratio varies from 13% in the first floor to 19% in the third floor. The high damping obtained with this approach indicated some anomaly in the data and/or assumption about the free vibration phase. Hence, an additional method was utilized

to estimate damping – the analysis model (with nonstructural stiffness already calibrated) was subjected to both the Landers and San Bernardino base motions and the response spectra, based on the roof accelerations, was compared to that obtained with the actual recorded motions. Results are presented in Fig. 8 which suggest that a damping of 10% (assigned to both the 1st and 2nd mode) produced a reasonable match. Hence the time history simulations presented in this paper are based on Rayleigh damping with coefficients corresponding to 10% of critical damping in the 1st and 2nd mode.

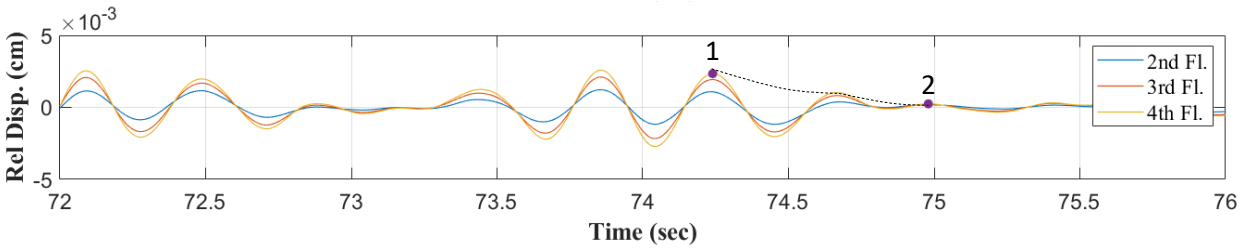

Figure 7. Free vibration response following the San Bernardino earthquake

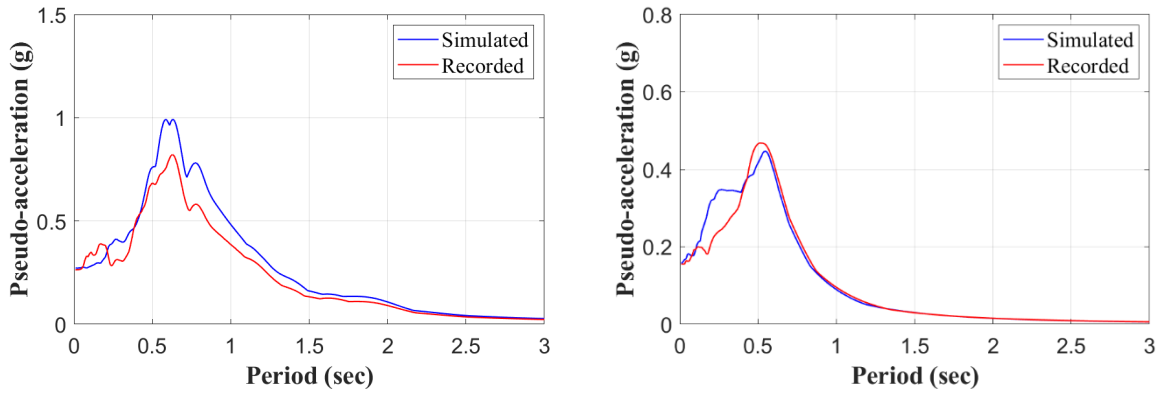

Figure 8. Comparison of acceleration spectra using data from the roof response: (a) Landers; (b) San Bernardino

Model Validation

The model was calibrated assuming elastic behavior during each of the recorded motions based on the following facts: (1) the fundamental period did not shift during these motions, and (2) there was no evident structural damage in the building following the seismic events. The simulated and recorded roof displacement histories during the Landers and San Bernardino shaking are shown in Fig. 9. The peak displacements during the Landers earthquake is slightly over-estimated – this is attributed to the fact that the 10% damping used in the simulation was lower than the observed damping (see Fig. 8). The magnitude of the response during the San Bernardino earthquake was negligible during the first 25 seconds, hence roof displacement history is shown beyond this point.

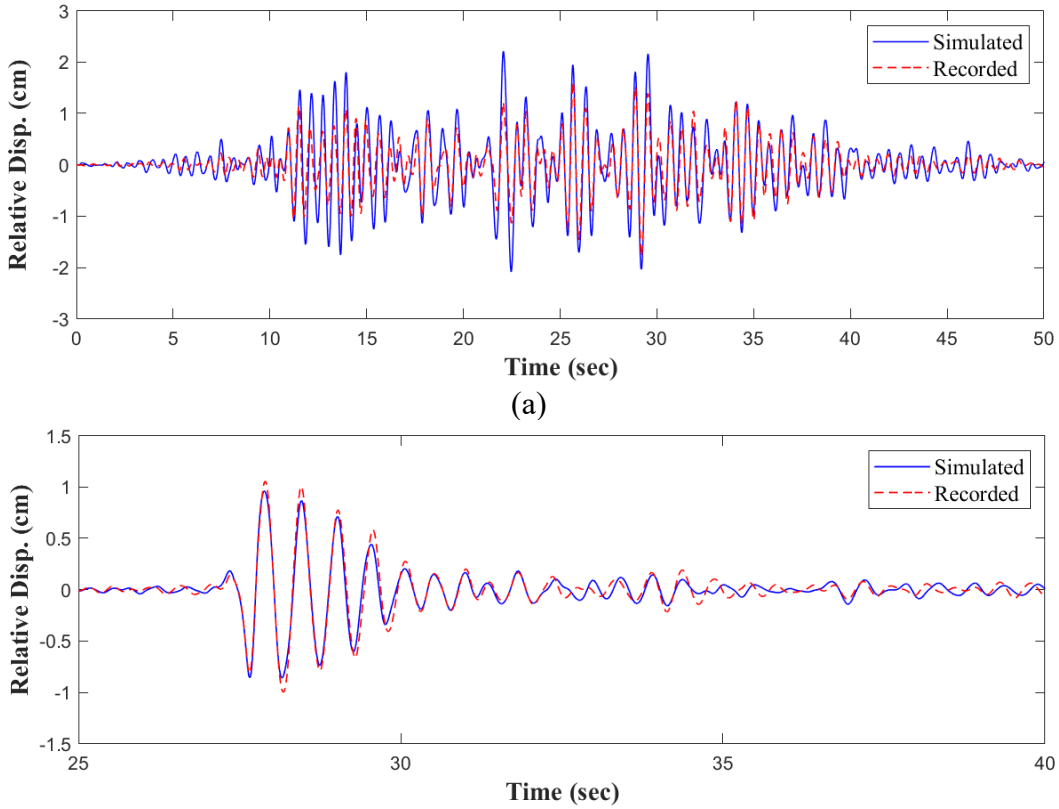

Figure 9. Comparison of recorded vs. simulated roof displacement histories:
(a) Landers; (b) San Bernardino

Building Assessment using ASCE 41 Guidelines

A seismic performance assessment of the building was carried out by analyzing the validated computer model of the perimeter frame and using both linear and nonlinear analysis procedures prescribed in ASCE 41. Note that in all procedures described hereafter, the lateral load application is preceded by the application of the sustained gravity loads on the frame. The seismicity considered in the assessment is based on the BSE-2E hazard level, which represents a 50% probability of occurrence in 50 years. The resulting response spectrum for the site is shown in Fig. 10 with the following key parameters: S_{XS} = 1.9 g; S_{X1} = 1.25 g; T_O = 0.13 sec and T_S = 0.66 sec.

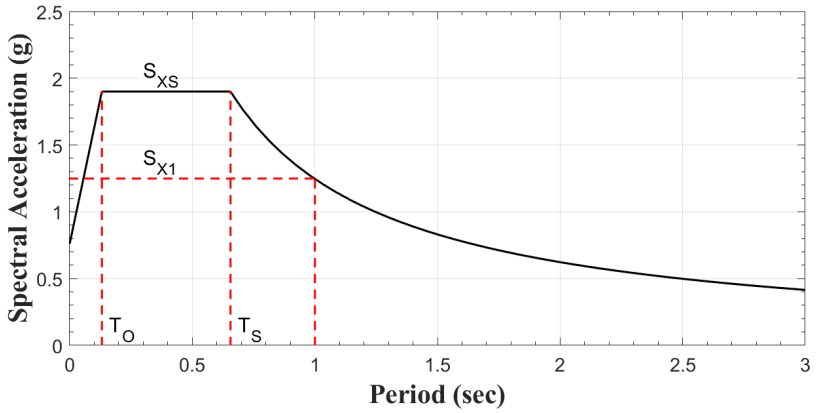

Figure 10. Response spectrum for site

Linear Procedures

For the Linear Static Procedure (LSP), an equivalent static load, representative of the seismic hazard, is applied over the height of the building. First, the pseudo lateral force V is calculated by using the following expression provided in ASCE 41:

$$V = C_1 C_2 C_m S_a W \tag{2}$$

The modification factors that account for inelastic behavior C_1 and hysterisis characteristics C_2 were both determined to be 1.0, whereas the effective mass factor C_m = 0.9. The spectral acceleration S_a was obtained from Fig. 10. The effective seismic weight of the building is 2058 kips and half this value was used to estimate the total lateral load on the perimeter frame. All elements were deformation-controlled, hence the maximum moment demands in each element was obtained due to the applied lateral forces and the corresponding demand-to-capacity ratios (DCRs or m-factors) are plotted in Fig. 11 (a) and 12 (a).

For the Linear Dynamic Procedure (LDP), the assessment was based on the response spectrum method. Considering the first three modes was sufficient to capture at least 90% of the participating mass of the frame. The equivalent static lateral load vector was then determined from:

$$\{p\} = [m]\{\Phi\}\Gamma\ S_a \tag{3}$$

where $[m]$ is the lumped mass matrix, $[\Phi]$ is the modal vector, Γ is the modal participation factor, and S_a is the spectral acceleration at the fundamental period of the frame, obtained from the target response spectrum (Fig. 10). Peak responses are recorded for each set of lateral loads and the modal demands are combined using the square root sum of squares (SRSS). The DCRs are shown in Fig. 11 (b) and 12 (b) alongside the LSP results. It is seen that both linear procedures produce very similar DCR values – several beams exceed Life Safety (LS) performance level at the lower two levels whereas the columns exhibited much better performance just exceeding Immediate Occupany (IO) limits at the first floor level.

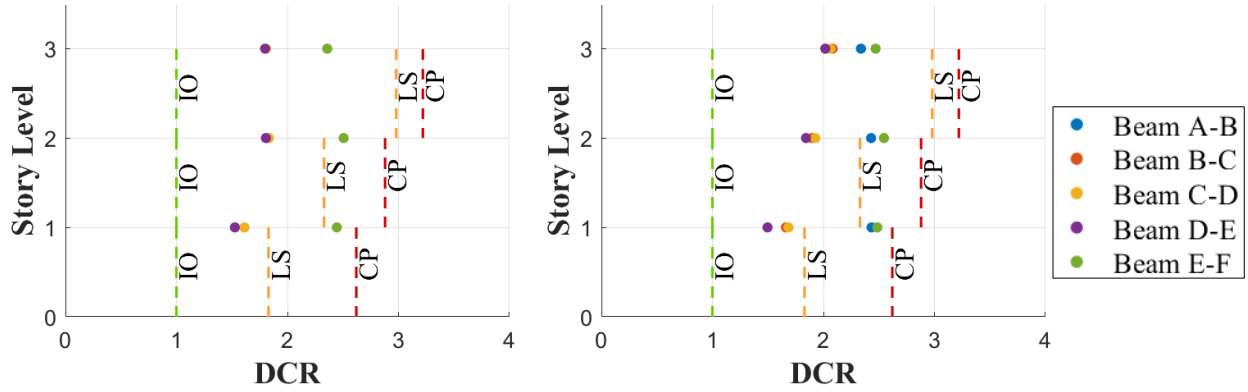

Figure 11. Demand-to-capacity ratios for beams:
(a) Linear Static Procedure; (b) Linear Dynamic Procedure

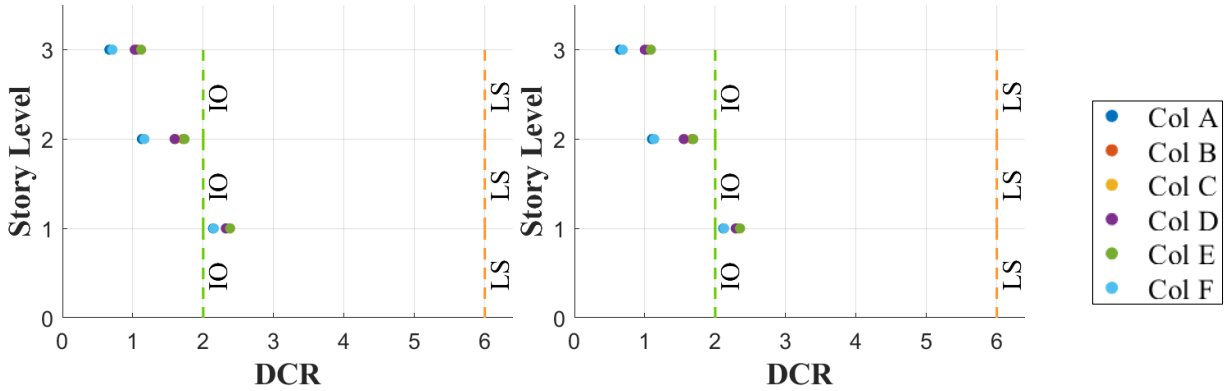

Figure 12. Demand-to-capacity ratios for columns:
(a) Linear Static Procedure; (b) Linear Dynamic Procedure

Nonlinear Procedures

As described previously, nonlinear action in the beams is represented by concentrated springs while columns are modeled using distriuted plasticity elements with fiber sections to capture axial force-moment interaction effects. The response of each nonlinear spring is based on the Modified Ibarra-Medina-Krawinkler (I-K) model – the transformation of the I-K model into the ASCE 41 backbone envelope for use in nonlinear procedures is displayed in Fig. 13.

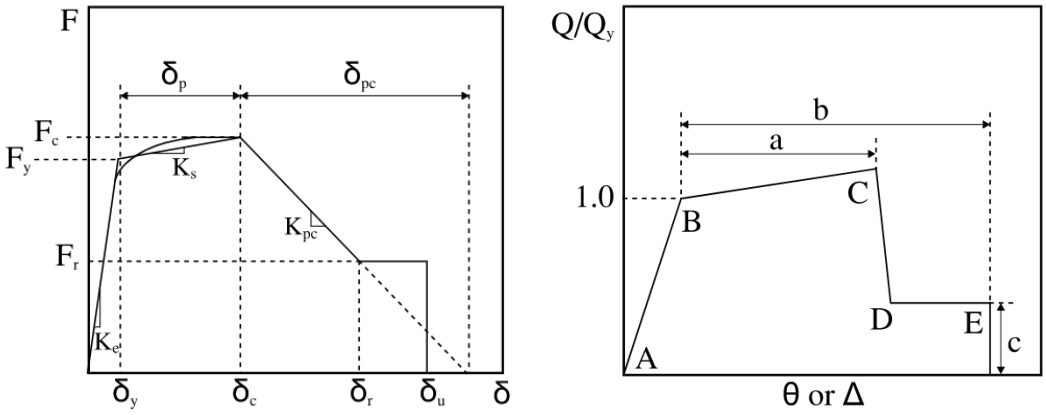

Figure 13. Modified Ibarra-Medina-Krawinkler model (left) and transformed backbone parameters (right) used in nonlinear procedures

For the Nonlinear Static Procedure (NSP), the target displacement δ_t is calculated using:

$$\delta_t = C_0 C_1 C_2 S_a \frac{T_e^2}{4\pi^2} g \quad (4)$$

The modification factors that accounts for the multi to single degree-of-freedom transformation, inelastic behavior, and hysteretic characteristics, respectively, were determined to be: C_0 = 1.3, C_1 = 1.034 and C_2 = 1.0. The effective fundamental period, and consequently the target displacement, was estimated through an iterative process to establish a converged effective period. The final computed target displacement was 11.28" (corresponding to a roof drift of 2.3 %) and an effective to initial stiffness ratio of 1.24. The inelastic demands in the beams and columns at the target displacement are estimated using OpenSees and are compared to the ASCE 41 acceptance criteria in Fig. 15 (a) and Fig. 16 (a).

Ground Motion Selection for NDP

In order to select ground motions that are representative of the seismic hazard at the site, the United States Geological Survey (2017) *Unified Hazard Tool* was used for the site deaggreation. The hazard at the site is controlled primarily by the San Jacinto fault with expected magnitude 8.0 and fault distances less than 1 km and the San Andreas fault with magnitude range 7.0 – 8.0 and fault distances between 7 – 12 km. A total of 51 ground motions were downloaded from the PEER NGA ground motion database (ngawest2.berkeley.edu) with the following filters: fault type: strike slip; magnitude: 6 to 8; distance to rupture: 0 to 12; and shear wave velocity Vs30: 180 to 360 m/s. Ground motions with spectral shapes signficantly different from the target spectrum were discarded. The final 11 sets of ground motion (pairs) were selected such that the average maximum direction spectra (RotD100) was at or above 90% of the target response spectrum in the period range $0.2T_1 - 1.5T_1$. Given that the site is classified as near-fault, the horizontal components of each selected set was rotated to the fault-normal and fault-parallel directions of the causative fault. The fault closest to the site is the San Jacinto fault, hence this fault angle was used as the reference for rotating the ground motions. ASCE 41-17 does not provide specific guidance on ground motion selection for 2D analysis. Therefore, the following procedure was implemented: for each ground motion set already rotated in the fault parallel and normal orientations, the base motions and their spectra in each direction were compared; the

motion with a larger evident pulse in the time history or a larger spectral value within the target period range was selected. A additional scale factor of 1.1 was necessary to ensure that the actually applied ground motions had a mean spectra that was equal to or above the target spetrum in the required period range. Figure 14 shows the final ground motion spectra and Table 3 summarizes essential details of the selected records.

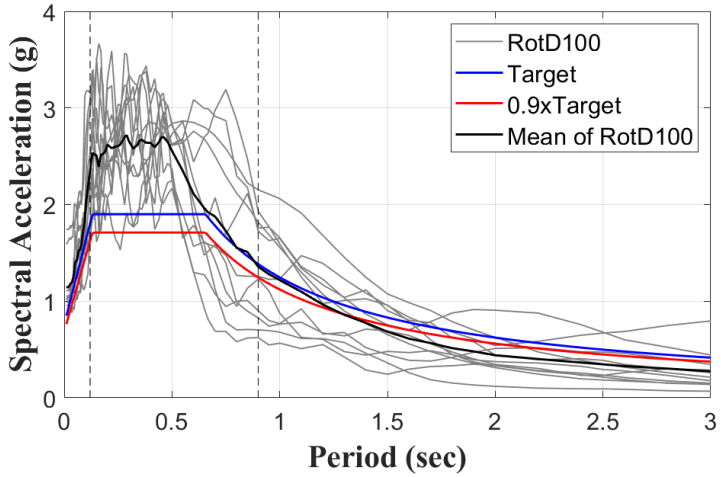

Figure 14. Maximum direction spectra of scaled motions and comparison of mean spectrum with target spectrum at site

Table 3. Selected ground motions

GM #	Record Sequence Number	Earthquake Name	Year	Station Name	Magnitude	R_{rup} (km)
1	6	"Imperial Valley-02"	1940	El Centro Array #9	6.95	6.1
2	30	"Parkfield"	1966	Cholame-Shandon Array #5	6.19	9.6
3	95	"Managua_-Nicaragua-01"	1972	"Managua_ ESSO"	6.24	4.1
4	162	"Imperial Valley-06"	1979	"Calexico Fire Station"	6.53	10.5
5	165	"Imperial Valley-06"	1979	"Chihuahua"	6.53	7.3
6	185	"Imperial Valley-06"	1979	"Holtville Post Office"	6.53	7.5
7	558	"Chalfant Valley-02"	1986	"Zack Brothers Ranch"	6.19	7.6
8	725	"Superstition Hills-02"	1987	"Poe Road (temp)"	6.54	11.2
9	4098	"Parkfield-02_ CA"	2004	"Parkfield - Cholame 1E"	6.00	3.0
10	4102	"Parkfield-02_ CA"	2004	"Parkfield - Cholame 3W"	6.00	3.6
11	4108	"Parkfield-02_ CA"	2004	"Parkfield - Fault Zone 3"	6.00	2.7

Nonlinear simulations of the calibrated numerical model were carried out using OpenSees for each of the eleven ground motions, and mean values of the plastic rotations in the beams and columns at each end of the element were determined. The maximum plastic rotation among all eleven motions was also recorded. Results are presented in Fig. 15 (b) and Fig. 16 (b) alongside the estimates from NSP. Two beams at the first floor level fail the Collapse Prevention (CP) limit when using NSP but pass Immediate Occupancy (IO) under NDP when considering the average rotation for the eleven motions. If the peak rotation among all motions are considered, the LS limit was exceeded in two beams and the CP limit was exceeded in one beam at the first floor level. Column demands in general were small and meet or slightly exceeded the criteria for IO performance level at all levels for both NSP and NDP.

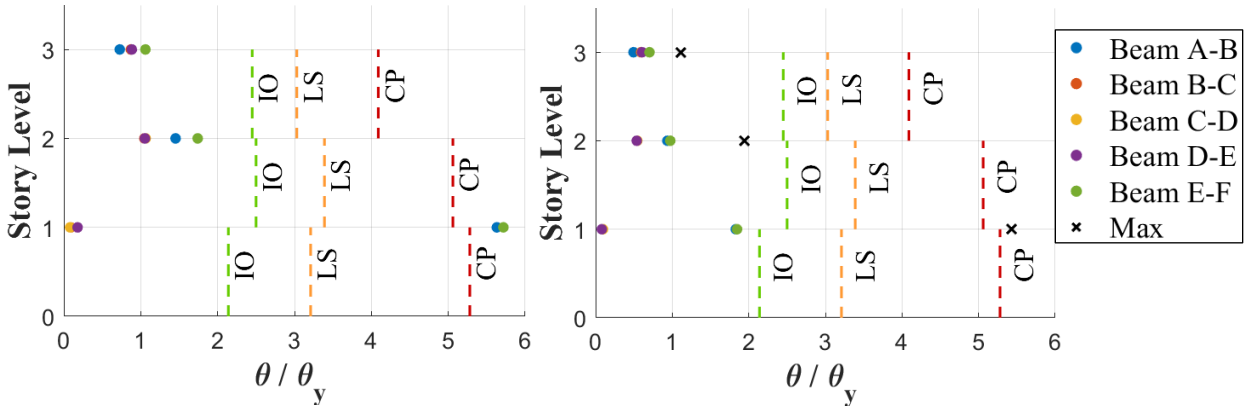

Figure 15. Ductility demands for beams:
(a) Nonlinear Static Procedure; (b) Nonlinear Dynamic Procedure

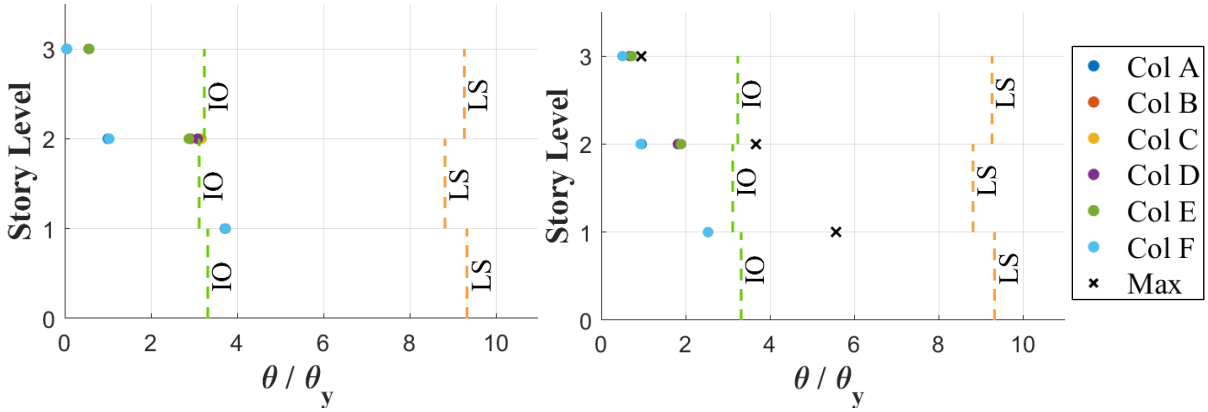

Figure 16. Ductility demands for columns:
(a) Nonlinear Static Procedure; (b) Nonlinear Dynamic Procedure

Conclusions

An existing three-story steel moment frame building that was designed and constructed prior to the 1961 UBC code revisions was analyzed using the modeling and acceptance criteria outlined in ASCE-41. Significant effort was directed towards identifying the nonstructural

stiffness of the system, estimating damping and validating the computer model of the perimeter frame used in the assessment of the building.

Results of the simulations indicate that both linear procedures resulted in consistent DCRs for both beams and columns at all floor levels. The nonlinear static procedure resulted in the most severe demands at the first floor with two beams failing the CP limit state. Simulations using NDP resulted in the lowest demands when considering the mean demands for all eleven ground motions. However, when the response to individual motions are examined, beams on the first floor failed LS performance in two cases and CP performance level in one event. This highlights the importance of ground motion selection and scaling when using NDP.

Acknowledgements

Funding for this study was provided by the California Department of Conservation, California Geological Survey (Strong Motion Instrumentation Program) under Contract 1019-013. However, the contents of the paper do not necessarily represent the policy of that agency nor is an endorsement by the State Government of California.

References

ASCE (2017). Seismic Evaluation and Retrofit of Existing Buildings, ASCE/SEI 41-17, American Society of Civil Engineers, Reston, Virginia.

ASCE (2016). Minimum Design Loads and Associated Criteria for Buildings and Other Structures, ASCE/SEI 7-16, American Society of Civil Engineers, Reston, Virginia.

Falborski, T., Hassan, A.S., Kanvinde, A.M (2020). Column Base Fixity in Steel Moment Frames: Observations From Instrumented Buildings, Journal of Constructional Steel Research. 168. 105993. 10.1016/j.jcsr.2020.105993.

Harris, J. and Speicher, M. (2019). Assessment of Performance-Based Seismic Design Methods in ASCE 41 for New Steel Buildings: Special Moment Frames, Earthquake Spectra. **34** (3).

Ibarra, L. F., and Krawinkler, H. (2005). Global Collapse of Frame Structures under Seismic Excitations. Technical Report 152, The John A. Blume Earthquake Engineering Research Center, Department of Civil Engineering, Stanford University, Stanford, CA.

U.S. Geological Survey (2017). Unified Hazard Tool, accessed September 7, 2020 at URL https://earthquake.usgs.gov/hazards/interactive/

COLLABORATIVE RECORDED DATA BASED RESPONSE STUDIES OF FOUR TALL BUILDINGS IN CALIFORNIA

Daniel Swensen[(1)] and Mehmet Çelebi[(2)]

[(1)] California Geological Survey, Strong Motion Instrumentation Program
[(2)] U.S. Geological Survey, Earthquake Science Center

Abstract

Seismic instrumentation, recorded earthquake responses, and collaborative studies of the response records from four tall California buildings are summarized in this summary paper. These buildings include the tallest San Francisco building, the 61-story Salesforce Tower, and the tallest California building, the 73-story Wilshire Grand Tower, as well as a 51-story residential building in Los Angeles and a 24-story government building in San Diego. Various system identification methods are used to analyze the largest earthquake response records retrieved from seismic arrays installed in each of the four buildings. Significant structural dynamics characteristics (fundamental periods and critical damping percentages) are extracted. In general, critical damping percentages for the first mode are <2.5%, consistent with recent studies and recommendations.

Introduction

The California Strong Motion Instrumentation Program (CSMIP) has installed seismic monitoring arrays on numerous tall buildings in California over the past few decades. Response studies of four of these tall buildings have recently been completed. These buildings include the Salesforce Tower in San Francisco (CSMIP Station No. 58680), the Wilshire Grand Tower in Los Angeles (CSMIP Station No. 24660), a 51-story residential building in Los Angeles (CSMIP Station No. 24M07) and a 24-story government building in San Diego (CSMIP Station No. 03631). Table 1 summarizes selected features of these four buildings. Data recorded in these buildings from recent earthquakes were analyzed using various methods to determine dynamic response characteristics and drift ratios. The analysis methods employed in these studies and selected results are summarized in this paper. Additional details of the response studies of these four tall buildings are separately provided in Çelebi et al. (2019), Çelebi et al. (2020), Çelebi et al. (2021), and Çelebi and Swensen (2021).

Summary of Building Structural Systems

Salesforce Tower

The Salesforce Tower is the tallest building in San Francisco, reaching a height of 1,070 feet. The building includes three stories below grade for parking and 61 stories above grade for offices. It has a roughly square floor plan with dimensions of up to 167 by 167 feet and rounded corners (Figure 1). The basement footprint is slightly larger than the tower, with dimensions of 198 by 184 feet. The typical story height is 14′-9". The vertical load carrying system consists of

concrete over metal deck supported by steel beams and columns, and concrete core walls. The exterior walls of the building are vertically straight between Levels 1 and 27. Beyond Level 27, the exterior walls gradually taper inward. The lateral force resisting system of the building comprises special concrete shear walls at the central core. The northern cell of the core shear wall terminates at Level 50, whereas the southern cell tops out at Level 64. The concrete wall thickness varies from 48" at the base of the structure to 24" near the top. The tower is crowned with a ~150 feet tall steel braced frame structure. The tower foundation is a concrete mat supported by 42 rectangular deep foundation elements called barrettes. The concrete mat varies in thickness from 14 feet at the core to 5 feet at the perimeter. The barrettes are 5 by 10.5 feet in plan and 185 to 230 feet long and are socketed into the bedrock below. See Çelebi et al. (2019) and Huang et al. (2018) for additional details.

Wilshire Grand Tower

The Wilshire Grand Tower in downtown Los Angeles is a 73-story mixed-use office and hotel building with a surrounding podium. The top of the structure features an architectural roof top sail and spire. The sail is a steel structure standing 97 feet above the main roof, and the tubular steel spire extends 176 feet above the sail (Figure 2). With the spire, this is the tallest building west of the Mississippi River with a height of approximately 1,100 feet. The tower has a roughly rectangular floor plan with dimensions of up to 244 by 112 feet. The typical story height varies from 11.5 feet to 14 feet. The vertical load carrying system consists of concrete over metal deck supported by steel beams, steel box columns filled with concrete, and concrete core walls. The lateral force resisting system of the building consists of concrete core shear walls with steel buckling restrained brace (BRB) outriggers and belt trusses. Concrete walls are 48" thick at the base of the structure and 24" thick near the top of the building. A total of 170 braces are placed at three locations along the height of the structure as part of the outrigger system and three-story tall steel belt trusses wrap the building at two levels. The tower is supported on an 18-foot thick concrete mat foundation which bears on bedrock. See Çelebi et al. (2020) and Huang et al. (2018) for additional details.

51-Story Residential Building

The 51-story residential building located in downtown Los Angeles comprises 51-stories above grade with an additional three levels below. Levels 1 to 6 comprise the podium of the building, whereas the tower of the building extends from Level 6 to the roof. The plan areas of the podium and tower have approximate dimensions of 321 by 118 feet and 156 by 95 feet, respectively. There is no seismic joint or separation between the tower and podium levels of the structure. The vertical and lateral load-carrying system consists of a dual-core concrete shear wall and perimeter concrete column system. The two load-carrying systems are interconnected with concrete flat slabs. The tower is supported on a concrete mat foundation that varies in thickness from 5 to 13 feet. The podium rests on a combination of continuous and spread footings and a few smaller mat footings. See Çelebi et al. (2021) for additional details.

24-Story Government Building

The 24-story government building in San Diego is 24 stories above and 2 stories below ground level. In-plan shape of the building is best described as irregular-rectangular and asymmetric.

The base dimensions of the building are approximately 296 by 199 feet, whereas typical floor dimensions are 253 by 100 feet. The vertical load carrying system consists of concrete over metal deck supported by steel beams and columns. The lateral load resisting system consists of special steel moment frames in each direction. In addition, viscous dampers are located along the height of the structure from Level 6 to the roof, in the transverse direction only. The building is supported on a concrete mat foundation that varies in thickness from 3 to 18 feet. See Çelebi and Swensen (2021) for additional details.

Table 1. Summary of selected features of four instrumented tall buildings involved in recent response studies

Building	Salesforce Tower	Wilshire Grand Tower	51-story Resid Bldg	24-story Govt Bldg
No. of Stories (Above/Below Ground Level)	61/3	73/5	51/3	24/2
Construction Material	Mixed	Mixed	Reinforced Concrete	Steel
Structural System	Concrete core shear walls with steel gravity framing	Concrete core shear walls with steel beams and concrete-filled steel box columns, three BRB outriggers, and two truss-belt systems	Concrete core shear walls and concrete columns	Steel moment frames with viscous dampers
Shear Wall to Floor Area Ratio (%)	1.24-3.95	4.0-5.8	~2.9	N/A
No. of Channels	32 accelerometers	36 accelerometers	30 accelerometers	24 accelerometers
Recorded Events	M4.4 Berkeley Earthquake of January 4, 2018	M4.5 S. El Monte Earthquake of Sept. 18, 2020 **M7.1 Ridgecrest Earthquake of July 5, 2019** M6.4 Ridgecrest Earthquake of July 4, 2019	M7.1 Ridgecrest Earthquake of July 5, 2019	M7.1 Ridgecrest Earthquake of July 5, 2019

Summary of Seismic Monitoring Arrays

Salesforce Tower

The Salesforce Tower instrumentation was completed by CSMIP in February of 2018. Thirty-two accelerometers were installed on 10 levels of the building. The vertical distribution of sensors in the building can be seen in the building section shown in Figure 1, which also includes plan views of selected instrumented floors of the building. Figure 1 was modified from the sensor layout of the building developed by CSMIP, which can be found on its website (www.strongmotioncenter.org) and includes plan views of all instrumented levels. To date, the Salesforce Tower has recorded motions from one significant earthquake, the M4.4 Berkeley Earthquake of January 4, 2018. Unfortunately, at the time of the Berkeley earthquake, only 27 of the 32 accelerometers had been installed (channels 1 to 27). However, shortly thereafter, a set of ambient data for all 32 channels was recorded.

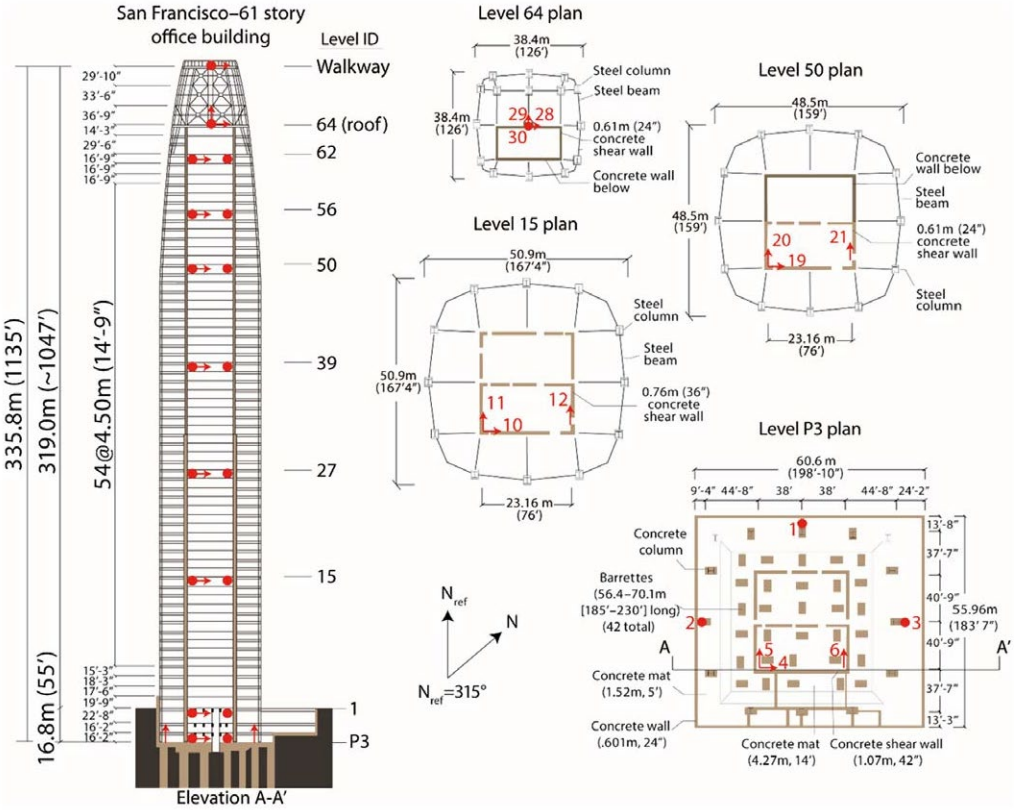

Figure 1. Vertical section, in-plan orientations, and dimensions at Levels P3, 15, 50, and 64 and shear wall distributions and thickness of the Salesforce Tower. Location and orientation of accelerometers are shown by red dots and arrows. Figure from Çelebi et al., (2019) which was modified from a figure at www.strongmotioncenter.org which includes plan views of all instrumented levels.

Wilshire Grand Tower

The instrumentation of the Wilshire Grand Tower by CSMIP was completed in June of 2017 by installing thirty-six accelerometers on 11 levels of the building. The vertical distribution of sensors in the building can be seen in the two building sections shown in Figure 2, which also includes a photograph of the building. The plan views of all instrumented levels can be seen in Figure 3. Figures 2 and 3 were modified from information for the building provided by CSMIP on (www.strongmotioncenter.org). To date, the Wilshire Grand Tower has recorded earthquake motions from three different significant events, which are listed in Table 1. The records from the M7.1 Ridgecrest Earthquake of July 5, 2019 were used for the analyses in Çelebi et al. (2020) and are summarized in this paper.

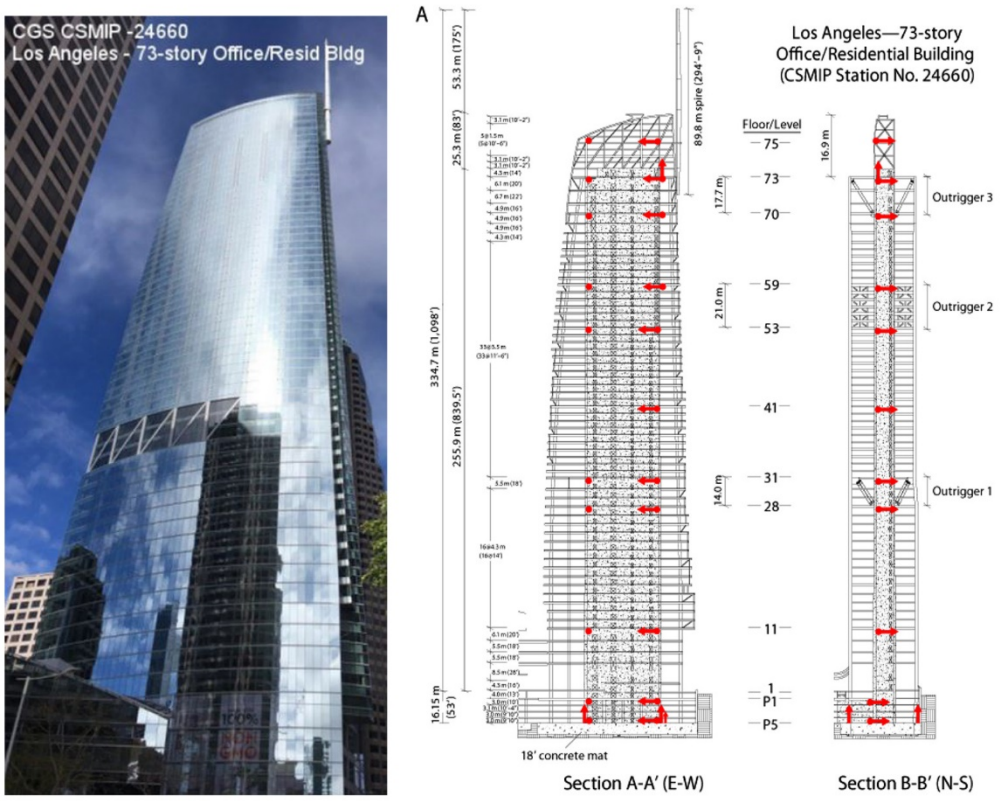

Figure 2. Photograph of the Wilshire Grand Tower and NS and EW vertical sections (www.strongmotioncenter.org). Vertical sections of the building depict vertical dimensions, the locations of outriggers and belt trusses, as well as the levels at which accelerometers are deployed (arrows indicate orientations). Figure from Çelebi et al. (2020), which was modified from www.strongmotioncenter.org.

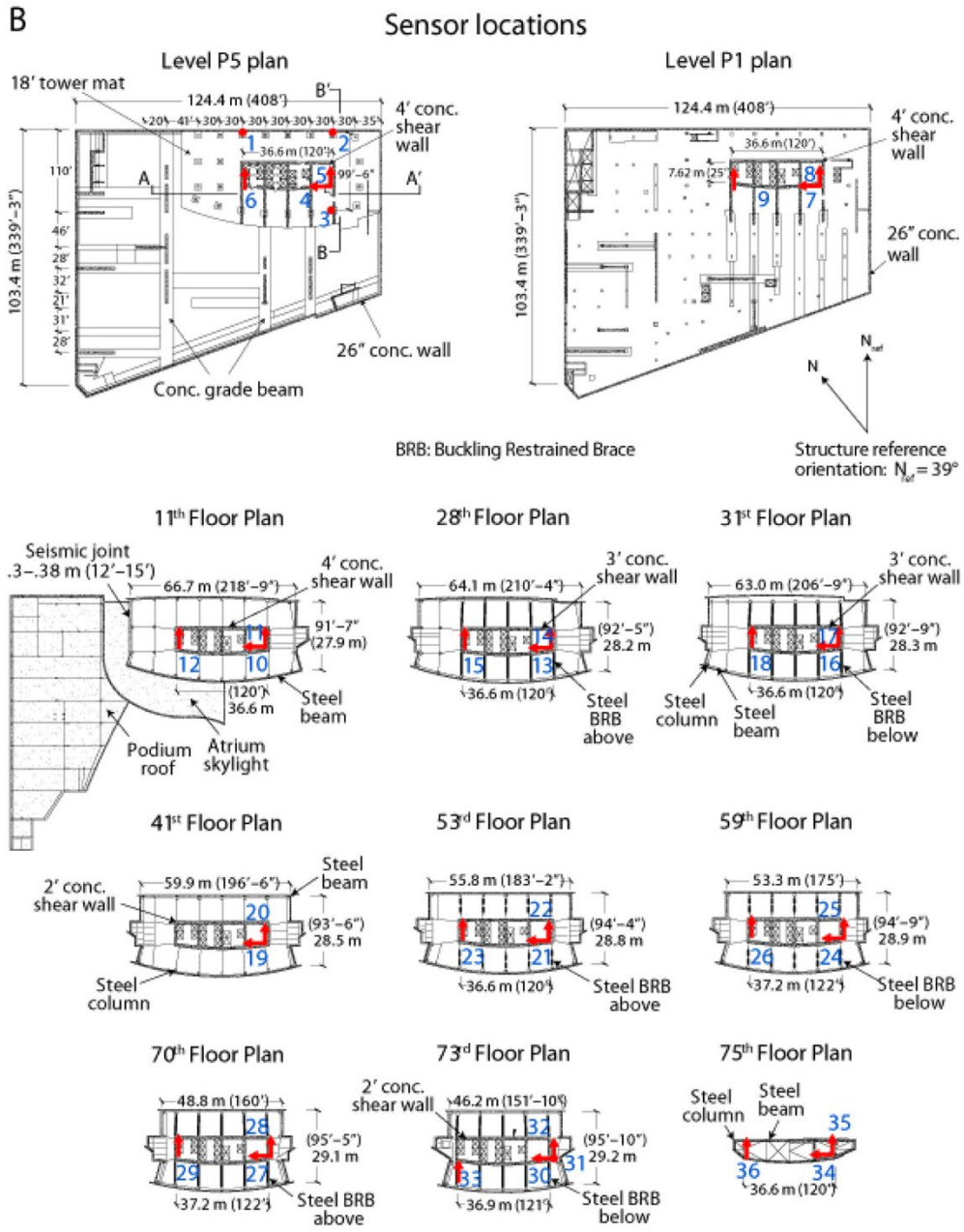

Figure 3. Plan views of floors of the Wilshire Grand Tower showing the core–shear walls and deployed accelerometers with locations and orientations. Figure from Çelebi et al. (2020), which was modified from www.strongmotioncenter.org.

51-Story Residential Building

The 51-story residential building was instrumented by CSMIP in April of 2019 with the installation of thirty accelerometers on eight levels of the building (Figure 4). The vertical distribution of sensors in the building can be seen in the building section shown in Figure 4, which also includes plan views of all instrumented floors of the building. Figure 4 was modified

from the sensor layout of the building developed by CSMIP, which can be found on their website (www.strongmotioncenter.org). Note that Levels 13, 14, and 44 are not included in the floor numbering scheme utilized for the building (i.e. there is no Level called 13, 14 or 44 in the building). This means, for example, that the floor level identified in Figure 4 as Level 52, is actually the 49th level of the building. To date, the 51-story residential building has recorded motions from one significant earthquake, the M7.1 Ridgecrest Earthquake of July 5, 2019.

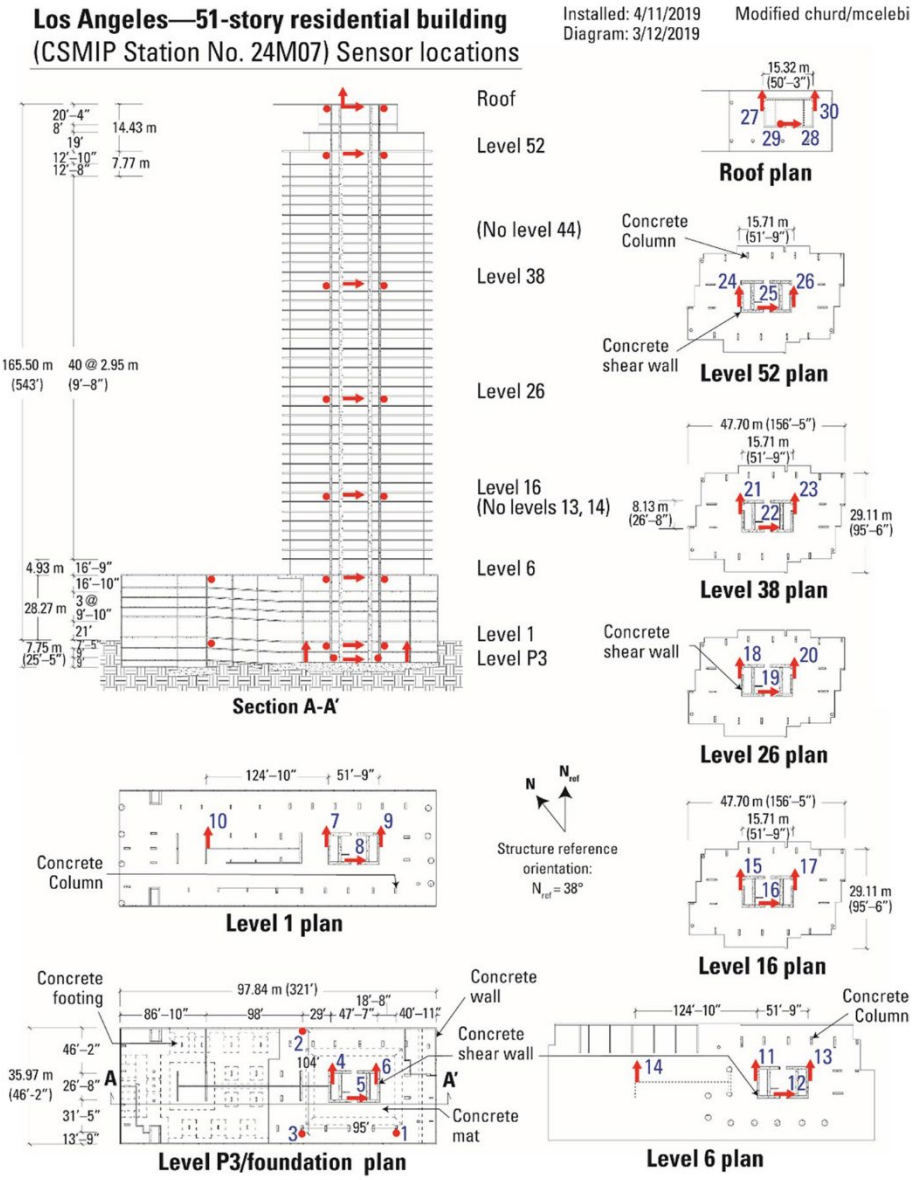

Figure 4. Eight plan views of different levels at the 51-story Residential Building show dimensions and deployed accelerometers in the N-S, E-W, and vertical orientations, according to the reference north as shown. Plan views of floors also show the core shear walls. A vertical section of the building depicts vertical dimensions and distribution of accelerometers. Figure from Çelebi et al. (2021).

24-Story Government Building

The instrumentation of the 24-story government building by CSMIP was completed in June of 2017. Twenty-eight accelerometers were installed on nine levels of the building. The vertical distribution of sensors in the building can be seen in the building section shown in Figure 5, which also includes plan views of all instrumented floors of the building. Figure 5 was modified from the sensor layout of the building developed by CSMIP, which can be found on their website (www.strongmotioncenter.org). Note that sensors 25 to 28 were installed on a pedestrian bridge, which is separated from the building by a seismic joint. To date, the 24-story Government Building has recorded motions from one significant earthquake, the M7.1 Ridgecrest Earthquake of July 5, 2019.

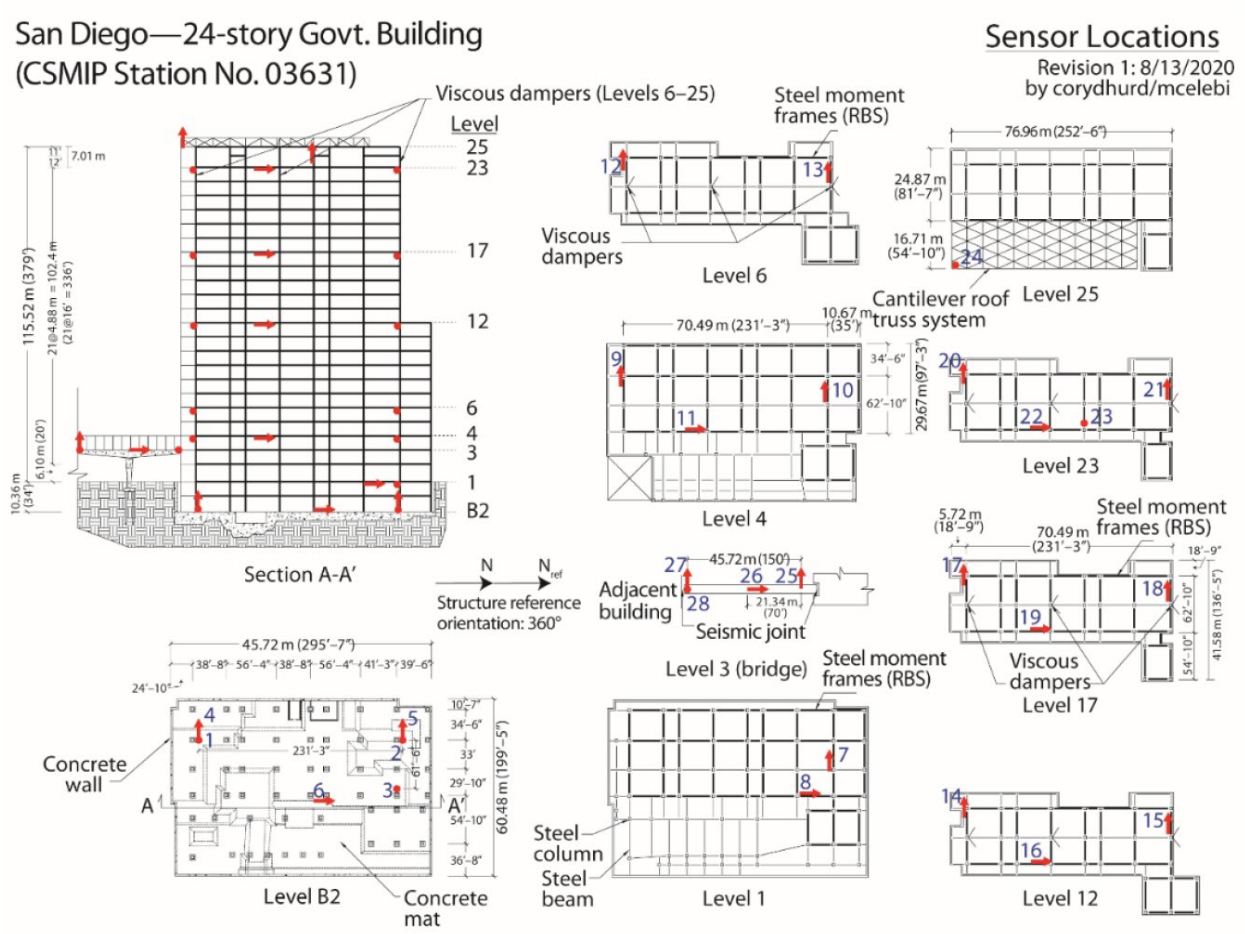

Figure 5. Instrumented vertical section and plan views that show dimensions, as well as arrows and dots depicting locations and orientations of accelerometers deployed throughout the 24-story Govt. Building. Figure from Çelebi and Swensen (2021).

Summary of Analysis Methods and Results

Data recorded in these four tall buildings from recent significant earthquakes were analyzed using several methods to determine their dynamic response characteristics. Through

various spectral analysis techniques, including spectral ratios, time-frequency distribution plots, and cross-spectra, with associated coherency and phase angle plots, the first three modal periods and modal damping percentages were determined for each building. These modal periods and modal damping percentages were validated for each building using the N4SID system identification process. Also, through application of the N4SID process, the first three mode shapes were identified for the north-south, east-west, and torsional directions of each building.

In addition to dynamic response characteristics, average drift ratios were also computed from the response data of these four tall buildings to recent earthquakes. Data from pairs of consecutive instrumented levels were used for these analyses. Because adjacent floor levels were not instrumented in these buildings, pairs of consecutive instrumented levels are typically several floor levels apart. As a result, the calculated drift is an average drift which occurs over several levels.

The modal periods, modal damping percentages, and maximum drift ratios determined from the recent response studies of these four tall buildings are summarized in Table 2. Additional details of the analyses performed, as well as the results obtained from these studies, can be found in the references previously mentioned in this paper.

Table 2. Summary of modal periods, modal damping percentages and maximum drift ratios determined from recent response studies of four instrumented tall buildings

		Salesforce Tower			Wilshire Grand Tower			51-story Residential Bldg			24-story Govt Bldg		
		NS	EW	TOR	NS	EW	TOR	NS	EW	TOR	NS	EW	TOR
Modal Period (sec)	1	5.00	5.00	1.30	6.25	3.70	2.38	4.76	3.57	2.22	3.45	3.33	3.33
	2	1.20	1.11	0.57	1.56	0.83	0.93	1.06	0.83	0.82	1.11	1.09	1.05
	3	0.52	0.50	0.33	0.64	0.38	0.48	0.46	0.38	0.29	0.67	0.64	0.63
Modal Damping (%)	1	1.30	0.60	1.50	3.55	1.48	2.25	2.40	2.10	2.20	4.40	1.30	1.10
	2	1.80	1.00	1.20	2.06	2.37	2.62	1.60	2.00	1.70	4.50	4.00	2.40
	3	1.00	1.20	2.10	2.60	1.00	0.49	2.60	1.20	1.70	5.40	2.90	1.70
Max Drift Ratio (%)		0.015	-	-	0.11	0.06	-	0.145	0.145	-	-	0.065	-

Discussion of Results and Conclusions

This paper summarizes the response studies of four tall buildings in California which have recently been completed. These buildings were instrumented by CSMIP and include the Salesforce Tower in San Francisco, the Wilshire Grand Tower in Los Angeles, the 51-story Residential Building in Los Angeles and the 24-story Government Building in San Diego. Data recorded by these buildings from recent earthquakes were analyzed using various methods to determine dynamic response characteristics and drift ratios. Selected results are summarized in Table 2.

The results summarized in Table 2 reflect the dynamic response characteristics due to the largest shaking experienced by these buildings to date; however, in each case this shaking was relatively light. As a result, the structural responses did not exhibit significant nonlinearity or shifts in vibrational periods. Given the seismic hazard associated with the locations of these buildings it is anticipated that stronger shaking may be experienced in the future. With higher shaking intensities in the future, the buildings may exhibit different behaviors and performances, and the vibrational periods may lengthen beyond those identified in these studies.

In general, critical damping percentages for the first mode of these buildings were determined to be <2.5%. This is consistent with other studies of earthquake response data from instrumented buildings in the United States, Japan, Turkey, and other countries. It is also consistent with design recommendations published by the Los Angeles Tall Buildings Structural Design Council and the Pacific Earthquake Engineering Research Center, both of which recommend 2.5% damping based on analyses such as these.

Drift ratios are important to quantify because they can be assessed as an indicator of damage. In the case of these four buildings the measured motions, and therefore the computed drift ratios, were determined to be too small to have caused damage.

References

Çelebi, M., Haddadi, H., Huang, M., Valley, M., Hooper, J. and Klemencic, R. (2019). The Behavior of the Salesforce Tower, the Tallest Building in San Francisco, California Inferred from Earthquake and Ambient Shaking, Earthquake Spectra, Volume 35, No. 4, pages 1711–1737, November 2019 (https://doi.org/10.1193/112918EQS273M).

Çelebi, M., Ghahari, S. F., Haddadi, H. and Taciroglu, E. (2020). Response study of the tallest California building inferred from the Mw7.1 Ridgecrest, California earthquake of 5 July 2019 and ambient motions, Earthquake Spectra, Vol. 36(3) 1096–1118, (https://doi.org/10.1177/8755293020906836).

Çelebi, M., Swensen, D. and Haddadi,H. (2021). Response study of a 51-story-tall Los Angeles, California building inferred from motions of the Mw7.1 July 5, 2019 Ridgecrest, California earthquake, Bulletin of Earthquake Engineering, online version February 19, 2021. (https://doi.org/10.1007/s10518-021-01053-9).

Çelebi, M. and Swensen, D. (2021). Response study of a tall San Diego, California building inferred from the M7.1 July 5, 2019 Ridgecrest, California earthquake motions*, in print,* The Open Construction & Building Technology Journal, Volume 15, 2021.

Huang, M., Swensen, D., Haddadi, H. and Reitz, T. (2018). Strong motion instrumentation of two new super tall buildings in California and results from ambient and earthquake response data, SMIP18 Seminar Proceedings, 117-138.

NEXT GENERATION SEISMIC HAZARD ANALYSIS OF EMBANKMENT DAMS: CASE OF THE LONG VALLEY DAM, CA

Kim B. Olsen, Te-Yang Yeh, and Daniel Roten

Department of Geological Sciences, San Diego State University

Abstract

We have simulated the 0-7.5 Hz seismic response of the Long Valley Dam (LVD), CA,in a 3D velocity model using a supercomputer for a 2015 M3.7 event and the 1986 M6.2 Chalfant Valley earthquake. The simulations include frequency-dependent attenuation Q(f), surface topography, and near-surface low velocity material. We find the most favorable fit to data on and nearby the LVD, including amplification effects of the dam, for models with the shear wave quality factor Qs(f) parameterized as $0.075V_S$ ($f < 1$Hz) and $0.075V_S f^{0.4}$ ($f > 1$Hz)(V_S in m/s), and a dam core with Vs=450 m/s.

Introduction

Dams retaining artificial water reservoirs are common and essential for irrigation and hydroelectric energy production in many parts of California. Ground shaking caused by earthquakes is usually the main hazard that must be considered in the safety evaluation of existing or projected dams (e.g., Wieland, 2014). No major concrete dam has failed as a result of ground motion from an earthquake (FEMA, 2005), and many arch dams have withstood significant shaking without physical evidence of damage. Embankment dams, usually built from compacted soils and rocks, have also responded satisfactorily to earthquake shaking in many cases, but have shown to be less resilient than concrete dams. During the 2011 M 9 Tohoku (Japan) earthquake, a drop in crest elevation led to overtopping and failure of the 18.5 m high Fujinuma earthdam (completed in 1949), and the uncontrolled discharge from the dam resulted in 8 fatalities. The 2008 M 8 Wenchuan (China) earthquake damaged more than 1,800 dams and reservoirs (e.g., Wieland and Chen, 2009), including the 156 m high Zipingpu concrete face rockfill (CFR) dam, where a maximum crest settlement of up to 1 m was recorded (e.g., Zou et al., 2013). During the 1971 M 6.6 San Fernando (CA) earthquake both the upper and lower Van Norman dams were severely damaged, and the lower dam was close to breaching (e.g., FEMA, 2005), prompting the evacuation of 80,000 people. Both dams were of the CFR type and constructed in the 1920s using the hydraulic fill method, which contributed to their vulnerability.

Overtopping of the lower dam, which would have led to a much greater disaster, was only averted because the water level at the time of the earthquake had been kept below the design elevation following an inspection a few years earlier. These examples underline the importanceof careful earthquake safety assessment in the construction and maintenance of dams.

This project focuses on the seismic response of the Long Valley Dam (LVD), a 55-meter high embankment dam located 35 km northwest of Bishop (CA), just east of the Sierra Nevada (see Figure 1, left). The dam consists mostly of an extensive rolled earthfill core (Lai and Seed, 1985) and was completed in 1941 to create Lake Crowley, which acts as a water reservoir for the city of Los Angeles. The dam has an array of accelerometers located on the dam crest, downstream wall, abutment and downstream bedrock (see Figure 1, right). While the long-term goal is to perform nonlinear analysis of the dam using strong motion recordings on the LVD array, our initial efforts presented here focus on the linear response. The array recorded, among others, ground motions from the 1986 M6.2 Chalfant Valley earthquake, as well as a 2015 M3.7 earthquake, providing excellent data to model the response of the LVD.

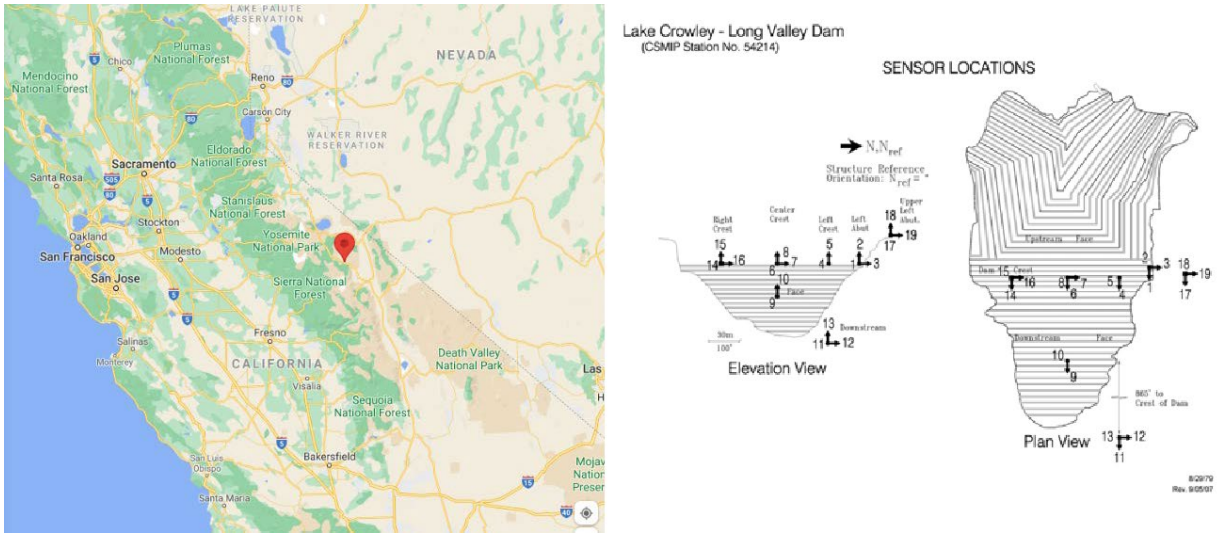

Figure 1. (left) Location of the LVD, and (right) sensor array deployed on the LVD.

We constructed a 3D Earth model including topography and the LVD, and validated the model against observed ground motions. Our reference model is extracted from the Southern California Earthquake Center (SCEC) Community Velocity Model (CVM) version 4.26-M01 (Small et al., 2017). We define frequency-dependent anelastic attenuation using the relation $Q_s=0.075V_s$ (f<1 Hz) and $Q_s=0.075V_s f^{0.4}$ (V_s in m/s), and $Q_p=2Q_s$, based on a suite of trial-and-error simulations, and in agreement with recent results for the Los Angeles area (Hu et al., 2021a). We included a shallow geotechnical layer (GTL), constrained by Vs30 values from the Wills et al. (2015) map, where the velocities from the surface are tapered to the background model at 700 m depth (Hu et al., 2021b), providing the best fit to data. Densities are derived using the empirical formulas by Brocher (2005). We model the dam with homogeneous material of V_s=450 m/s, V_p=1,000 m/s and ρ=2,110 m/s (see Figure 2). This model of the dam material is

somewhat stiffer than that used by Griffith and Prevost (1988), but generates the best fit to the data out of a series of models tested. The simulations use the scalable AWP-ODC finite difference code (Cui et al., 2013) with support for surface topography using the vacuum formulation.

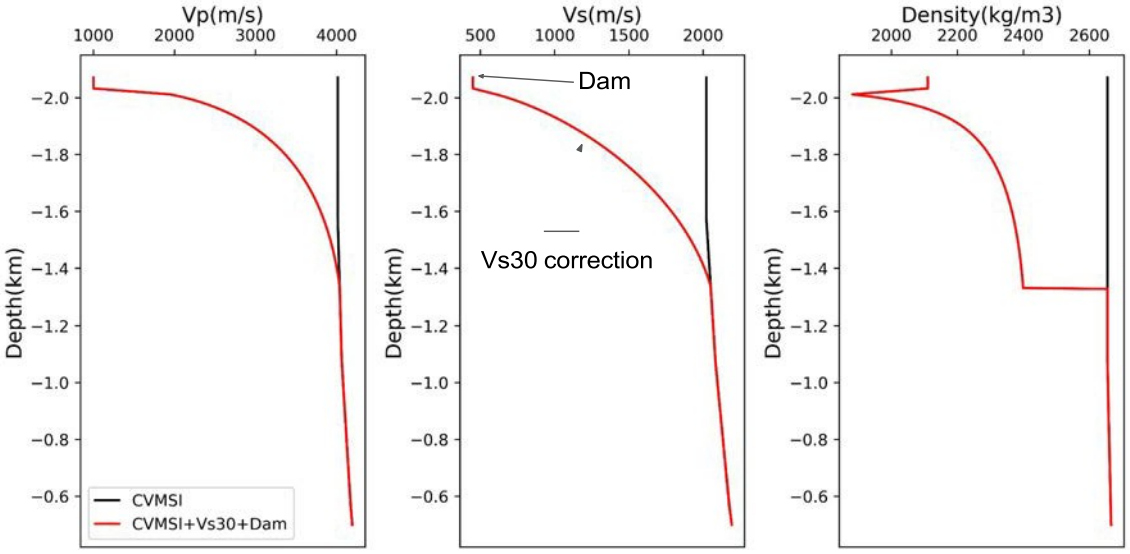

Figure 2. Velocity and density profiles (red lines) below the through and below the LVD, after applying the GTL to a depth of 700 m. Black lines depict the values in the CVM 4.26 before theGTL is applied.

Modeling of the 2015 M3.7 Earthquake

Figure 3 shows the model domain used for the simulations of the 2015 M3.7 earthquake (see Table 1 for source parameters), and Figure 4 shows the surface distribution of Vs.

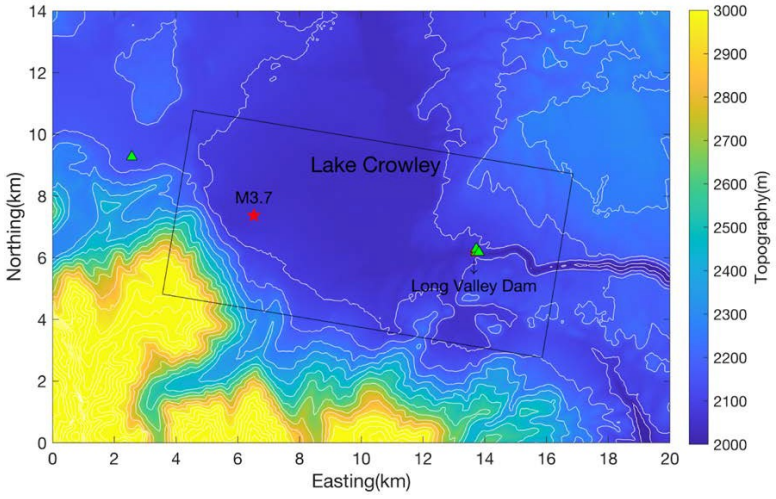

Figure 3. Model domain (black rectangle) for the simulation of the 2015 M3.7 earthquake.

Table 1

12.5 km x 6 km x 8.5 km domain
3564 x 1728 x 2432 grid points
dh=3.5m
$Q_s = 0.1 V_s f_s^{0.6}$
USGS 1m resolution DEMEvent information
Time: 2015/8/22 13:34:48 UTC
Epicenter: Lat: 37.598°N Lon: 118.788°WDepth: 4.8 km
Mw 3.71

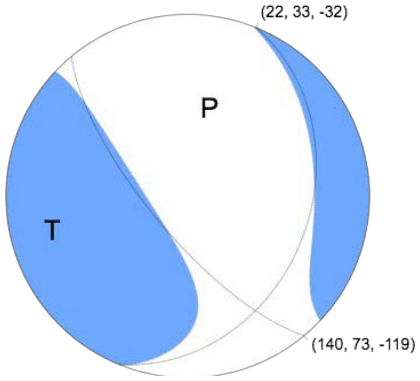

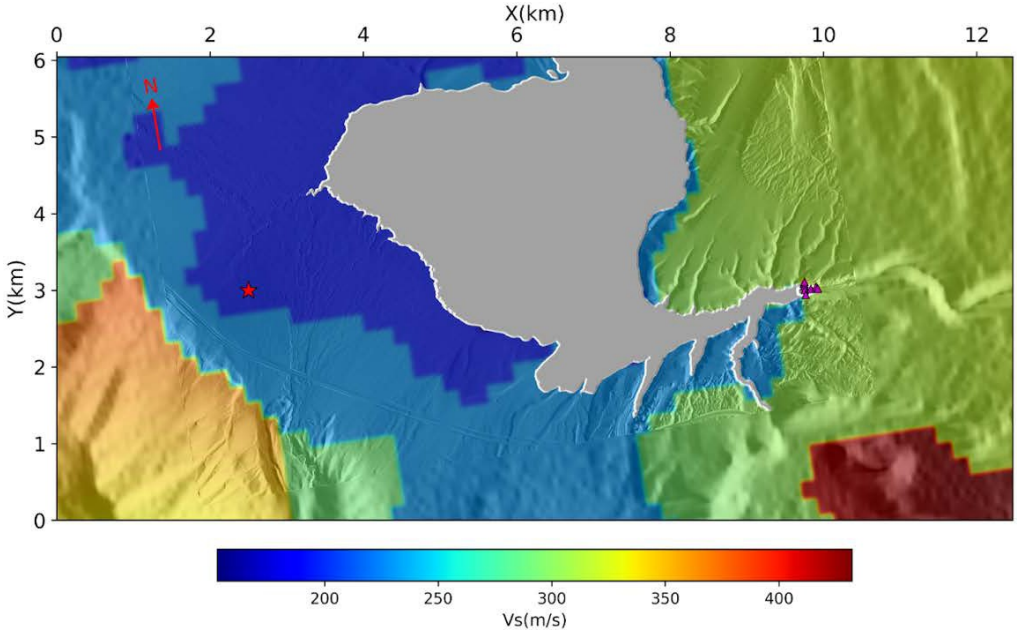

Figure 4. Surface V_S in the model domain (black rectangle in Figure 2) for the M 3.7 event, modified by the Vs30 map from Wills et al. (2015). The star depicts the epicenter, and the LVD is located near (X=10, Y=3 km), where the triangles depict sensor locations. The gray area is Lake Crowley.

Figures 5-10 show comparisons of 0.1-7.5 Hz synthetics and data at selected channels on and near the dam, in the time and FAS domains. In general, we obtain satisfactory fit between data and synthetics in both amplitude and duration. Figure 11 compares PGA for synthetics and data in the LVD array. The fit is acceptable, but the synthetics slightly overpredict the recorded PGAs on the dam crest for the east component. Figure 12 shows a comparison between downstream and center crest sensor records and synthetics. The comparison shows that the synthetics reproduce the amplification due to the dam, both in the time and FAS domains.

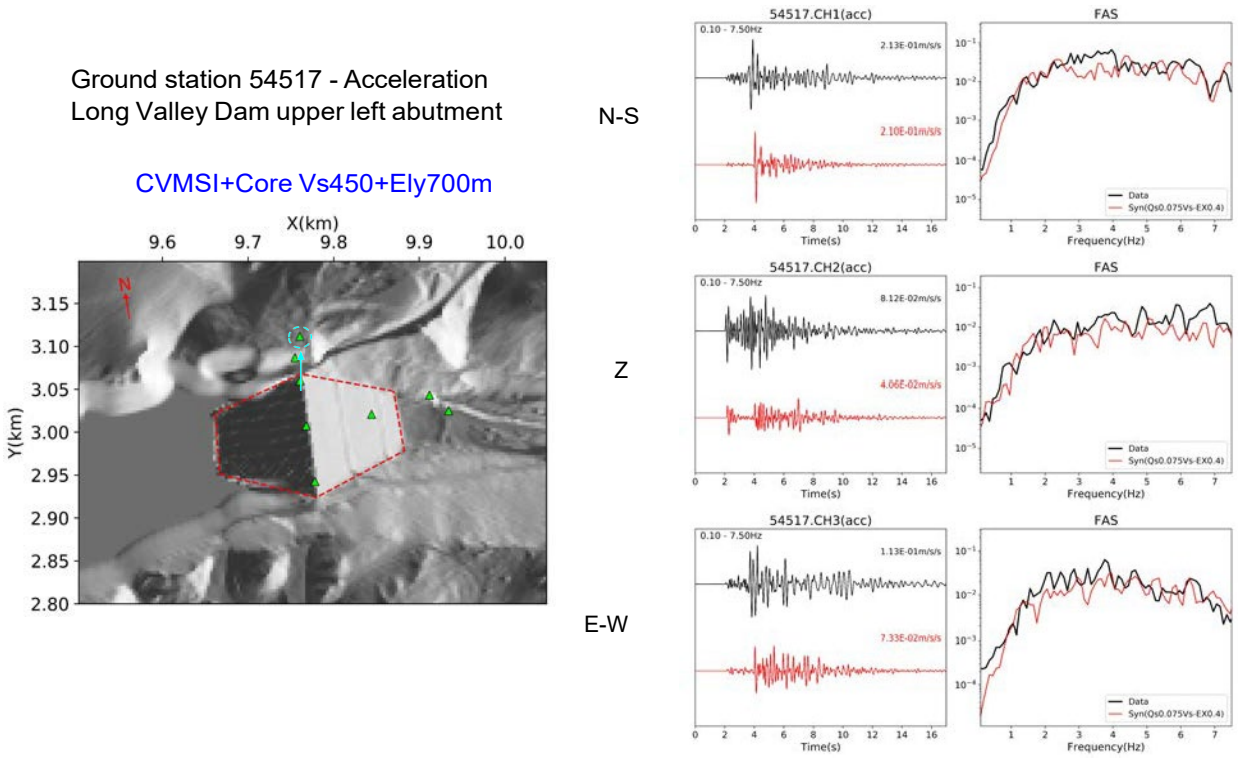

Figure 5. (left) Map showing locations of sensors at the LVD, and (right) comparison of data(black traces) and synthetics (red traces) in the time and FAS domains for the 2015 M3.7 earthquake, for the left abutment station (circled in map on the left).

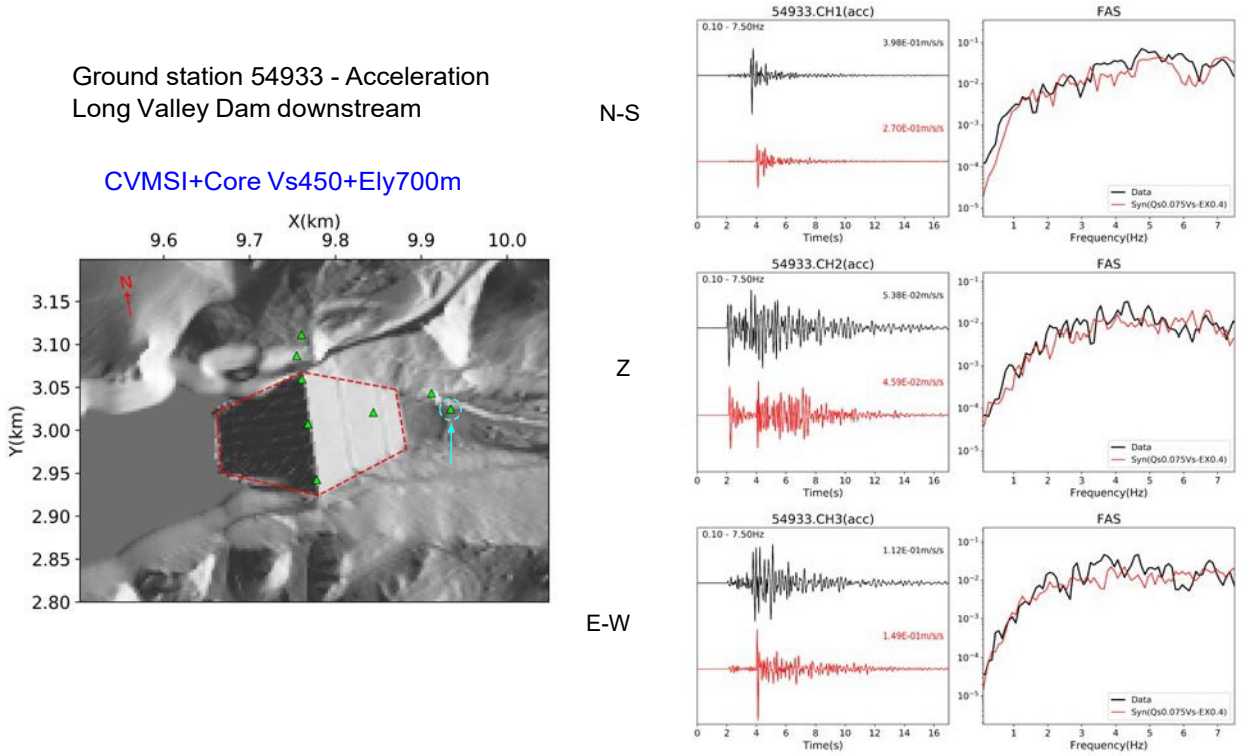

Figure 6. Same as Fig. 5, but for LVD downstream.

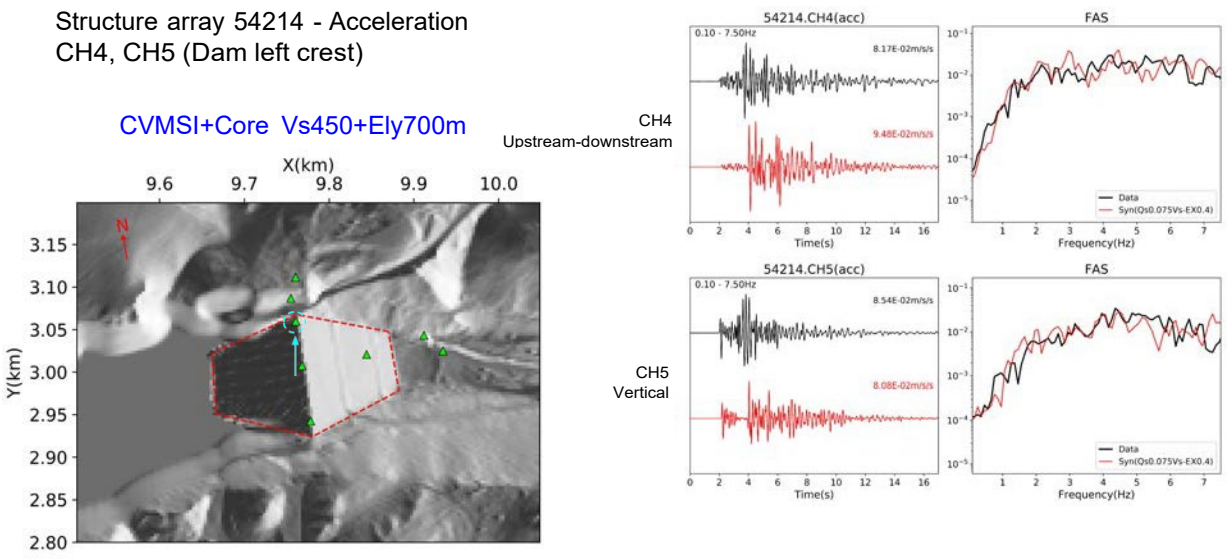

Figure 7. Same as Fig. 5, but for LVD left crest.

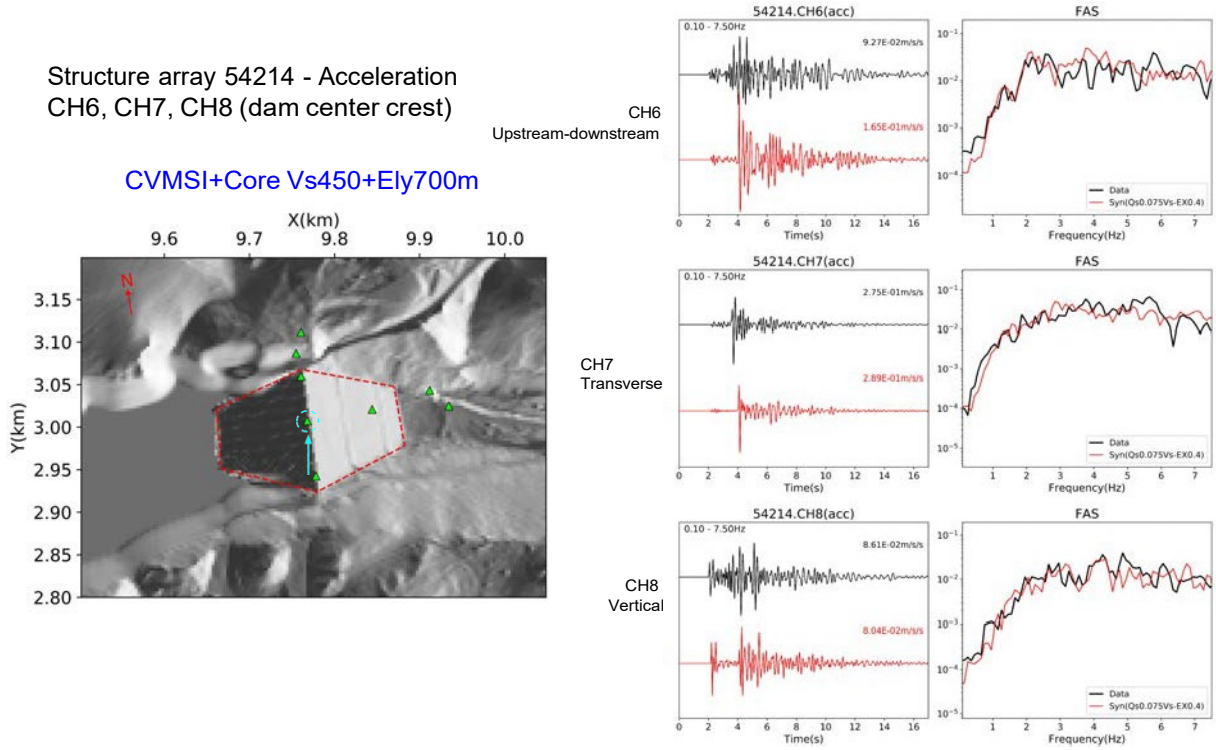

Figure 8. Same as Fig. 5, but for LVD center crest.

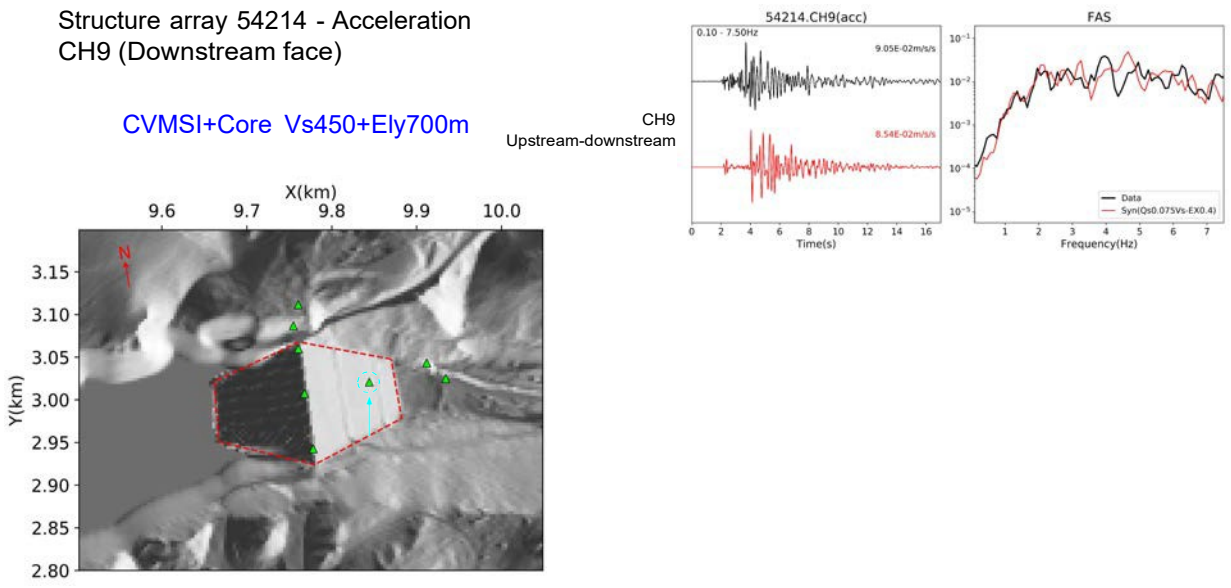

Figure 9. Same as Fig. 5, but for LVD downstream face.

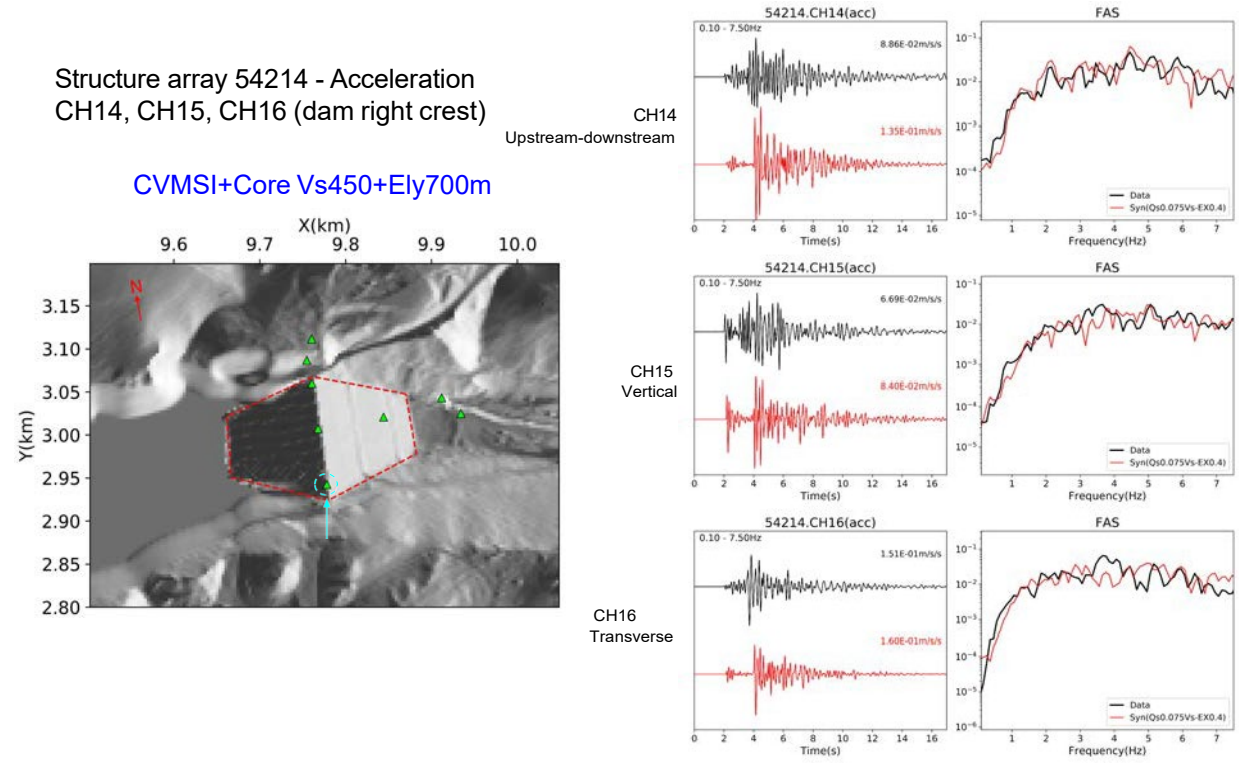

Figure 10. Same as Fig. 5, but for LVD right crest.

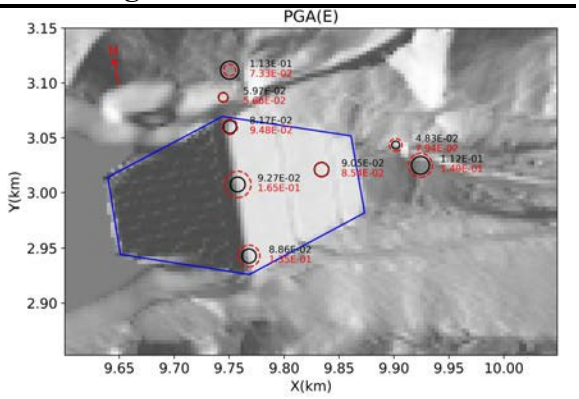

Figure 11. Comparison of east (E), vertical (Z), and north (N) component PGA for data (black circles) and synthetics (red circles) for the M3.7event. Circle radii are proportional to PGA (listed next to the circles, in m/s^2, color coded).

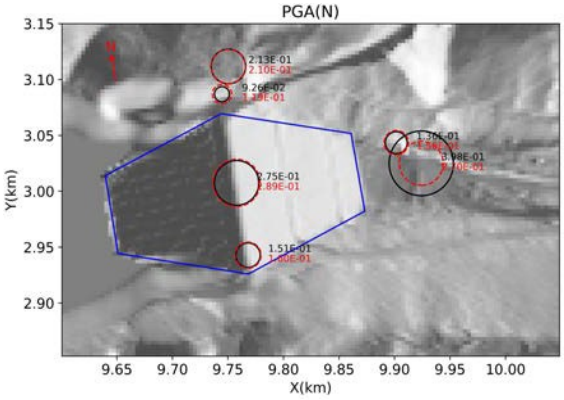

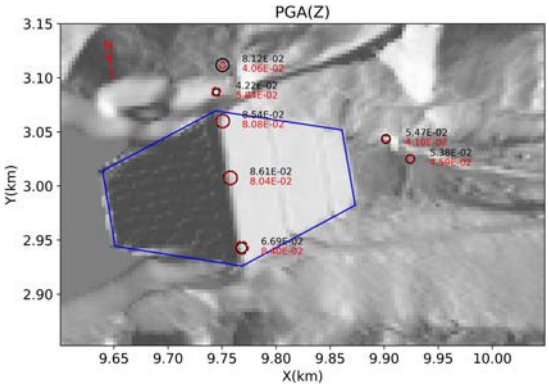

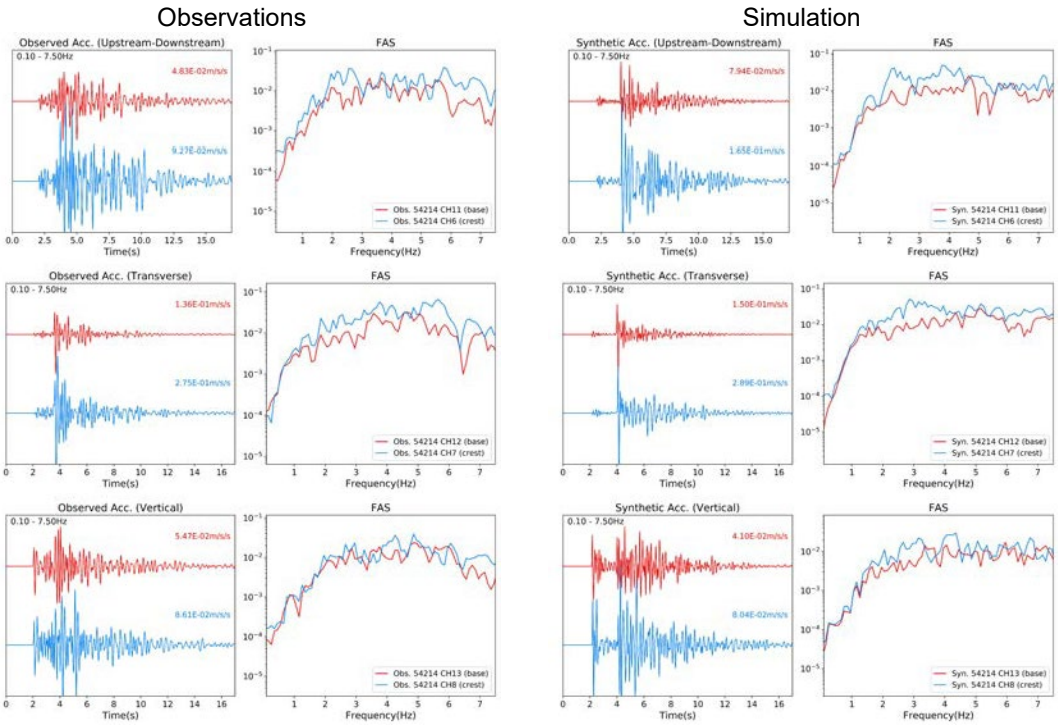

Figure 12. Comparison of base (channel 11) to crest (channel 6) amplification of accelerations, for (left)observations and (right) synthetics, for the M3.7 earthquake.

Modeling of the July 21 1986 Chalfant Valley, CA, Earthquake

The California-Nevada border region near Bishop, CA, was struck by a M_W6.2 earthquake on July 21, 1986. 24 hours before the mainshock, on July 20, a M5.9 foreshock occurred, and the largest aftershock (M5.8) hit on July 31. The sequence was recorded by several stations within 20 km of the source by stations deployed by the University of Nevada at Reno, with many more temporary stations added after the mainshock hit. Two people were injured, and property damage was estimated at $2.7 million (USGS, 1989).

We generated a source description using the kinematic rupture generator by Graves and Pitarka (2016), which requires information on hypocentral location, fault dimensions, and focal mechanism. To estimate these parameters, Cockerham and Corbett (1987) relocated the hypocentral locations of the Chalfant Valley earthquake sequence including the mainshock and aftershocks following the larger events. The aftershocks occurred below a depth of 3 km, with the hypocenter of the mainshock located at a depth of around 11 km. Seismic observations from local, regional and teleseismic data (Cockerham & Corbett, 1987; Pacheco & Nábělek, 1988; Smith & Priestley, 2000) suggest a fault plane striking 139º-155º and 55º-60º dipping to southwest with predominantly right-lateral slip. The coseismic dislocation model from geodetic data by Savage & Gross (1995) also suggests a right-lateral strike-slip faulting mechanism. The length and width of the fault plane for a M_W6.2 event estimated using the empirical relationship by Leonard (2010) agree reasonably well with the spatial extent of the aftershock distribution. Based on these findings, we use a length and width of the fault plane of 12 km and 10 km, respectively, with the top of the fault at a depth of 4 km. The focal mechanism is strike/dip/rake=150º/55º/180º. Figure 13 shows the relative location of the designated fault plane and the LVD. This source description leads to updip-bilateral rupture propagation, in agreement with the interpretation of Cockerham and Corbett (1987).

The simulation domain was rotated by 14.34º clockwise to save computational memory and wall clock time, and has a size of 39 km (L) x 22 km (W) x 15 km (H), as shown in Figure 13, left. The model covers up to 4,000 m above sea level to accommodate the highest topography within the domain. In order to incorporate the high-resolution geometry of the LVD into the mesh we use the 1-meter resolution digital elevation model (DEM) from USGS for the LVD and the surrounding area. At locations where the queried grid location is out of the range of the 1-meter resolution model, we used the elevations from the 1-arc-second resolution DEM from USGS which provides better spatial coverage. The slip distribution and rupture times are shown in Figure 13, right. Figure 14 shows the surface Vs in the model domain, after the application of the GTL.

Figures 15-18 shows comparison of acceleration time histories for synthetics and data at select stations on and nearby the LVD for the Chalfant Valley earthquake. In general, the synthetics provide a reasonable fit to the data in both time and Fourier domains, and the simulations reproduce the observed amplification of the dam structure.

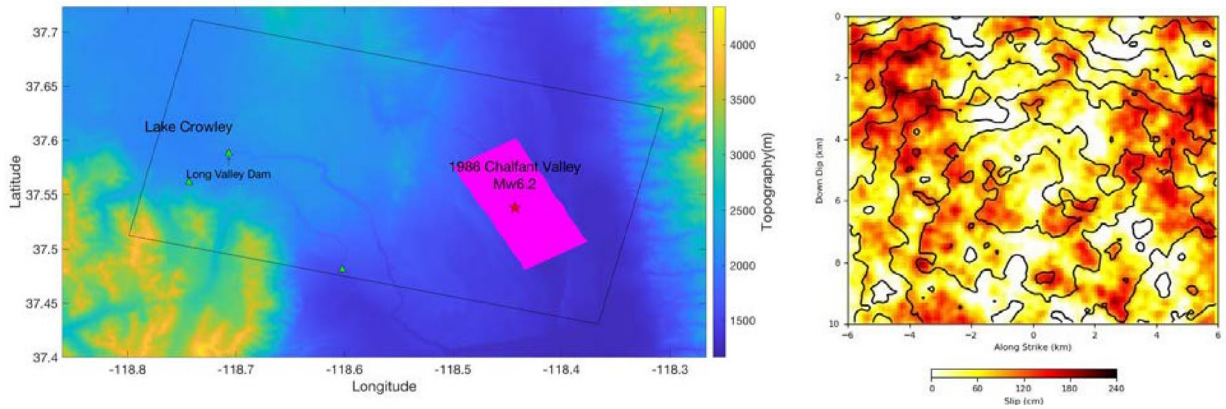

Figure 13. (left) Location map for the 1986 Chalfant earthquake relative to the LVD. The black box depicts the simulation domain for the earthquake. The purple area shows the surface projection of our finite fault source realization for the event, and the red star shows the epicentral location. The green triangles are station locations. (right) Slip distribution of the rupture model generated by the Graves and Pitarka (2016) kinematic rupture generator.

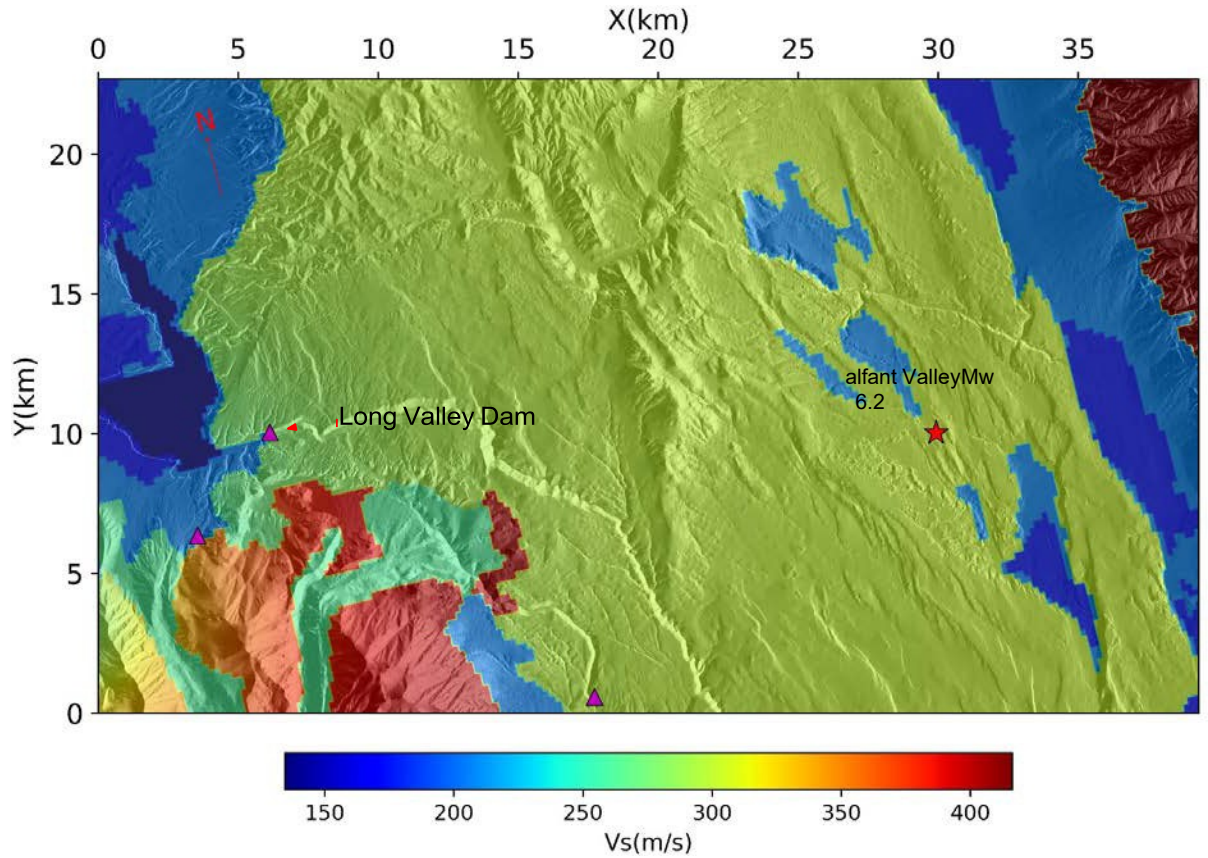

Figure 14. Surface V_S in the model domain (black rectangle in Figure 13, left) for the Chalfant Valley event, modified by the Vs30 map from Wills et al. (2015). The star depicts the epicenter, and the triangle depicts the LVD.

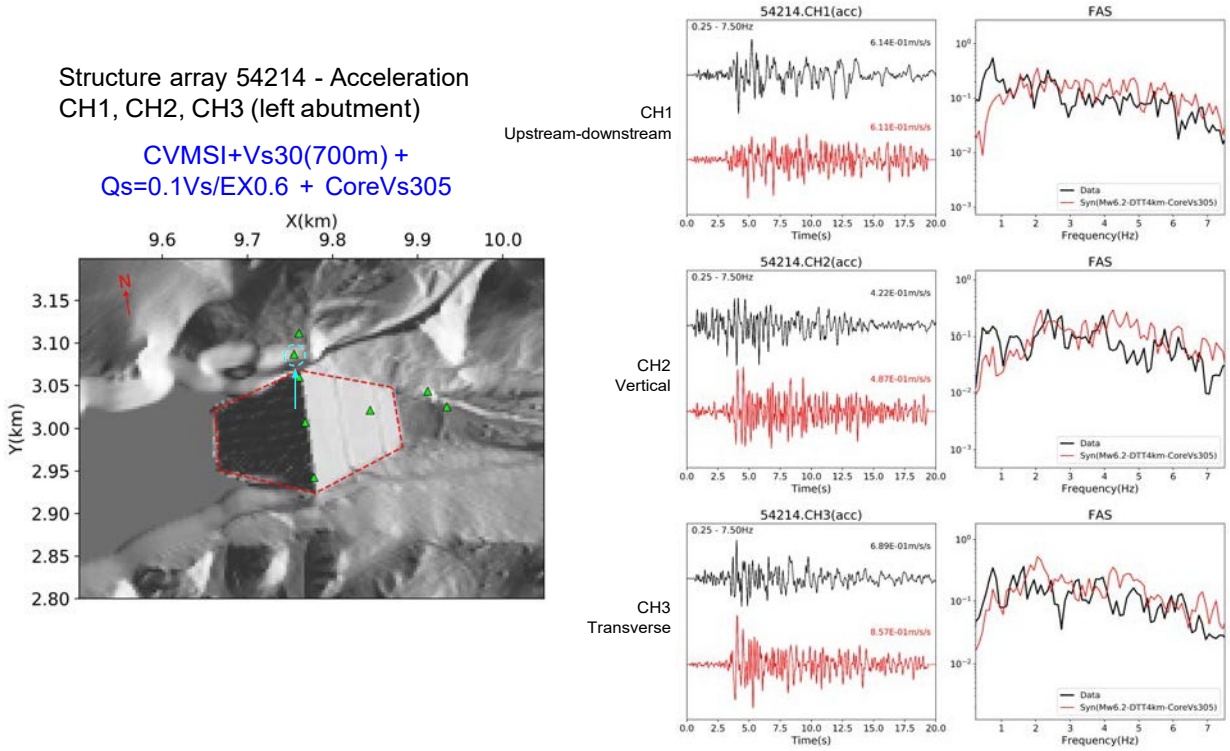

Figure 15. (left) Map showing locations of sensors at the LVD, and (right) comparison of data (black traces) and synthetics (red traces) in the time and FAS domains for the 1986 Chalfant Valley, CA, earthquake, for the left abutment station (circled in map on the left).

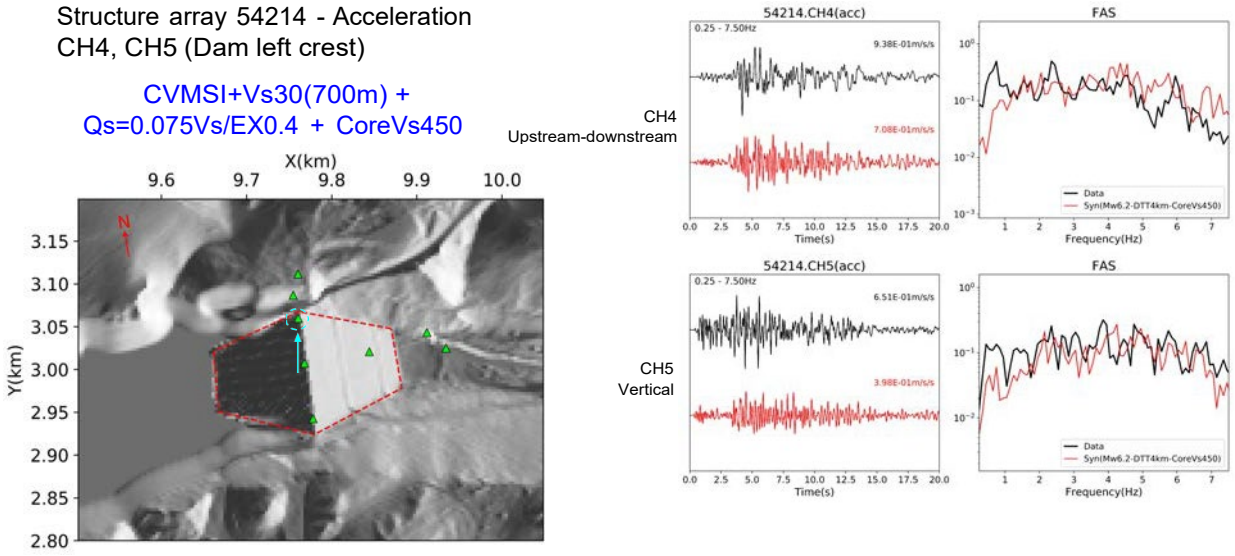

Figure 16. Same as Fig. 15, but for LVD left crest.

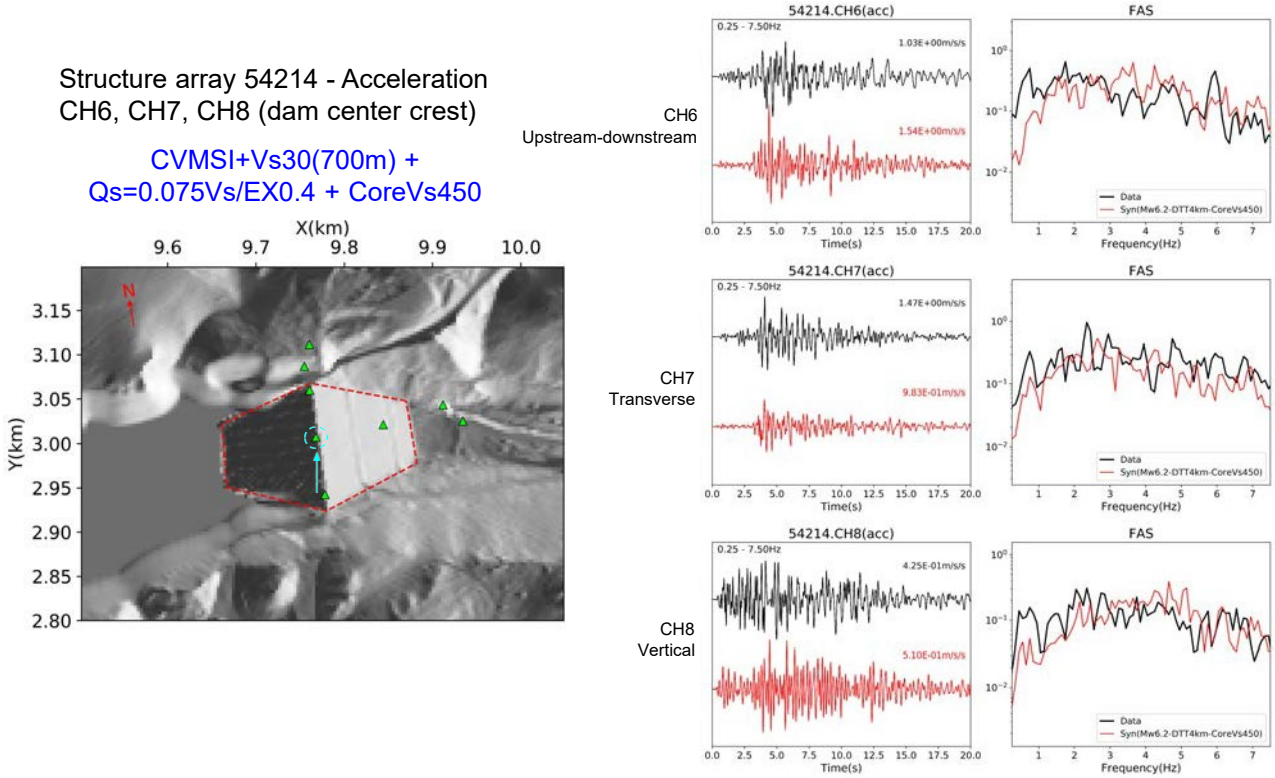

Figure 17. Same as Fig. 15, but for LVD center crest.

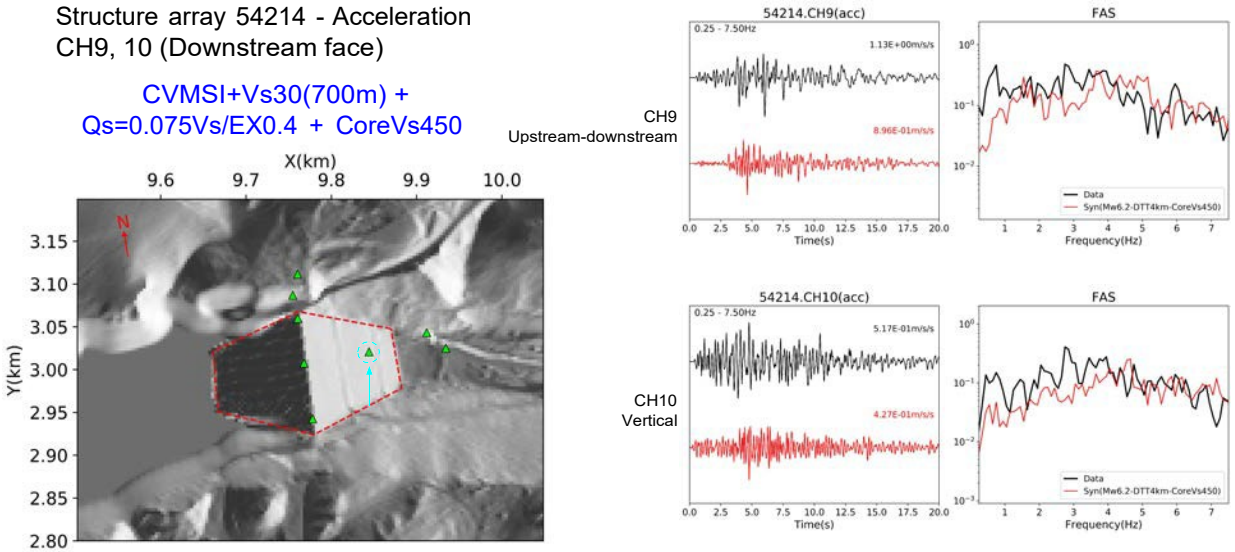

Figure 18. Same as Fig. 15 but for LVD downstream face.

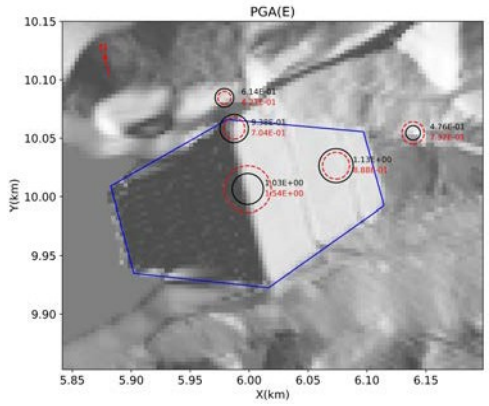

Figure 19. Comparison of east (E), vertical (Z),and north (N) component PGA for data (black circles) and synthetics (red circles) for the Chalfant Valley earthquake. Circle radii are proportional to PGA (listed next to the circles, in m/s^2, color coded).

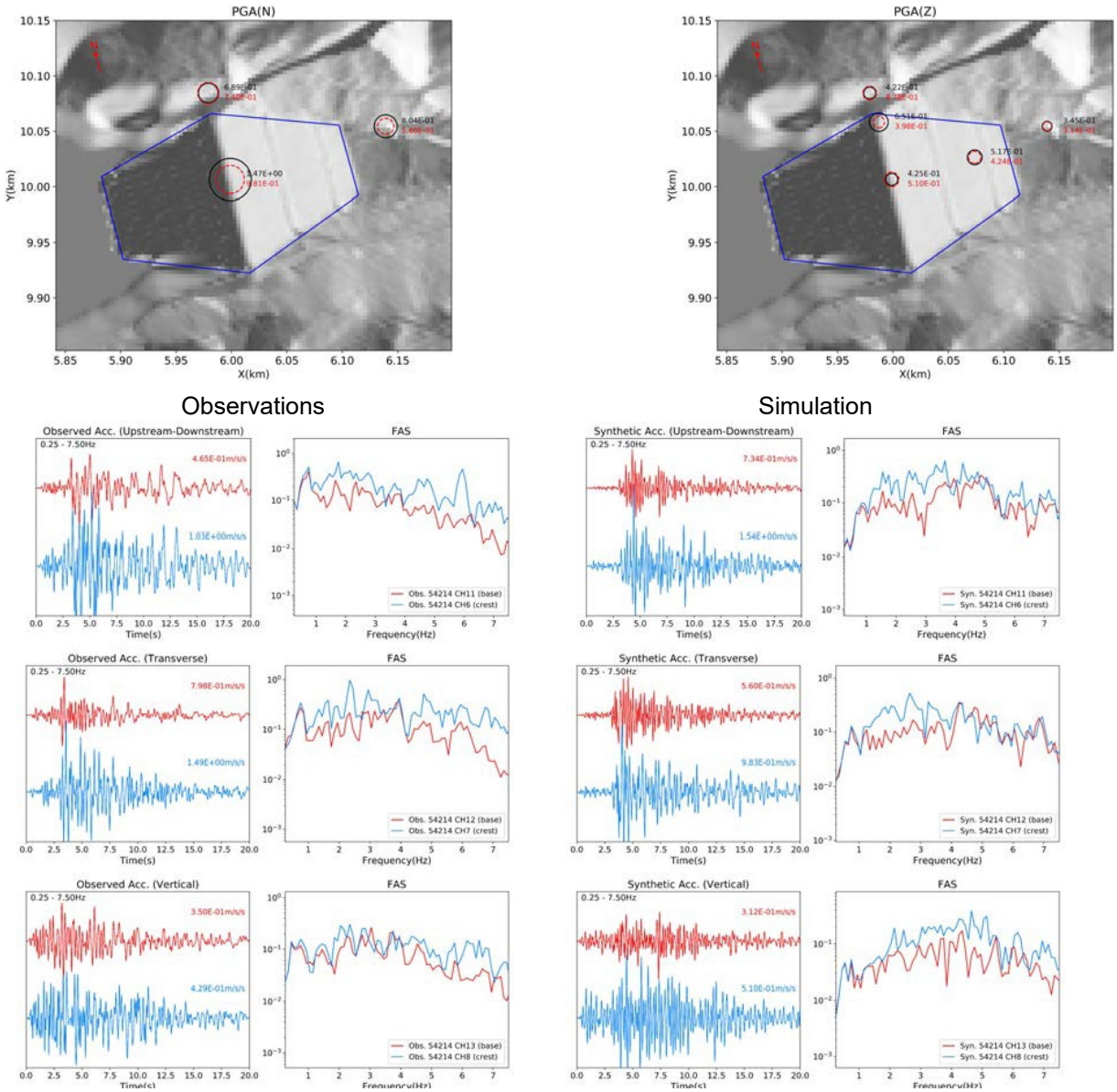

Figure 20. Comparison of base (channel 11) to crest (channel 6) amplification of accelerations, for (left)observations and (right) synthetics, for the Chalfant Valley earthquake.

Future Work: Nonlinear Soil Effects

The 1986 Chalfant Valley earthquake generated PGAs up to 0.21g at the LVD, at or above the threshold of 0.15-0.2g for the onset of nonlinear soil effects found in several published studies (e.g., Ren et al., 2017; Regnier et al., 2011; Huang et al., 2000). Thus, the records from the event may be used to validate the nonlinear response of the LVD. For this purpose, we plan to use a fully hysteretic Iwan-type, multi-yield surface approach (Iwan, 1967) implemented in AWP (Roten et al., 2019), to assess any nonlinear response and calibrate the reference strain.

The Hilton Creek Fault (HCF) is a significant range-bounding normal fault at the eastern side of the Sierra Nevada. Because it passes just 8 km west of the LVD, it has been identified asa possible source for the Maximum Credible Earthquake (MCE) that could significantly affect the stability of the dam (Lai and Seed, 1985). The scenario of a M 6.8 earthquake on the HCF was also considered in a recent study on earthquake hazards for the Long Valley Caldera-Mono Lake Area (Chen et al., 2014). It was estimated that such an event would result in a PGA of 0.4–0.5g at the site of the LVD (Chen et al., 2014). We plan to perform realistic simulations of rupture, wave propagation and dam response during a M 6.8 scenario on the HCF. We will analyze peak ground velocities on the dam slopes and crest, as well as permanent deformations throughout the dam structure, to assess the performance of the structure during such an event.

Disclaimer

The contents of this report were developed under Contract No. 1020-006 from the CaliforniaDepartment of Conservation, California Geological Survey, Strong Motion Instrumentation Program. However, these contents do not necessarily represent the policy of that agency or endorsement by the State Government.

Acknowledgements

This project is supported by the California Department of Conservation, California GeologicalSurvey, Strong Motion Instrumentation Program, Contract 1020-006. Simulations and post- processing were carried out on the OLCF (Oak Ridge Leadership Computational Facility) supercomputers SUMMIT and the cluster Rhea under an INCITE research allocation.

References

Bonilla, L. F., R. J. Archuleta, and D. Lavallée (2005). Hysteretic and dilatant behavior of cohesionless soils and their effects on nonlinear site response: Field data observations and modeling, Bull. Seismol. Soc. Am. 95, no. 6, 2373–2395.

Brocher, T.M. (2005) Empirical Relations between Elastic Wavespeeds and Density in the Earth's Crust. *Bulletin of the Seismological Society of America*, **95**, 2081–2092. doi:10.1785/0120050077.

Chen, Rui, Branum, David M, Wills, Chris J, and Hill, David P. (2014). Scenario earthquake hazards for the Long Valley Caldera-Mono Lake area, east-central California. Tech. rept. US

Geological Survey.

Cockerham, R. S., & Corbett, E. J. (1987). The July 1986 Chalfant Valley, California, earthquake sequence: preliminary results. *Bulletin of the Seismological Society of America, 77*(1), 280-289.

Cui, Y., Poyraz, E., Olsen, K. B., Zhou, J., Withers, K., Callaghan, S., Larkin, J., Guest, C., Choi, D, Chourasia, A., et al. 2013. Physics-based seismic hazard analysis on petascale heterogeneous supercomputers. Page 70 of: Proceedings of SC13: International Conference for High Performance Computing, Networking, Storage and Analysis. ACM.

Ely, G., Small, P., Jordan, T.H., Maechling, P.J. & Wang, F. (2010) A Vs30-derived Near-surface Seismic Velocity Model. No. S51A-1907, p. 1, Presented at the AGU, San Francisco, California.

FEMA. 2005. Earthquake Analysis and Design of Dams. Federal Guidelines for Dam Safety, FEMA-65. Washington, D.C. https://www.fema.gov/media-library/assets/documents/ 2482.

Graves, R., & Pitarka, A. (2016). Kinematic Ground-Motion Simulations on Rough Faults Including Effects of 3D Stochastic Velocity Perturbations. *Bulletin of the Seismological Society of America, 106*(5), 2136-2153. https://doi.org/10.1785/0120160088

Griffiths, D.V., and Prevost, J. H. 1988. Two-and three-dimensional dynamic finite element analyses of the Long Valley Dam. Geotechnique, 38(3), 367–388.

Hu, Z., K.B. Olsen, and S.M. Day (2021a). 0-5 Hz Deterministic 3D Ground Motion Simulations for the 2014 La Habra, CA, Earthquake, Geophysical Journal International, submitted October 2021.

Hu, Z., K.B. Olsen, and S.M. Day (2021b). Calibration of the Near-surface Seismic Structure in the SCEC Community Velocity Model Version 4, Geophysical Journal International, submitted October 2021.

Huang, H.C., C.S. Shieh, and H.C. Chiu (2000). Linear and nonlinear behaviors on a soil site using Loftung downhole array in Taiwan, Procs. 12WCEE.

Iwan, W. (1967). On a class of models for the yielding behavior of continuous and composite systems. J. Appl. Mech, 34(4):612–617.

Lai, S.S., and Seed, H.B. (1985). Dynamic Response of Long Valley dam in the Mammoth Lake Earthquake Series of May 25–27 1980. Tech. rept. UCB/EERC-85/12. Earthquake Engineering Research Center.

Leonard, M. (2010). Earthquake Fault Scaling: Self-Consistent Relating of Rupture Length, Width, Average Displacement, and Moment Release. *Bulletin of the Seismological Society of America, 100*(5A), 1971-1988. https://doi.org/10.1785/0120090189.

O'Reilly, O., T.-Y. Yeh, K.B. Olsen, Z. Hu, A. Breuer, D. Roten, and C. Goulet (2021). A high-order finite difference method on staggered curvilinear grids for seismic wave propagation applications with topography, Bull. Seis. Soc. Am., published online, Sept 8,2021.

Pacheco, J., & Nábělek, J. (1988). Source mechanisms of three moderate California earthquakes of July 1986. *Bulletin of the Seismological Society of America, 78*(6), 1907-1929.

Ren, Y., R. Wen, X. Yao, and K. Ji (2017). Five parameters for the evaluation of the soil nonlinearity during the Ms8.0 Wenchuan earthquake using the HVSR method, Earth, Planets and Space 69:116, DOI 10.1186/s40623-017-0702-7.

Regnier, J., L.F. Bonilla, E. Bertrand, and J.F. Semblat (2011). Empirical evidence of nonlinear response at several KIK-net stations, Procs. Of Effects of Surface Geology on Seismic Motion, August 23-26, 2011, University of California Santa Barbara.

Roten, D., K. B. Olsen, J. C. Pechmann (2012). 3D Simulations of M 7 Earthquakes on the Wasatch Fault, Utah, Part II: Broadband (0-10Hz) Ground Motions and Nonlinear SoilBehavior (2012). Bull. Seis. Soc. Am. 102, 2008-2030.

Roten, D., K.B. Olsen, and S.M. Day (2019). 3D simulation of large San Andreas scenario earthquakes using a multi-surface plasticity model, Seism. Res. Lett., 90, 2B, 943.

Savage, J. C., & Gross, W. K. (1995). Revised dislocation model of the 1986 Chalfant Valley earthquake, eastern California. *Bulletin of the Seismological Society of America, 85*(2),629-631.

Small, P., Gill, D., Maechling, P. J., Taborda, R., Callaghan, S., Jordan, T. H., et al. (2017). The SCEC Unified Community Velocity Model Software Framework. *Seismological Research Letters, 88*(6), 1539-1552. https://doi.org/10.1785/0220170082

Smith, K. D., & Priestley, K. F. (2000). Faulting in the 1986 Chalfant, California, Sequence: Local Tectonics and Earthquake Source Parameters. *Bulletin of the Seismological Societyof America, 90*(4), 813-831. https://doi.org/10.1785/0119990129

USGS (1989). The intensity of the July 21, 1986, Chalfant Valley, California, earthquake, USGS Open-File Report 89-135, L. Brewer, 25 p.

Wieland, M., and Chen, H. (2009). Lessons learnt from the Wenchuan earthquake. International Water Power & Dam Construction, 36–40.

Wieland, M. (2014). Seismic hazard and seismic design and safety aspects of large dam projects. Pages 627–650 of: Perspectives on European Earthquake Engineering and Seismology.Springer.

Wills, C. J., Gutierrez, C. I., Perez, F. G., & Branum, D. M. (2015). A Next Generation VS30 Map for California Based on Geology and Topography. *Bulletin of the Seismological Society of America, 105*(6), 3083-3091. https://doi.org/10.1785/0120150105.

Zou, D., Xu, B., Kong, X., Liu, H., and Zhou, Y. (2013). Numerical simulation of the seismic response of the Zipingpu concrete face rockfill dam during the Wenchuan earthquake based on a generalized plasticity model. Computers and Geotechnics, 49, 111–122.

ARTIFICIAL INTELLIGENCE-ENABLED STRUCTURAL HEALTH MONITORING

Yuqing Gao* and Khalid M. Mosalam†

Pacific Earthquake Engineering Research (PEER) Center
Department of Civil & Environmental Engineering, University of California, Berkeley

Extended Abstract

In this data explosion epoch, artificial intelligence (AI)-enabled structural health monitoring (SHM) using the state-of-the-art machine learning (ML) and deep learning (DL) technologies has become of great interest in civil engineering. Based on data type, it can be further classified into two major directions, namely *vision-based* [6] and *vibration-based* [1] SHM.

In vision-based SHM, two critical issues need to be addressed: (1) the lack of uniform automated damage detection principles based on domain knowledge, and (2) the lack of benchmark datasets with well-labeled large amounts of data. Therefore, we developed the automated and hierarchical framework called PEER Hub Image-Net (PHI-Net or simply φ-Net) [7]. The framework consists of eight basic benchmark detection tasks based on current domain knowledge and past reconnaissance experience. These tasks are: (1) scene level, (2) damage state, (3) concrete cover spalling condition (material loss), (4) material type, (5) collapse mode, (6) component type, (7) damage level, and (8) damage type. According to the φ-Net framework, a large number of structural images was collected, preprocessed, and labeled to form the φ-Net dataset, an open-source online large-scale multi attribute image dataset, which currently contains 36,413 images with multiple labels. However, compared to the general computer vision benchmark dataset, ImageNet containing 15 million labeled images, the size of φ-Net is still not large enough. Therefore, transfer learning (TL) was adopted to better utilize the features from source domain of general ImageNet to the target structural image datasets [5, 6, 17]. Besides, generative adversarial networks (GANs) for structural image data augmentation [4] and also Balanced Semi-Supervised GAN (BSS-GAN) [10] have been developed to address the lack of labeled data and imbalanced class issues.

Through φ-Net benchmarking experiments, promising results were achieved and reported, which provide the reference for future DL applications. The well-trained models in these experiments are named Structural ImageNet Models (SIMs) and they serve as benchmarks for future development of classification algorithms. Moreover, the direct application of these SIMs was further performed, namely image-based post-disaster assessment of the 1999 Chi-Chi earthquake, Taiwan, which revealed the high potential and contribution of the φ-Net in vision-based SHM [7]. From a structural engineering point of view, a recent important development pertains to a systematic and human-in-the-loop deep learning model interpretation & diagnoses framework, namely Structural Image Guided Map Analysis Box (SIGMA-Box), which gives better understanding of how deep convolutional neural network (DCNN) models work in vision-based SHM [8]. Moreover, adopting the SIGMA-Box increases the level

*Post-Doctoral Researcher, gaoyuqing@berkeley.edu.
†Corresponding author, Taisei Professor of Civil Engineering & PEER Director, mosalam@berkeley.edu.

of confidence of engineers in these DCNN models to further improve their performance, and effectively apply them to practical structural engineering problems.

Attention has been given to the applications of DL in practical bridge health monitoring (BHM) projects. In such AI-enabled BHM, crack identification and width measurement are two of the important metrics for evaluating the functionality of bridges. However, some problems still exist in extending previously developed ML/DL methods to practical applications, such as data annotation difficulty, limited model generalization ability, and inaccuracy of the DL identification of the actual crack width measurement. An application-oriented multi stage crack recognition framework is recently proposed and called Convolutional Active Learning Identification-Segmentation-Measurement (CAL-ISM) [18]. It includes four kernel steps: (1) pre-training of the benchmark classification model, (2) re-training of the semi-supervised active learning model, (3) pixel-level crack segmentation, and (4) crack width measurement. The performance of the CAL-ISM framework is validated from two practical applications: (i) test bridge column specimen, and (ii) field BHM project. The obtained results from these applications demonstrated the effectiveness of CAL-ISM for BHM applications, which is recommended for more future BHM deployments.

In the direction of vibration-based SHM, vibration data especially acceleration plays the major role [2, 3, 12]. Since the turn of this century, time series (TS) modeling of vibration signals using a family of auto-regressive (AR) models was found to be effective in damage detection and has been used to capture damage features in structures [2, 3, 9] . However, there are some drawbacks limiting the use of AR series modeling in practice. The most notable is the requirement of stationary input, which is difficult to achieve in real SHM applications, where TS data (i.e., vibration signals) collected from sensors after earthquakes are usually non-stationary. Thus, elaborate data pre-processing (e.g., segmenting, de-trending, and de-nosing) and stationarity checks are inevitable before modeling. However, these methods lack a systematic pipeline and may not guarantee stationarity. Thus, we developed a systematic two-stage framework, namely Auto-Regressive Integrated Moving-Average Machine Learning (ARIMA-ML), to combine TS modeling techniques and ML approaches for detecting structural damage [9]. The first stage focuses on the TS modeling, and the second stage performs the recognition tasks. Specifically, ARIMA-ML consists of four main modules: (1) pre-processing, (2) model parameter determination, (3) feature extraction, and (4) classification. The performance of the framework was validated using data from full-scale shaking table tests of a three-story steel frame making use of the average segment accuracy and confusion matrix. The validation experimental results demonstrated the robustness and accurate performance of the ARIMA-ML in all tasks. In addition, the feature importance (*FI*) score was analyzed to examine the most important features for damage detection and pattern recognition, illustrating the need for higher order coefficients and validating the superiority of the proposed framework.

Even though the number of AI-enabled SHM studies and applications is rising in the past five years, very few of them bridge the gap between ML/DL results and the final decision making procedure. In one of our ongoing project for developing the “Bridge Rapid Assessment Center for Extreme Events (BRACE2)”, we developed a post-earthquake damage and functionality assessment framework and implemented it on Route 580/238 Separation in Hayward

and demonstrated it with four other bridges. The developed framework uses the data to provide a real-time estimate of the bridge damage that can be used to inform decisions concerning whether to close the bridge to traffic and where to expect damage. At the core of the framework is a Decision-Making Platform (DMP) that utilizes data streamed in real-time from accelerometers along with limit states (LS) from component models as key features, e.g., [14], to extract using ML, response from a global bridge model subjected to the recorded ground motion signals, and ML/DL rapid recognition results. This facilitates the decision-making about the damage condition, location & severity, refer to [15, 16] for an earlier development of this DMP as a framework for Human-Machine Collaboration (H-MC). The H-MC framework combines ML tool using *novelty detection* and human (domain) expertise using structure-specific analytical model for damage assessment of instrumented structures with only data from undamaged cases. It was successfully used to detect undamaged and damaged 15 real instrumented buildings in California [13]. Moreover, such DMP can be expanded to be in terms of a full probabilistic formulation of the multi attribute utility theory (MAUT) for holistic designs/decisions. This was conducted in [11] where uncertainties were modeled by random variables defined through a performance-based engineering (PBE) approach to take into account not only safety issues in the face of extreme events such as major earthquakes, but also environmental responsibility and energy consumption.

In summary, the developed advances and obtained promising results in AI-enabled SHM studies shed light on the high potential of these state-of-the-art methodologies in more practical structural engineering applications. In future pursuits, improved monitoring, learning, maintenance, and ultimately effective decision-making regarding the conditions, replacement or retrofit of the built environment can be reliably achieved.

Acknowledgements

This research received funding support from California Department of Transportation (Caltarns) for the “Bridge Rapid Assessment Center for Extreme Events (BRACE2)” project, Tsinghua-Berkeley Shenzhen Institute (TBSI), and the California Department of Conservation’s Strong Motion Instrumentation Program (CSMIP). Additional financial support was provided by the Taisei Chair of Civil Engineering, Univ. of California, Berkeley. Opinions and findings in this paper are those of the authors and do not necessarily reflect those of the sponsors.

References

[1] Yalin Arici and Khalid M. Mosalam. System identification of instrumented bridge systems. *Earthquake Eng. & Structural Dynamics*, 32(7):999–1020, 2003.

[2] Yalin Arici and Khalid M. Mosalam. Modal identification of bridge systems using state-space methods. *Structural Control & Health Monitoring*, 12(3-4):381–404, 2005.

[3] Yalin Arici and Khalid M. Mosalam. Statistical significance of modal parameters of bridge systems identified from strong motion data. *Earthquake Eng. & Structural Dynamics*, 34(10):1323–1341, 2005.

[4] Yuqing Gao, Boyuan Kong, and Khalid M. Mosalam. Deep leaf-bootstrapping genera-

tive adversarial network for structural image data augmentation. *Computer-Aided Civil & Infrastructure Eng.*, 34(9):755–773, 2019.

[5] Yuqing Gao, Bozhe Li, Khalid M. Mosalam, and Selim Günay. Deep residual network with transfer learning for image-based structural damage recognition. In *Eleventh US National Conference on Earthquake Eng., Integrating Science, Eng. & Policy*, 2018.

[6] Yuqing Gao and Khalid M. Mosalam. Deep transfer learning for image-based structural damage recognition. *Computer-Aided Civil & Infrastructure Eng.*, 33(9):748–768, 2018.

[7] Yuqing Gao and Khalid M. Mosalam. PEER Hub ImageNet: A large-scale multiattribute benchmark data set of structural images. *ASCE, Journal of Structural Eng.*, 146(10):04020198, 2020.

[8] Yuqing Gao and Khalid M. Mosalam. Deep learning visual interpretation on images of structural damage. *Journal of Building Eng.*, Submitted, 2021.

[9] Yuqing Gao, Khalid M Mosalam, Yueshi Chen, Wei Wang, and Yiyi Chen. Autoregressive integrated moving-average machine learning for damage identification of steel frames. *Applied Sciences*, 11(13):6084, 2021.

[10] Yuqing Gao, Pengyuan Zhai, and Khalid M. Mosalam. Balanced semi-supervised generative adversarial network for damage assessment from low-data imbalanced-class regime. *Computer-Aided Civil & Infrastructure Eng.*, 36(9):1094–1113, 2021.

[11] Khalid M. Mosalam, Umberto Alibrandi, Hyerin Lee, and Jaume Armengou. Performance-based engineering and multi criteria decision analysis for sustainable and resilient building design. *Structural Safety*, 74:1–13, 2018.

[12] Khalid M. Mosalam and Yalin Arici. Health monitoring of a bridge system using strong motion data. *Smart Structures & Systems*, 5(4):427–442, 2009.

[13] Khalid M. Mosalam, Sifat Muin, and Yuqing Gao. New directions in structural health monitoring. *NED University Journal of Research*, 2:77–112, 2019.

[14] Sifat Muin and Khalid M. Mosalam. Cumulative absolute velocity as a local damage indicator of instrumented structures. *Earthquake Spectra*, 33(2):641–664, 2017.

[15] Sifat Muin and Khalid M Mosalam. Human-machine collaboration framework for structural health monitoring and resiliency. *Eng. Structures*, 235:112084, 2021.

[16] Sifat Muin and Khalid M Mosalam. Structural health monitoring using machine learning and cumulative absolute velocity features. *Applied Sciences*, 11(12):5727, 2021.

[17] Zifeng Wang, Yuyang Zhang, Khalid M. Mosalam, Yuqing Gao, and Shao-Lun Huang. Deep semantic segmentation for visual understanding on construction sites. *Computer-Aided Civil & Infrastructure Eng.*, 36(11), 2021.

[18] Yue Zheng, Yuqing Gao, Shiyuan Lu, and Khalid M. Mosalam. Multi-stage semi-supervised active learning framework for crack identification, segmentation and measurement of bridges. *Computer-Aided Civil & Infrastructure Eng.*, Submitted, 2021.

SHAKEALERT® EARTHQUAKE WARNING: THE CHALLENGE OF TRANSFORMING GROUND MOTION INTO PROTECTIVE ACTIONS

Douglas Given[1)] and the West Coast ShakeAlert Project Team

[1)] U.S. Geological Survey, Pasadena, CA, USA. E-mail: doug@usgs.gov

Abstract

The USGS ShakeAlert® earthquake early warning (EEW) system is operational and providing public alerting in three West Coast states: California, Washington, and Oregon. Since 2006 the USGS has pursued a strategy of incrementally developing and rolling out EEW for increasingly larger areas and uses.As funding from federal and state budgets grew the system became more capable, detection methods were developed and improved, core network sensor stations were built or upgraded, and partners were enlisted to deliver alerts and implement protective actions. In the fall of 2018, the system became sufficiently functional to publicly declare it "open for business" in all three states for use by licensed partners to alert personnel in limited settings and take automated machine-to-machine actions. State-wide public alerting began in California in October of 2019, expanded to Oregon in March of 2021, and to Washington in May of 2021. Today millions of people can receive ShakeAlert-powered EEW through a variety of delivery methods and dozens of machine-to-machine protective systems are in place in transportation systems, utilities, fire stations, schools, hospitals, and public and private buildings. The ShakeAlert System implementation plan calls for a supporting network of 1,675 seismic stations. 1,129 (73%) have been completed and the rest should be done by 2025.

Introduction

Since 2006 the U.S. Geological Survey (USGS) along with partner organizations has beendeveloping the ShakeAlert Earthquake Early Warning (EEW) system for the highest risk areasof the United States: California, Oregon, and Washington. The purpose of the system is to reduce the impact of earthquakes and save livesand property by providing alert messages to the public via existing mass notification technologies and to institutional users and commercial service providers to trigger automated, user-specific protective actions.

The ShakeAlert System leverages the existing earthquake monitoring capability and expertise of the Advanced National Seismic System (ANSS)regional networks. The project is a collaboration ofmany organizations including the USGS, Caltech, UC Berkeley, the California Geological Survey,the California Governor's Office of Emergency Services, the University of Washington, the University of Oregon, the University of Nevada, Reno, Central Washington University and UNAVCO. Dozens of public and private organizations and businesses are developing anddeploying ShakeAlert-powered products and services and ten organizations have received licenses to operate. The ShakeAlert System has been available to a limited number of beta users since 2012 but thefirst major rollout occurred in October 2018 when the system was declared "open for business" and made available to public and private institutional "pilot" users on the West Coast, including emergency responders, schools, utilities, rail systems, and

businesses. Public mass alerting via authorized smartphone apps and Federal Emergency Management Agency's Wireless Emergency Alert (WEA) system began inCalifornia on October 19, 2019, expanded to Oregon on March 11, 2021, and to Washington on May 4, 2021. ShakeAlert-powered products andservices are now offered by 10 licensed operators who are part of a growing EEW industry.

Major System Components

The ShakeAlert system is made up of several major geographically distributed but tightly interconnected sub-systems and components. These are ground motion sensors networks, data processing and alert production centers, alert distribution systems, technical user implementations, a testing and performanceplatform, continuing research and development, and a robust education and outreach program.

Ground Motion Sensor Networks

The ShakeAlert build-out plan (Given et al., 2018) calls for a total of 1,675 high-quality, real- time seismic stations: 1,115 in California and 560in the Pacific Northwest. All sites have three- component strong motion accelerometers and about a quarter include broad-band seismometers. This number provides a typical station spacing of 10 km in urban areas, 20 km in seismic sourceareas that endanger population centers, and 40 km in other areas. About 1,229 seismic stations, 73%of the target number, are currently contributing data and the balance are being built with both federal and state funding. Early priority was given to covering the southern California, San Francisco Bay, and Seattle/Tacoma regions which are now at or near target density. Plans also call for using datafrom hundreds of existing high-rate, real-time GNSS receivers operated by USGS and cooperator networks.

The ShakeAlert System's public safety mission requires fast and reliable delivery of remote sensor data to processing centers. Resilience is aided by using many independent commercial and co-operator communication services (e.g., cellular, IP radio, microwave, satellite, and internet) as well as microwave and radio infrastructure operated by USGS, state agencies, and other partners.

Data Processing and Alert Centers

The ShakeAlert production system now inoperation (v2.1.5) is designed with both spatial andfunctional redundancy. Data processing centers aredistributed along the West Coast in Seattle, Washington, and Menlo Park, Berkeley, and Pasadena, California and are jointly staffed by USGS and university personnel. The system processing architecture has three major layers—a Data Layer for handling high volumes of real-time ground motion data; a Processing Layer that does waveform analysis, earthquake detection, magnitude calculation, and ground motion predictions, and finally an Alert Layer that decides when events should be published and creates various message products. System modules communicate using ActiveMQ message brokers.The Alert Layer meets U.S. government standards for data security and all high-level data are encrypted. All production servers and software components are continuously monitored using industry best-practices and standard tools to detect system faults, failures, security issues, and

monitor state-of-health and resource usage. In addition, the system meets government requirements andstandards for its designation as a Highly Valued Asset by the Department of Homeland Securityand is subject to regular cybersecurity tests,reviews, and audits.

Scientific Algorithms

The system currently has two rapid earthquake detection algorithms. The first is EPIC which is based on the ElarmS algorithm (Chung et al., 2019).It creates short-term average/long-term average (STA/LTA) triggers in small, filtered time

windows and associates these into point-source solutions using a grid search method solutions and peak P-wave displacement to estimate magnitudes.EPIC has several checks to discriminate between random noise and earthquake shaking and includesa “filter bank” check to reject teleseisms. The second is FinDer (Finite-Fault Detector) which canproduce both a point-source or line-source solutionby estimating the fault’s centroid location, orientation, and length using a pattern search technique to fit ground motion observations to pre-calculated fault templates (Böse, et al., 2012). A Solution Aggregator combines EPIC and FinDer solutions into a single weighted average solution that is the basis for several alert and information products. The eqInfo2GM module (Thakoor et al., 2019) take this combined solution and uses ground motion prediction and intensity conversion equations to estimate the resulting distribution and value of instrumental Modified Mercalli Intensity (MMI), Peak Ground Acceleration (PGA) and Peak Ground Velocity (PGV). Finally, a Decision Module publishes the results to alert servers if theymeet the criteria for public release.

The system revises its solutions up to twice per second as the quake grows and more ground motion data become available. For large events,updates could continue for minutes.

Alert Products and Thresholds

To meet the needs of various users the ShakeAlert System produces three message product streams for each event, all of which are published as XML messages to a publish/subscribe system on USGS alert servers. Licensed users may subscribe to one or more of these message streams.The *dm_event* messages include the earthquake magnitude and location but no estimate of ground shaking. The *gm_contour* messages containmagnitude and location results plus contours (as 8- point polygons) of MMI shaking intensity. The *gm_map* messages include magnitude and location plus a 0.2°x0.2° (approximately 20km x 20km) map grid of the estimated MMI, PGA, and PGV distribution.

The ShakeAlert system can detect events as small as magnitude 2.5 in some areas and publishesevents of magnitude 3.5 or greater in order to exercise the system. Because its goal is to warn of potentially damaging shaking and frequent alerts could result in “alert fatigue”, distributers are bound in their license agreements to abide by public release thresholds based on magnitude and intensity. Public alerts delivered by the Federal Emergency Management Agency (FEMA) Wireless Emergency Alert System (FEMA, 2019) are sent only to the MMI 4+ area when the magnitude is 5.0 or larger. Apps are limited toalerting the MMI 3+ area when the magnitude is 4.5 or larger. Machine-to-machine applications may go down to magnitude 4.0.

Within a few minutes of each public alert, on- call personnel compare the ShakeAlert result to authoritative network solutions and initiate appropriate event follow-up messages and products.This includes a report for the USGS earthquake event pages summarizing how the ShakeAlert system performed.

Alert Distribution Systems

The USGS has the authority to generate alerts but does not have the infrastructure or budget for mass distribution. Public mass alerting depends on existing or newly developed mass alertingpathways. For example, FEMA's Integrated Public Alert and Warning System (IPAWS) distributes alerts to cellular mobile service providers who thenforward them to the public's smartphones and other devices as Wireless Emergency Alerts (WEAs). Limited speed tests indicate delivery performance is highly variable. Alerts may be received by some in as little as 4 seconds after an alert is published but delays of several to tens of seconds are more typical, and up to 25% of phones may never receive the alert at all.

Public alerts are also distributed by several partners using push notifications to smartphone apps. These include QuakeAlertUSA, MyShake, and Shake-ReadySD (San Diego). Google has integrated ShakeAlert messages with their Androidplatform reaching millions of people without the need to download an app. Another licensed operator, Global Security Systems, can deliver alerts encoded in commercial FM radio broadcasts to purpose-built devices and another pilot, Clover Alert, is doing the same over public televisionairwaves.

Technical User Implementations

Dozens of public and private partners aredeveloping ShakeAlert-powered products and services to take automated machine-to-machine actions. For example, San Francisco's Bay Area Rapid Transit (BART) System began slowing trains in August of 2012. Following their lead LA Metro, the Los Angeles area light rail system, and Metrolink, southern California's commuter rail system, began using ShakeAlert products in 2021. Two water controls companies, RH2 and Varius, market equipment to automatically control valves, gates, and pumps in municipal water, sewage, and power systems. Other licensed partners like Early Warning Labs, SkyAlert, and Valcom, provide systems to alert people or take automated actions inother venues like high-rise condos, fire stations,schools, hospitals, offices, and public buildings.

Testing and Performance Platform

The ShakeAlert System Testing andPerformance (STP) Platform provides quantitative assessment of the performance of individual algorithms and the system as a whole (Cochran, et al., 2018a). No change is made to the production systems' configuration or software without STP evaluation. The STP platform supports two testingmethodologies. Candidate changes are run in a live real-time environment that is identical to the actual production system for a minimum of two weeksbut usually longer. In offline testing, a suite ofhistorically recorded waveform sets is replayed in apseudo-real-time test environment. The test suite includes 65 Japanese events, 140 U.S. West Coast earthquakes, 63 regional and teleseismic events,and 36 sets of problematic signals like sensor re- centering and calibration events. Results for point source solutions are

compared to the authoritative ANSS network solution and baseline runs. Also, ShakeAlert ground motion predictions are compared to ShakeMaps for each test event. If test results show an improvement in performance, the change is deployed. The effectiveness of testing is limited because there are few large U.S.earthquakes available for the test suite and many ofthe historic events that are available were recorded with older, sparser sensor networks than exist today. The STP Platform will evolve to accommodate new algorithms and other changes tothe system architecture. For example, new procedures and tools are being added to compare ground motion estimates rather than source results, like location and magnitude.

Continuing Research and Development

Research and development to improve thesystem is ongoing (Cochran et al., 2018b). Improvements are constantly being made to production algorithms to improve the speed and accuracy of source characterization and ground motion predictions.

New methods are under development. Test results of the PLUM (Propagation of Local Undamped Motion) algorithm (Cochran et al., 2019) suggest it could improve the performance of ShakeAlert and provide backup to more traditional methods, especially during complex sequences. Geodetic methods like GFAST-PGD (Williamson, et al., 2020) are also being developed and tested to improve alerts by better constraining the sourceextent and magnitude of large earthquakes.

Research into the theoretical limits to EEW and how to maximize its effectiveness is ongoing. Meier (2017) and Minson et al. (2018; 2019) have explored the limits of EEW and show that for shallow crustal earthquakes it is difficult to provideaccurate and timely warnings using high ground motion thresholds to initiate protective actions. Longer warning times are possible when lower ground motion thresholds are used but users will experience more cases where strong shaking does not arrive.

Social science research is also being done tounderstand human response to alerts and informdecisions about setting alert thresholds, alert messages, signals and sounds, effective public education, and appropriate protective actions. Currently 17 projects are under way at 10 universities and research institutions across 5 U.S. states, Canada, Europe, New Zealand, Japan, and Mexico.

Education and Outreach Program

For ShakeAlert products to be effective, people must be trained to react quickly and effectivelywhen they receive an alert. Also, institutional usersmust understand the system's benefits for their organization and be motivated to implement automated actions and provide announcements to their personnel. To accomplish this, the ShakeAlertproject includes a vigorous communications, education, and outreach effort with participationfrom stakeholders from all three states and Canada.

This effort is focused on five priorities: public preparedness, technical implementation, consistent messaging and communications, integration withother earthquake products, and

development anddissemination of educational resources. A ShakeAlert Messaging Toolkit is available for free at (https://www.shakealert.org/messaging_toolkit/)that includes guidance, talking points, andmultimedia materials tailored to reach a variety of stakeholder groups. Materials are available in several languages and are intended to integrate with existing earthquake preparedness efforts, encourage consistent information about ShakeAlertSystem technology, and promote appropriate protective actions.

Conclusions

Although the ShakeAlert sensor network is not yet complete and the project is not fully funded, it is "open for business" and providing earthquake early warning for millions of Americans in the highest risk states of our nation: Washington, Oregon, and California. Automated machine-to- machine protective systems are installed in transportation systems, utilities, fire stations, schools, hospitals, and public and private buildings,and a budding EEW industry is growing. The system is transitioning from development to an operation and maintenance phase, but it will never be "finished". Much work remains to improve the reliability, speed, and utility of the alert messages and delivery to users. The public must be educated about the system's capabilities and limitations, and most importantly on how to protect themselves when they receive an alert. Decision makers need to be educated about the system's value in protecting their organization's people and infrastructure. Finally, the nascent EEW industry must be encouraged to flourish in order to maximize the benefits of EEW in reducing earthquake losses.

Disclaimer

Any use of trade, firm, or product names is for descriptive purposes only and does not imply endorsement by the U.S. Government.

References

Böse, M., Heaton, T.H. and Hauksson, E., 2012. Real-time finite fault rupture detector (FinDer) for large earthquakes. Geophysical Journal International, 191(2), pp.803-812.

Chung, A.I., Henson, I. and Allen, R.M., 2019. Optimizing earthquake early warning performance: ElarmS-3. Seismological Research Letters, 90(2A), pp.727-743.

Cochran, E.S., Kohler, M.D., Given, D.D., Guiwits, S., Andrews, J., Meier, M.A., Ahmad, M., Henson, I., Hartog, R. and Smith, D., 2018a. Earthquake early warning ShakeAlert system: Testing and certification platform. Seismological Research Letters, 89(1), pp.108- 117.

Cochran, E.S., Aagaard, B.T., Allen, R.M., Andrews, J., Baltay, A.S., Barbour, A.J., Bodin, P., Brooks, B.A., Chung, A., Crowell, B.W.,

Given, D.D., Hanks, T.C., Hartog, J.R., Hauksson, E., Heaton, T.H., McBride, S., Meier, M-A., Melgar, D., Minson, S.E., Murray, J.R., Strauss, J.A., and Toomey, D., 2018b, Research to improve ShakeAlert earthquake early warning products and their utility: U.S. Geological

Survey Open-File Report 2018–1131, 17 p.

Cochran, E.S., Bunn, J., Minson, S.E., Baltay, A.S., Kilb, D.L., Kodera, Y. and Hoshiba, M., 2019. Event detection performance of the PLUM earthquake early warning algorithm in southern California. Bulletin of the Seismological Society of America, 109(4), pp.1524-1541.

FEMA, 2019. Integrated Public Alert and WarningSystem (IPAWS). Federal Emergency Management Agency, US:https://www.fema.gov/emergency- managers/practitioners/integrated-public-alert- warning-system

Given, D.D., Allen, R.M., Baltay, A.S., Bodin, P., Cochran, E.S., Creager, K., de Groot, R.M., Gee,L.S., Hauksson, E., Heaton, T.H. and Hellweg, M., 2018. Revised technical implementation plan for the ShakeAlert system—An earthquake early warning system for the West Coast of the United States (No. 2018-1155). US Geological Survey.

Meier, M.A., 2017. How "good" are real-time ground motion predictions from earthquakeearly warning systems? Journal of Geophysical Research: Solid Earth, 122(7), pp.5561-5577.

Meier, M.A., Heaton, T. and Clinton, J., 2015. The Gutenberg algorithm: Evolutionary Bayesian magnitude estimates for earthquake earlywarning with a filter bank. Bulletin of the Seismological Society of America, 105(5), pp.2774-2786.

Minson, S.E., Meier, M.A., Baltay, A.S., Hanks, T.C. and Cochran, E.S., 2018. The limits of earthquake early warning: Timeliness of ground motion estimates. Science advances, 4(3), p.eaaq0504.

Minson, S.E., Baltay, A.S., Cochran, E.S., Hanks, T.C., Page, M.T., McBride, S.K., Milner, K.R. and Meier, M.A., 2019. The limits ofearthquake early warning accuracy and best alerting strategy. Scientific reports, 9(1), pp.1- 13.

Thakoor, K., Andrews, J., Hauksson, E. andHeaton, T., 2019. From earthquake sourceparameters to ground-motion warnings near you: The ShakeAlert earthquake information to ground-motion (eqInfo2GM) method. Seismological Research Letters, 90(3), pp.1243-1257.

Williamson, A.L., Melgar, D., Crowell, B.W., Arcas, D., Melbourne, T.I., Wei, Y. and Kwong, K., 2020. Toward near-field tsunami forecastingalong the Cascadia subduction zone using rapid GNSS source models. Journal of Geophysical Research: Solid Earth, 125(8),p.e2020JB019636.

THE COMMUNITY SEISMIC NETWORK FOR DENSE, CONTINUOUS MONITORING OF GROUND AND STRUCTURAL STRONG MOTION

Monica Kohler[1] and the Community Seismic Network Team

[1]Department of Mechanical and Civil Engineering
California Institute of Technology, Pasadena, CA

Abstract

The Community Seismic Network (CSN) is a cloud-based, strong-motion network of seismic stations deployed in the greater Los Angeles area. The sensors report three-component acceleration time series data and peak acceleration scalar data for use in assessments of earthquake shaking intensity in buildings and on the ground level, monitoring structural health of instrumented buildings, zonation maps of future shaking potential, and the ShakeAlert earthquake early warning system. The hardware and software behind CSN's client and server architecture are described, as well as network subarrays deployed at Los Angeles Unified School District campuses, the NASA-JPL campus, and in mid-rises and high-rises.

Introduction

This paper describes the architecture of the Community Seismic Network (CSN), a permanent strong-motion seismic network. CSN has been developed over the past 10 years by a team of scientists, listed in the Acknowledgments section of this paper, whose work is represented here. CSN hardware comprises commercially produced MEMS accelerometers that are coupled with processors, external storage, and power supply. CSN consists of over 700 accelerometers that are deployed in mid-rises and high-rises, school campuses, civic service buildings, and homes in California (Fig. 1). The CSN project has increased the number of 3D (ground level+all upper floors of buildings) seismic observations in greater Los Angeles by an order of magnitude, by taking advantage of advances in small-form-factor MEMS sensing technologies, on-site computing, and cloud infrastructure. The mission of CSN is to: 1) Provide high spatial resolution assessments of shaking intensity in buildings and on the ground following major earthquakes; 2) Monitor the health and safety of structures through detection and location of damage; 3) Create zonation maps of future shaking potential in populated areas; and 4) Provide data for the ShakeAlert earthquake early warning system (Given et al., 2014, 2018; Kohler et al., 2020).

The Community Seismic Network (CSN) currently comprises hundreds of stations located in southern California, most of which are in the greater Los Angeles area (Clayton et al., 2011, 2015, 2020; Kohler et al., 2013, 2014, 2018; Massari et al., 2017). The accelerometers are triaxial, and capable of recording accelerations up to twice the level of gravity. The primary product of the network is measurements of shaking of the ground as well as upper floors in buildings, in the seconds during and following a major earthquake. Each sensor uses a small, dedicated ARM processor computer running Linux, and analyzes time series data in real time at 250 sps, which then is downsampled to 50 sps for data storage purposes.

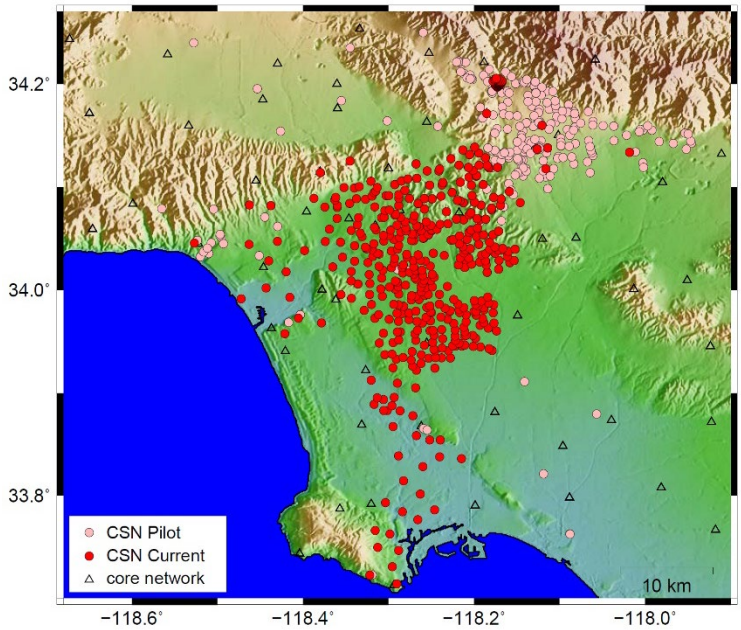

Figure 1. Seismic stations in southern California. CSN stations: circles. SCSN stations: triangles.

CSN client architecture

Hardware

CPU

CSN clients have primarily been deployed using low-power, "single-board-computer" (SBC) platforms since 2012. Such platforms typically have a physically small form factor and consume under 20 W of power, making them suitable for use with low-wattage battery backup units. They also have between one and four USB 1.0 ports, and at least one ethernet port with 10 Mbps or greater data transmission rates. Some platforms have a USB serial port suitable for on-site connectivity without disturbing an operating client. Other platforms have wireless radios, such as Bluetooth or WiFi, that provide on-site access without having to displace the active network connection.

The most recent large CSN deployment in early 2020 used 100 Raspberry Pi Model 4B units, housed in passive cooling aluminum cases. The previous large CSN deployment in early 2019 used 200 Raspberry Pi Model 3B units, also housed in passive cooling plastic cases. Board failures have not been observed in the ~2.5 years after deployment, despite the reliance on small chip-size heat sinks used in the absence of aluminum cases to serve as heat sinks. A small number (~5) of Raspberry Pi Model 3B+ units have also been deployed; these were originally for laboratory use but were later migrated into the field to meet deployment goals. Each of the Raspberry Pi units allows for the use of SD cards for a moderate amount (about three months) of on-site storage.

CSN's first SBC platform beginning in early 2012 was the Global Scale Technologies SheevaPlug, which includes a single USB 2.0 port, a single RJ-45 1 Gbps ethernet port, 512 MB

internal flash drive, and an external SD card slot. It also provides a mini-USB port for serial console access. Over 400 of these are still deployed and operating at CSN stations in the field. The SheevaPlug has a single USB mini-A port configured so that it can be connected to a laptop or desktop USB A port via USB serial interface. MacBook Pros and most Windows-compatible laptops need no special USB driver software to communicate with a SheevaPlug; however earlier MacOS systems may need a dedicated driver for the SheevaPlug.

Accelerometer

Through 2021, CSN has used only one type of accelerometer family to provide the base acceleration data - the phidgets.com Model 1056, based on the STMicroelectronics analog MEMS LIS344ALH triaxial inertial sensor with ± 2g range. Initial CSN stations used the original 1056 model that included a compass and gyroscope, but most CSN stations now use the model 1056-1 which only has the triaxial accelerometer.

Power, battery backup, and power boards

A combination of power options attempt to provide CSN stations with a few hours of backup power. In some cases, emergency power is available from the sensor host enterprise; in other cases, local enterprise-provided Uninterruptible Power Supply (UPS) units are available for use. When reliable backup power is not available, small battery backup units are added to the setup.

The canonical UPS deployed to date is a CyberPower CP350SLG unit which typically provides a couple of hours of standby power. This unit has a form factor that neatly fits into the external CSN box packaging that has been deployed since the outset, but the units lack an interface that would support status monitoring. One issue with these units is the limited lifetime (2-3 years) of the internal sealed lead acid battery. In addition, while a single battery replacement cycle works well, a second replacement cycle is less likely to succeed. At the third replacement point, the unit is scrapped.

Early SheevaPlugs were notorious for premature failure of their internal 120 VAC-to-5 VDC power supply board. Now, after 5-8 years of deployment, CSN's SheevaPlugs are experiencing increasing rates of power board failures. As of early 2021, these power boards are no longer available from the vendor, so a suggestion from the user community was adopted in which failed boards are replaced with a generic 2.5Amp power adapter wall wart, and the factory output plug is replaced with a harness obtained from a retired SheevaPlug power board.

CSN server architecture

Software

Operating system

The CSN client software is based on the Linux operating system running on the hardware platform with USB and ethernet interfaces. The USB interface is primarily used to connect to the accelerometer. The ethernet interface is the primary means of sending locally collected

accelerometer data to the CSN server environment. The ethernet interface is also used to maintain an open reverse-ssh tunnel to the server environment. This permits remote access from the server to the client even if client-side enterprise firewalls are present.

Preparing the SBC's operating system platform involves a combination of tasks that include: ensuring that a base level of applications has been installed on the platform to support CSN tools; setting various configuration parameters specific files for each application of interest; and in some cases disabling conflicting applications. CSN practice is to retain the operating Linux system version originally installed on a hardware platform. This provides a degree of stability and predictability that is valuable over many years. As of 2021, several 8-year-old deployments are still in operation and are expected to continue in perpetuity. This also addresses early versions of hardware that do not readily support operating system version upgrades. However, the above practice also implies ongoing support for an ever-growing number of Linux versions, each typically customized for a particular hardware platform family and model.

Client application

The CSN client application is a Python script, currently written to Python 2.7. It is thread-based, in which the threads are used to handle several different tasks:

- Interfacing with the accelerometer over USB and receiving triaxial samples from the sensor.
- Processing the triaxial samples from the sensor (including decimation, mean removal, property assessment).
- Creating picks from incoming sensor samples.
- Monitoring the system clock, obtaining Network Time Protocol (NTP) time from a time server, computing a regression, and providing other threads with timestamp.
- Uploading 10-minute raw data files to Amazon S3, and uploading latest station configuration data file to Amazon S3.
- Implementing a web server interface for remote users to obtain data from the client including: a) uptime, b) version, c) latest accelerometer sample, d) 10-minute files for arbitrary periods of time, e) latest 2 minutes of data in the form of Google Charts for each of the three sensor axes.
- Ensuring that sufficient space is available on local storage by deleting older files when necessary.

The main client program contains the credentials for accessing both the Amazon S3 service that will store the sensor data, and the location and credentials for the ActiveMQ broker which will receive the picks from the client. (ActiveMQ is open-source messaging software that is employed by the distributed algorithms and applications that require messaging, and the broker is an application that validates, translates and routes a message from a sender to a receiver). The CSN client file is in a human-readable format that contains CSN station metadata including the sensor's latitude and longitude, building identification, floor number, and client name. This is routinely edited to contain the required details.

Timing and accuracy

Accurate timestamps are required in the client to ensure that the data points are all synchronized with accurate external clocks and with those from other clients. This is especially critical for deployments of several clients within the same building, for example all sensors from sequential floors in a building for which inter-story drift or propagating wave property calculations are desired. To achieve accurate timestamps, the client applies a linear regression to the reported times obtained from one of several possible NTP servers on the network. Typically, the servers are at Caltech, UCLA, and USC, but sometimes the local router is used for failover capability. In some cases, a CSN SBC in the field serves as the NTP server (e.g. a separate CSN NTP server in a building).

The client polls the NTP server every minute, and the offset between the system clock and the NTP time is added to a sliding 10-minute window of offsets. A linear regression is then performed on the latest 10 minutes of data, which allows an estimate to be made for the true time at any data point (i.e. time series sample) over the coming minute before the NTP server is polled again. An example of how the NTP offsets and predicted offsets look over a 1-hour period is shown in Fig. 2.

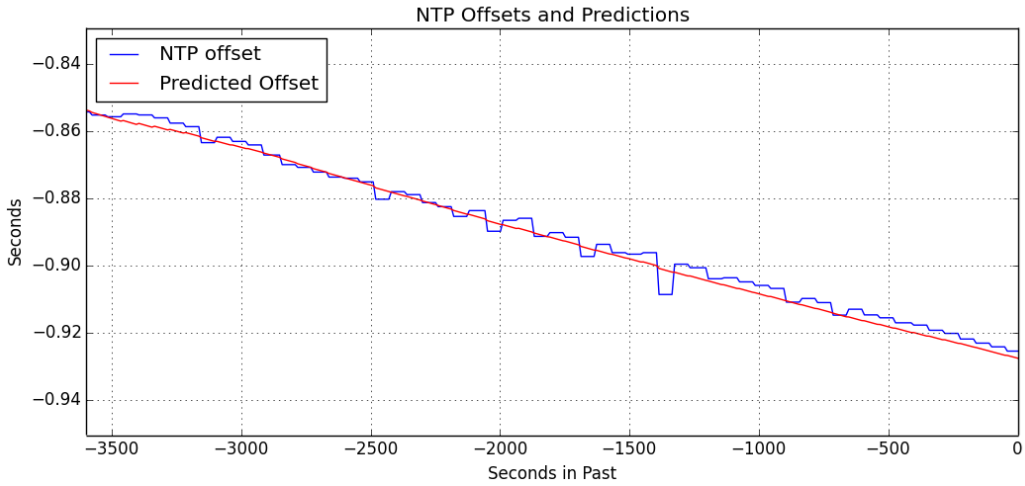

Figure 2. Example of NTP offsets (blue curve) and predicted time offsets (red line) over a 1-hour period of waveform data.

Client server architecture

CSN provides both real-time and near-real-time access to client-generated data. Limited real-time data flows instantly from CSN clients to a CSN cloud server data broker, to which two subscribers currently connect – one for earthquake early warning test applications and the other for a ShakeMap (Wald et al., 2008; Worden et al., 2020) service test instance. Near-real-time data flows in short bursts (currently, 10-minute-long time series) from CSN clients through a CSN cloud server to a local server-based archive at Caltech.

The method by which these parallel data flows are carried out is as follows. The CSN client running on the Linux-based processor at each station has two different but concurrent

modes for uploading data. In the first mode (referred to as "pick mode"), the station software instantly detects anomalously large waveform events in the data stream, such as high-amplitude accelerations, and immediately sends the computed peak amplitude scalar values and their associated time stamps to the Amazon cloud (AWS). In this mode, the CSN python application assesses the incoming stream of samples from the phidget sensor device library, and it forwards the selected samples to a server running on the CSN cloud infrastructure. The pick mode data are those that are currently designated for ShakeMap and the ShakeAlert earthquake early warning system.

The CSN station uploads all waveform data in the second near-real-time mode ("continuous mode"). The station's processor accumulates 10 minutes of three-component, minimally processed, unfiltered, acceleration data into a file. Once the file is complete, it is compressed and uploaded to the cloud, while data are being accumulated into the next file. The 10-minute data files are retained by the station's system until the local storage use reaches a maximum threshold value, at which time the files are aged out; typically this amounts to a few weeks of sensor data with the flash storage cards. This storage system would need to be accessed for accumulated data in the case of power outages or communications problems.

CSN's software client computes peak accelerations which are reported as picks (the "pick mode" introduced above) if values are > 0.5% g. The picks are computed from the time series' deviations from a long-term mean calculated over 10-second sliding windows. Each orthogonal axis is treated independently and the minimum repick interval is 1 second on the same axis; thus the maximum pick rate is 3 picks/second. Timestamps associated with the picks are calculated using a continuous regression on the NTP offsets to the computer's system clock, as discussed earlier. Only ground-level station picks are sent to the cloud for the ShakeMap and ShakeAlert applications.

In the current implementation of CSN's pick distribution method, the CSN client (running at the station) directly generates an ActiveMQ message for each pick locally on the station's processor, in the required format for ShakeMap or the earthquake early warning applications FinDer (Böse et al., 2012, 2015, 2018) and PLUM (Cochran et al., 2019). The CSN server sends that message to an ActiveMQ broker running on an AWS virtual machine. The CSN client includes an NTP-based corrected pick timestamp in the ActiveMQ message. ShakeAlert operates its own ActiveMQ brokers, whose topics are subscribed to by the various algorithms, including FinDer and PLUM. A channel between the CSN broker and the ShakeAlert broker used by development versions of FinDer and PLUM allows it to receive all CSN client picks. Both FinDer and PLUM use all reported CSN client picks associated with an earthquake, since they always exceed 0.5% g. At the server side where PLUM is running, MMI values are computed continuously for the incoming accelerometer measurements. MMI is computed from the incoming PGA pick values on all three components, and sent when an MMI threshold for PLUM is exceeded. The maximum rate of MMI messages being sent by each client is one message per second, for the duration of the shaking. Similar to FinDer, these MMI values are relayed to the ShakeAlert ActiveMQ broker to which the development version of PLUM is subscribed.

As of August 2021, the data stream provided by the CSN python client application to the CSN ActiveMQ broker sufficiently matches the expectations of the ShakeAlert infrastructure to support a direct subscription. Future enhancements to the stream from the CSN client to the CSN ActiveMQ broker may require an additional level of processing and assessment within the cloud, prior to making the data available to the ShakeAlert production system.

The data flow architecture is illustrated in Fig. 3. The key motivation for this setup is to prevent large latencies that can arise in part from the current ShakeAlert requirement that each station sends full waveforms to the central processing site.

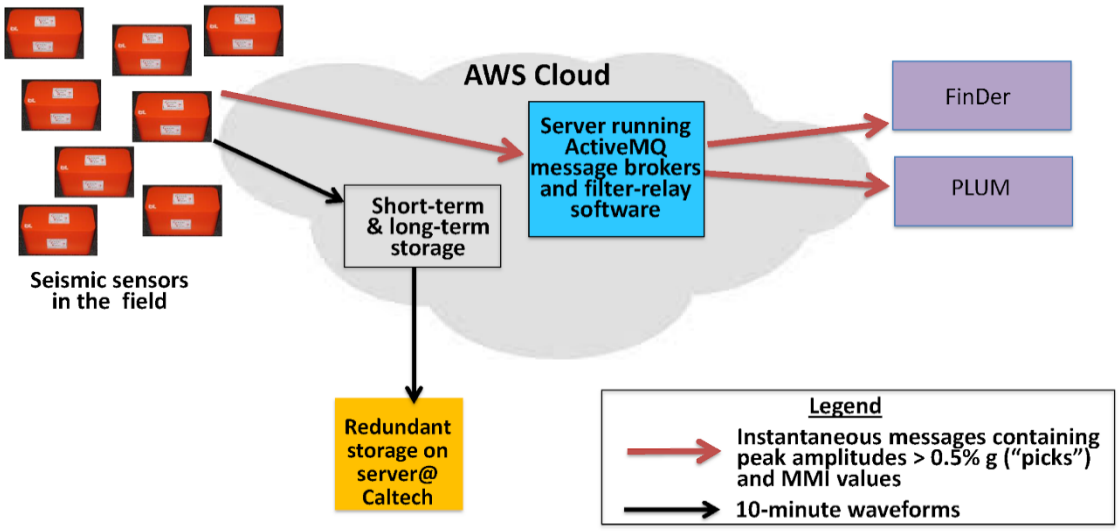

Figure 3. Data flow architecture schematic. Sensors in the field (left side of diagram) send two types of data to the message broker and storage servers in the Amazon cloud (AWS cloud). Data are then passed on to development instances of FinDer and PLUM (right side of diagram).

The ShakeMap infrastructure requires a different format and content for peak amplitude data than is provided by the CSN cloud ActiveMQ broker for ShakeAlert. Therefore, a service running on the local server platform subscribes to the CSN ActiveMQ broker, provides very low latency reformatting of the incoming peak amplitude (pick) data stream, and then sends those data onward to the ShakeMap infrastructure.

A number of waveform data retrieval applications operate on the local server to provide continuous waveform time series files to researchers. The main application is based on the Seismogram Transfer Program (STP) client (STP, 2007) and can deliver data for all stations rapidly for recent months, and with a small latency for data older than that. Customized CSN STP-based clients serve a subset of sensors such as all stations at Los Angeles Unified School District campuses, NASA-JPL, and several instrumented mid-rise and high-rise buildings. The applications rely on three file types for their operation: 1) the station file which contains the metadata information for each station in CSN, 2) the waveform metadata files which contain metadata information about each waveform segment, and 3) the waveform segment files

themselves which contain the digital samples in SAC format. The data used by the applications is refreshed by restarting them; this is done on a regular basis several times a day.

Los Angeles Unified School District (LAUSD) stations

The majority of CSN stations are deployed at campuses of the Los Angeles Unified School District (LAUSD). LAUSD is a public, general-community stakeholder and partner, with approximately 1000 campuses that span the City of Los Angeles (2000 km^2). The school campus buildings are typically 1-3 story wood frame or reinforced concrete structures built after 1950. These structures include types that are known to be prone to severe damage due to seismic hazards, especially for older construction and soft first-story construction. Approximately 400 of the LAUSD campuses are instrumented with CSN sensors (majority of red circles shown in Fig. 1). Average CSN station spacing at LAUSD campuses is about 0.5 km.

An experimental ShakeMap-ShakeCast-like setup has been developed for the LAUSD campuses at which CSN has deployed a sensor (Kohler et al., 2018). The setup is generally based on features of ShakeCast (Wald et al., 2008), including the use of the Hazus Earthquake Model Loss Estimation Methodology (Hazus, 2020) to classify structures and supply fragility curves. However, key differences are that it uses CSN data recorded at the actual structure as shaking intensity input into the fragility functions for the structure, and CSN-developed web-based tools for its user interface. The LAUSD campuses used in this installation consist of only low-rise structures across a lateral dimension spanning about 20 km. All sensors are located in communication or utility closets; none are in classrooms. The ShakeCast application is installed in the central LAUSD office in downtown Los Angles and communication is modeled on a centralized decision engine setup in which information could be subsequently sent via formal channels to local principals and campuses.

As mentioned above, CSN's current software client computes broadband peak accelerations which are reported to ShakeMap if values are > 0.5% g, obtained from the time series' deviations from the long-term mean, on any axis. Many CSN stations on school campuses are in locations with frequent human activity that influences noise levels. For example, many LAUSD stations exhibit noticeably higher noise levels during school hours. In future work, station-specific noise models taking into account time of day and day of the week could be trained, allowing for more reliable picking and signal-to-noise estimation at stations with predictable human-generated noise.

Mid-rise and high-rise instrumentation

Several mid-rise and high-rise buildings are currently instrumented by CSN with at least one triaxial sensor deployed on most floors. All are located in the downtown or greater Los Angeles region. The buildings include a 52-story dual system (concentrically braced steel frames at core with outrigger moment frames (with 63 sensors); 15-story steel moment frame and concrete shear wall (with 34 sensors); 9-story reinforced concrete (with 10 sensors); and two 9-story steel moment-frame with trusses and girders (one with 31 sensors and the other with 15 sensors).

Several of the instrumented buildings have two or three triaxal sensors deployed on most floors, for the purpose of measuring torsion, rotations or rocking. Although the sensors are not usually located at the edges of the floors, their locations relative to the center of mass on the building floor can be determined from structural engineering drawings obtained for most of the instrumented buildings. The majority of sensors are located in electrical or IT closets. One of the CSN-instrumented buildings – the 52-story high-rise – also has CSMIP instrumentation that has recorded significant earthquakes since the 1992 M7.3 Landers earthquake, and could be used for data comparison of the July 2019 M7.1 and M6.4 Ridgecrest earthquakes, the September 2020 M4.5 South El Monte earthquake, and the April 2021 M4.0 Lennox earthquake.

NASA-JPL stations

A total of 220 CSN triaxial accelerometers are deployed on the ~ 1 km × 1 km NASA-JPL campus. This subset of sensors could be considered an "array within an array" due to their smaller but approximately equidistant station spacing. Sensors are installed on both ground-level and upper-level floors of several buildings. The ground-level stations have an average spacing of about 100 m.

The NASA-JPL sensor deployment can be viewed and tested as a prototype mini-city strong-motion deployment, as there are one or more CSN accelerometers installed in about 90 buildings (mostly single or two-story structures) on the campus. The building types comprise wood frame, steel sheds, modular trailers, steel-moment frame, and reinforced concrete. Of the total 220 stations deployed at JPL, only the 100 ground-level stations are contributing maximum shaking peak acceleration pick data for the experimental ShakeMap and earthquake early warning algorithms. As with the LAUSD subarray, a ShakeMap-ShakeCast-like setup has been configured for JPL (Massari et al., 2017). Each of the buildings uses fragility curves supplied by the Hazus Earthquake Model Loss Estimation Methodology (Hazus, 2020). The ShakeCast configurations for the JPL sites are set up so that they use the CSN ShakeMap as input for localized and customized building performance assessment. Several buildings have either two or three sensors located on the ground level floors because the structures are long or they contain a significant element joint halfway down the longitudinal axis of the building.

2019 Ridgecrest earthquake

The July 2019 Ridgecrest earthquake sequence that occurred in southeastern California, was recorded on hundreds of CSN sensors in the Los Angeles basin (Kohler et al., 2020; Filippitzis et al., 2021). In particular, CSN captured variations in ground-level motion and upper floor deformation within mid- and high-rise buildings and showed unexpected patterns of large spatial variations in shaking amplification, as was envisioned as a primary purpose of CSN. Work with CSN recordings of the M7.1 mainshock revealed amplified shaking in the instrumented 52-story high-rise in downtown Los Angeles lasting over two minutes. In addition, ground-level accelerations showed increases in the amplification of long-period motions (> 1 s) from the northern Los Angeles sedimentary basin (Fig. 4). In Fig 4, several locations show nearly co-located CSN and SCSN or CSMIP instrumentation (circles and diamond symbols in close proximity), indicating the consistent response between stations of the different networks for this earthquake. High-rises experienced unusually strong long-period shaking in the east-west

direction as a result of excitation by a complex train of scattered shear waves inside the basin, including surface waves propagating in the basin. The density of the CSN observations demonstrated that the behavior of structures (e.g. buildings) with long natural periods does not follow long-standing expectations for how sedimentary basins affect amplification (Filippitzis et al., 2021).

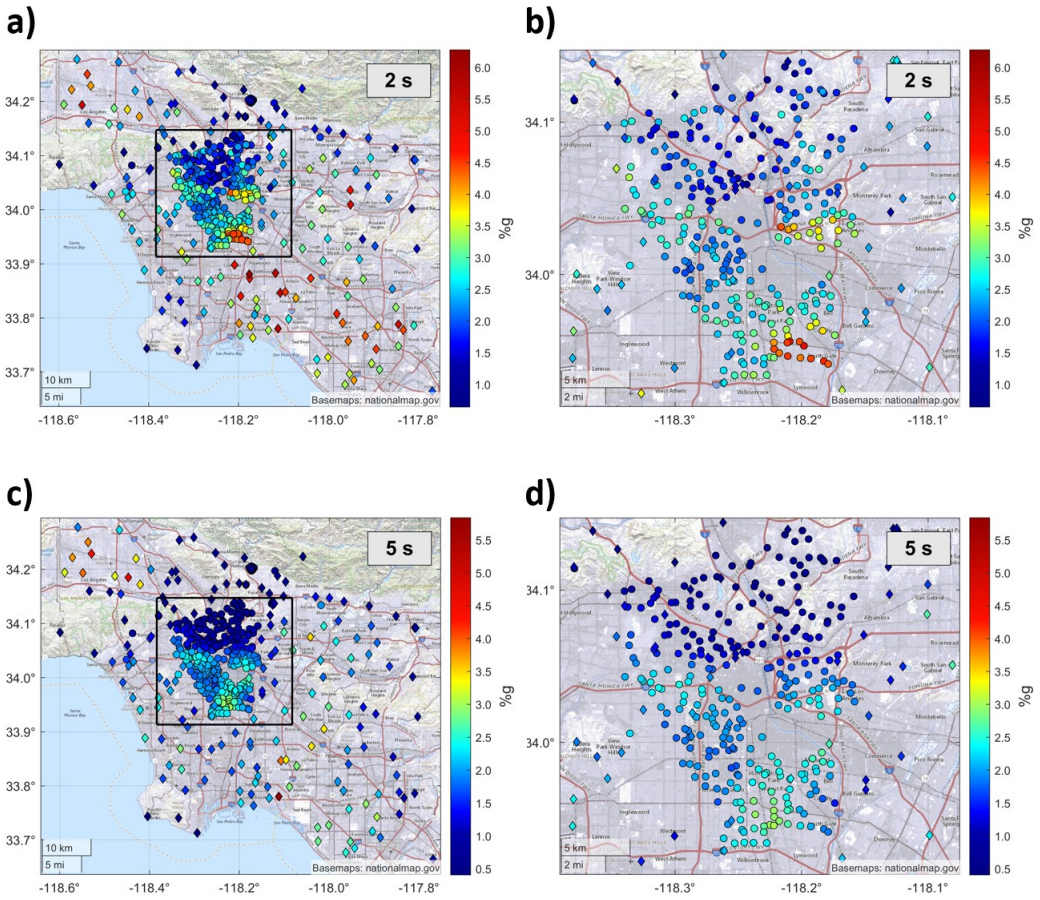

Figure 4. Pseudo-spectral acceleration amplitudes using 5% damping for the 2019 M7.1 Ridgecrest earthquake in southern California. Periods shown are: (a,b) 2 s, and (c,d) 5 s. Left column: Greater urban Los Angeles region. Right column: Blow-up of the region inside the marked squares on the left, showing detail. CSN stations=circles. SCSN+CSMIP stations=diamonds.

The ground-level accelerations recorded by CSN from the Ridgecrest earthquakes also exhibited coherent, gradational variations in the spectral amplitudes of high-frequency motions across the NASA-JPL campus that suggest correlations with geomorphological features (ridges, canyons, and foothills). The variations in spectral amplitudes are most pronounced for frequencies between 1 and 3 Hz. For the M7.1 mainshock, the overall maximum amplification occurred in the highest elevation, on top of the bedrock mesa bounding the campus to the north. The M6.4 and M5.4 foreshocks show a similar amplification pattern. The amplification pattern changes with the frequency as energy components of various wavelengths interact with surface and subsurface features of different characteristic lengths. For this higher-frequency range, the

incoming waves likely interacted with numerous small-size features at the site to generate a complex, rapidly-varying amplification pattern.

The integration of site-specific and structure-specific instrumentation provided by the Community Seismic Network enables the deployment of large numbers of seismic sensors for dense spatial sampling. The developed framework offers a path forward for city-scale and regional-scale seismic network operations, and could serve as a scalable and reconfigurable tool for monitoring structures such as tall buildings, bridges and dams, as well as lifeline infrastructure.

Acknowledgements

The Community Seismic Network is the product of years of work by many people who have made up the CSN team over the years. The author is a part of this team, and in representing this team wishes to acknowledge their past and ongoing contributions to the CSN project. The current CSN team members are Robert Clayton (Seismological Lab; California Institute of Technology), Thomas Heaton (Department of Mechanical and Civil Engineering, and Seismological Lab, California Institute of Technology), Richard Guy (Department of Civil and Environmental Engineering, University of California, Los Angeles; and Seismological Lab, California Institute of Technology), Julian Bunn (Center for Data-Driven Discovery, Division of Physics, Math and Astronomy, California Institute of Technology), Filippos Filippitzis (Department of Mechanical Engineering, University of Western Macedonia, Kozani, Greece; and Department of Mechanical and Civil Engineering, California Institute of Technology), Yousef Bozorgnia (Department of Civil and Environmental Engineering, University of California, Los Angeles) and Ertugrul Taciroglu (Department of Civil and Environmental Engineering, University of California, Los Angeles). The CSN team is grateful to Caltech, UCLA, the Conrad N. Hilton Foundation, and Computers & Structures Inc., the Gordon and Betty Moore Foundation, and the National Science Foundation for providing support for the Community Seismic Network over the past decade.

References

Böse, M., T. Heaton, and E. Hauksson (2012). Real-time finite fault rupture detector (FinDer) for large earthquakes, *Geophys. J. Int., 191*, 803-812.

Böse, M., C. Felizardo, and T. H. Heaton (2015). Finite-fault rupture detector (FinDer): Going real-time in Californian ShakeAlert Warning System, *Seis. Res. Lett.,* 86(6), 1692-1704.

Böse, M., D. E. Smith, C. Felizardo, M.-A. Meier, T. H. Heaton, and J. F. Clinton (2018). FinDer v.2: Improved real-time ground-motion predictions for M2-M9 with seismic finite-source characterization, *Geophys. J. Int.,* 212, 725-742.

Clayton, R., T. Heaton, M. Chandy, A. Krause, M. Kohler, J. Bunn, R. Guy, M. Olson, M. Faulkner, M. H. Cheng, L. Strand, R. Chandy, D. Obenshain, A. Liu, and M. Aivazis (2011). Community Seismic Network, *Annals of Geophysics*, 54, 6; doi: 10.4401/ag-5269.

Clayton, R. W., T. Heaton, M. Kohler, M. Chandy, R. Guy, and J. Bunn. (2015). Community Seismic Network: a dense array to sense earthquake strong motions, *Seis. Res. Lett*., 86, 1354-1363, doi: 10.1785/0220150094.

Clayton, R., M. Kohler, R. Guy, J. Bunn, T. Heaton, and M. Chandy (2020). CSN/LAUSD network: A dense accelerometer network in Los Angeles schools, *Seis. Res. Lett.,* 91(2A), 622-630, doi:10.1785/0220190200.

Cochran, E. S., J. Bunn, S. E. Minson, A. S. Baltay, D. L. Kilb, Y. Kodera, M. Hoshiba (2019). Event detection performance of the PLUM earthquake early warning algorithm in southern California, *Bull. Seis. Soc. Am.,* 109 (4), 1524–1541, doi:10.1785/0120180326.

Filippitzis, F., M. D. Kohler, T. H. Heaton, R. W. Graves, R. W. Clayton, R. G. Guy, J. J. Bunn, and K. M. Chandy, Ground motions in urban Los Angeles from the 2019 Ridgecrest earthquake sequence, *Earthquake Spectra*, version available online, doi:10.1177/87552930211003916, 2021.

Given, D., E. Cochran, T. Heaton, E. Hauksson, R. Allen, M. Hellweg, J. Vidale, and P. Bodin (2014). Technical implementation plan for the ShakeAlert production prototype system—An Earthquake Early Warning system for the West Coast of the United States, *U.S. Geological Survey Open-File Report 2014–1097*, 25 pp.

Given, D. D., R. M. Allen, A. S. Baltay, P. Bodin, E. S. Cochran, K. Creager, R. M. de Groot, L. S. Gee, E. Hauksson, T. H. Heaton, M. Hellweg, J. R. Murray, V. I. Thomas, D. Toomey, and T. S. Yelin (2018). Revised technical implementation plan for the ShakeAlert system—An earthquake early warning system for the West Coast of the United States, *U.S. Geological Survey Open-File Report 2018–1155*, 42 pp., doi:10.3133/ofr20181155.

Hazus (2020). *Hazus Earthquake Model Technical Manual.* Federal Emergency Management Agency, Washington, D.C. https://www.fema.gov/sites/default/files/2020-10/fema_hazus_earthquake_technical_manual_4-2.pdf.

Kohler, M. D., T. H. Heaton, and M. H. Cheng (2013). The Community Seismic Network and Quake-Catcher Network: enabling structural health monitoring through instrumentation by community participants, *Proceedings of the SPIE Smart Structures/Non-destructive Evaluation Conference*, San Diego, CA, March 10-14, 2013.

Kohler, M. D., T. H. Heaton, M. H. Cheng, and P. Singh (2014). Structural health monitoring through dense instrumentation by community participants: the Community Seismic Network and Quake-Catcher Network, *10th U.S. National Conference on Earthquake Engineering* (*10NCEE*), Anchorage, Alaska, July 21-25, 2014.

Kohler, M. D., R. Guy, J. Bunn, A. Massari, R. Clayton, T. Heaton, K. M. Chandy, H. Ebrahimian, and C. Dorn (2018). Community Seismic Network and localized earthquake situational awareness, *11th U.S. National Conference on Earthquake Engineering* (*11NCEE*), Los Angeles, CA, June 25-29, 2018.

Kohler, M. D., D. Smith, J. Andrews, A. Chung, R. Hartog, I. Henson, D. Given, R. de Groot, and S. Guiwits (2020). Earthquake Early Warning ShakeAlert 2.0: public rollout, *Seis. Res. Lett*., 91(3), 1763–1775, doi:10.1785/0220190245, 2020.

Kohler, M. D., F. Filippitzis, T. H. Heaton, R. W. Clayton, R. G. Guy, J. J. Bunn, and K. M. Chandy (2020). 2019 Ridgecrest earthquake reveals areas of Los Angeles that amplify shaking of high-rises, *Seis. Res. Lett*., 91(6), 3370–3380, doi:10.1785/0220200170.

Massari A., M. Kohler, R. Clayton, R. Guy, T. Heaton, J. Bunn, K. M. Chandy, D. Demetri (2017). Dense building instrumentation application for city-wide structural health monitoring and resilience, *16th World Conference on Earthquake Engineering* (*16WCEE*), Santiago, Chile, January 9-13, 2017.

Seismogram Transfer Program (STP) Reference Manual (2007). Prepared by the Southern California Earthquake Data Center, Seismological Laboratory, California Institute of Technology, Version: 1.01, https://scedc.caltech.edu/data/stp/STP_Manual_v1.01.pdf.

Wald, D., K.-W. Lin, K. Porter, and L. Turner (2008). ShakeCast: Automating and improving the use of ShakeMap for post-earthquake decision-making and response, *Earthquake Spectra*, 24, 2, 533-553.

Worden, C. B., E. M. Thompson, M. Hearne, and D. J. Wald (2020). ShakeMap Manual Online: Technical Manual, User's Guide, and Software Guide, U. S. Geological Survey, http://usgs.github.io/shakemap, doi: 10.5066/F7D21VPQ.